



Fermi National Accelerator Laboratory

FN-445
(2013.000)

January, 1987

A PINACOTECA OF CROSS SECTIONS FOR
HADROPRODUCTION OF HEAVY QUARKS

R. K. ELLIS AND C. QUIGG

Fermi National Accelerator Laboratory

P. O. Box 500, Batavia, Illinois 60510

January 22, 1987

ABSTRACT

Cross sections for the production of c - and b - quarks in pN and πN collisions are presented for beam momenta from 300 to 800 GeV/c.



I. INTRODUCTION

In the last year there has been a resurgence of interest in the theory of the production of heavy quark pairs in hadronic reactions. This interest is motivated not only by the promise of reliable experiments on the hadroproduction of charm,¹ but also by reports of the observation of bottom² (and possibly top³) in hadronic reactions. In addition, the high statistics obtained⁴ for the photoproduction of charm in Fermilab experiment E-691 provide great encouragement for experiments aimed at the hadroproduction of charm and beauty. On the theoretical side, the progress^{5,6,7} of the last year can be summarized as follows. The standard perturbative QCD formula for the inclusive charm production,

$$H_1(P_1) + H_2(P_2) \rightarrow Q(P_3) + X \quad (1)$$

is given by,

$$\frac{E_3 d\sigma}{d^3 P_3} = \sum_{i,j} \int dx_1 dx_2 \left[\frac{E_3 d\hat{\sigma}_{ij}(\alpha_s(Q^2), \hat{p}_1, \hat{p}_2)}{d^3 P_3} \right]_{\hat{p}_1=x_1 P_1, \hat{p}_2=x_2 P_2} f_i^{(1)}(x_1, Q^2) f_j^{(2)}(x_2, Q^2) \quad (2)$$

The functions f are the distribution functions of light partons (gluons, light quarks and antiquarks) evaluated at a scale Q , which is of the order of the mass m of the produced heavy quark. For definiteness we shall set the scale $Q = 2m$ throughout this paper. The symbol $\hat{\sigma}$ denotes the short distance cross-section from which the mass singularities have been factored in the normal way⁸. Since the sensitivity to collinear emission has been removed from the short-distance cross-section, $\hat{\sigma}$, it is calculable as a perturbation series in $\alpha_s(Q^2)$. The lowest order which contributes is $O(\alpha_s^2)$. In this order there are contributions to $\hat{\sigma}$ due to gluon-gluon fusion and quark-antiquark annihilation.

$$\begin{aligned} (a) \quad & q(p_1) + \bar{q}(p_2) \rightarrow Q(p_3) + \bar{Q}(p_4) \\ (b) \quad & g(p_1) + g(p_2) \rightarrow Q(p_3) + \bar{Q}(p_4) , \end{aligned} \quad (3)$$

where the four momenta of the partons are given in brackets. The invariant matrix elements squared for processes (a) and (b) have been available in the literature for some time^{9,10,11} and are given by,

$$\overline{|M^{q\bar{q} \rightarrow Q\bar{Q}}(p_1, p_2, p_3, p_4)|^2} = \frac{g^4 V}{2N^2} \left(\frac{\{13\}^2 + \{23\}^2}{\{12\}^2} + \frac{m^2}{\{12\}} \right) \quad (4)$$

$$\overline{\sum} |M^{gg \rightarrow Q\bar{Q}}(p_1, p_2, p_3, p_4)|^2 = \frac{g^4}{2VN} \left(\frac{V}{\{13\}\{23\}} - \frac{2N^2}{\{12\}^2} \right) \left(\{13\}^2 + \{23\}^2 + 2m^2\{12\} - \frac{m^4\{12\}^2}{\{13\}\{23\}} \right), \quad (5)$$

where the dependence on the $SU(N)$ color group is shown explicitly, ($V = N^2 - 1$, $N = 3$). The matrix elements squared in Eqs. (4,5) have been summed and averaged over initial and final colours and spins, (as indicated by $\overline{\sum}$). For brevity, in these formulae, we have introduced the notation $p_i \cdot p_j = \{ij\}$ for the scalar product of two four-momenta. The short distance cross sections are given in terms of the invariant matrix elements squared by

$$\frac{E_3 d\hat{\sigma}}{d^3P_3} = \frac{1}{64\pi^2\{12\}} \overline{\sum} |M|^2 \delta(\{12\} - \{13\} - \{23\}). \quad (6)$$

The corrections to the parton model formula, Eq.(2), are of two types. They are either higher order perturbative corrections which are suppressed by the presence of additional powers of $\alpha_s(Q^2)$, or power corrections suppressed by inverse powers of the heavy quark mass.

In general terms the phenomenological consequences of Eq. (2) can be summarised as follows. Processes (a) and (b) lead to a cross section for the production of charmed particles which is predominantly central.⁷ By kinematics, the transverse momentum of the heavy quark or antiquark is, on the average, of the order of its mass, whereas the transverse momentum of the quark-antiquark pair is controlled by the transverse momenta of the incoming partons and is hence small.

The theoretical arguments summarized above do not address the issue of whether the charmed quark is sufficiently heavy that the hadroproduction of charmed hadrons in all regions of phase space is described via this mechanism. In fact there is evidence the hard scattering picture alone cannot provide a complete description of all data on charm production. Some experiments^{1,12} have reported nuclear target dependences, ($\sigma \propto A^\alpha$ where $\alpha \neq 1$), which cannot be accommodated by the hard scattering picture which requires $\alpha = 1$. There is also evidence^{1,13} that the production of charmed particles which share quarks with the target beam is enhanced in the forward direction. In preparing the curves given in this paper we have used the hard scattering picture which does not include these effects. This we do partly for expediency, since no entirely convincing model of these effects exists, and also because we do not find the experimental situation entirely compelling. Note also that such effects are suppressed relative to Eq. (2) by inverse powers of the heavy quark mass and hence will be less important for quarks heavier than charm.

The cross section curves which we present in the next section will show that, at the beam energies which we investigate, there is great sensitivity to the value of the

heavy quark mass. Principally this sensitivity reflects the fact that a variation in the quark mass changes the longitudinal momentum fraction x of the incoming parton distributions which is probed. Faced with this uncertainty, we have adopted two extreme values for the mass of the heavy quarks. The values which we have chosen are for the charmed quark, $1.2 \text{ GeV}/c^2 < m_c < 1.8 \text{ GeV}/c^2$ and for the bottom quark $4.7 \text{ GeV}/c^2 < m_b < 5.3 \text{ GeV}/c^2$. The quark cross sections which we present are predictions for the total cross sections for open and hidden charm or beauty. Thus in the case of charm the curves given correspond to the sum of the cross-sections for $J/\psi, \psi'$ and all associated states below threshold as well as the production of charmed mesons and baryons. This duality is familiar from e^+e^- physics where the parton model result corresponds to both the resonance structure below threshold and continuum above the threshold for the production of open charm.

Of interest for the planning and execution of experiments is the question of the relative efficiency of pion and proton beams for the production of heavy flavors. In the comparison of these two processes the uncertainty due to the mass of the heavy quark is less acute. A preliminary look¹⁴ suggested that πN interactions may have important advantages over pN interactions for $b\bar{b}$ production at Tevatron II energies, because the yield of bottom quarks is larger in πN collisions, and because the smaller πN total cross section implies a smaller background to the heavy flavors. In this note we present a considerably more detailed picture of cross sections for the production of both charmed and bottom quarks. We confirm the earlier conclusion that pion beams are more efficient for b -quark production than proton beams of somewhat higher energy. This comes as no surprise, because the elements of the calculation are unchanged. In addition, particularly for experiments sensitive to forward production of heavy flavors, we find that pion beams hold an advantage for the production of charm as well. A general conclusion is that choosing a pion beam to enhance the prospects of a search for b -quarks will not compromise the yield of charmed particles.

II. RESULTS FOR CHARM

We have calculated rates for heavy flavor production via the elementary two-body processes (a) and (b) using the pion structure functions of Owens¹⁵ and, for consistency, the nucleon structure functions of Duke and Owens.¹⁶ For the strong coupling constant we use the standard one-loop expression

$$1/\alpha_s(Q^2) = \frac{27}{12\pi} \log \frac{Q^2}{\Lambda^2} - \frac{1}{6\pi} \sum_{i=c,b,\dots} \theta(Q^2 - 4m_i^2) \log(Q^2/4m_i^2) \quad (7)$$

with $\Lambda = 200$ MeV. In both the structure functions and the strong coupling constant we take $Q^2 = 4m_c^2$. The cross sections are calculated for an "isoscalar nucleon" $N \equiv (p+n)/2$. The results we present refer to the cross sections for producing *either* a quark *or* an antiquark (*not summed*). This must be kept in mind in comparing with experimental results.

The integrated cross sections for charm production in πN and pN collisions are shown in Fig. 1 for charmed quark masses $m_c = 1.2, 1.8$ GeV/c². There is considerable sensitivity to the quark mass: the rates differ by nearly an order of magnitude for the two choices. As indicated above the values which we have chosen for the quark masses are intended to be limiting values.

Whatever choice is made for the quark mass, there is little difference between production rates in pion beams and proton beams. When attention is restricted to forward production ($x_F > 0.2$), pion beams produce charm at about twice the rate of proton beams, as shown in Fig. 2. We show in Fig. 3 the contribution of the gluon fusion process (b) to charm production. It accounts for essentially the full cross section shown in Fig. 1. Thus the advantage of the pion beam for charm production lies principally in the harder gluon distribution, proportional to $(1-x)^{3.1}$ versus $(1-x)^6$ for the proton, not in the contribution of valence antiquarks.

The longitudinal momentum (or Feynman x_F) distribution $d\sigma/dx_F$ is shown in Figs. 4-9 for beam momenta from 300 to 800 GeV/c. Here we see that the entire difference between pion and proton cross sections occurs for forward production.

The transverse momentum distributions $d\sigma/dp_{\perp}^2$ are shown in Figs. 10-21 for the full range of Feynman x_F , and for the forward range $x_F > 0.2$. The pion beam produces charms with somewhat larger values of the transverse momentum, and this tendency is enhanced for forward production.

In Figs. 22-25 we show three-dimensional and isopleth representations of the proton-induced and pion-induced charm cross sections for $m_c = 1.5$ GeV/c² and beam momentum of 600 GeV/c.

Another class of processes contributes significantly to the production of charmed particles^{17,18}. As first observed by Kunszt and Pietarinen,¹⁷ because of the large cross-section for the production of gluon jets at large transverse momentum the process



is likely to be the principal source of heavy quarks, especially at large transverse momentum ($q_T \gg m$). This mechanism might give a large contribution to heavy particle production because the ratio of the relevant $2 \rightarrow 2$ matrix elements is extremely large. In fact, at 90 degrees in the parton-parton center of mass, the

gluon fusion mechanism is much more likely to produce a gluon than a quark.

$$\frac{\sum |M(ss \rightarrow ss)|^2}{\sum |M(ss \rightarrow qq)|^2} \approx 200 \quad (9)$$

The validity of this schematic reasoning has been confirmed by analysis of the full $2 \rightarrow 3$ matrix elements including mass effects.^{17,18,19} A numerical example is shown in Fig. 26 for charm production in 800 GeV/c pN collisions with $m_c = 1.2$ GeV/c². It is important to note that in the absence of a complete $O(\alpha_s^3)$ calculation Fig. 26, which compares the p_T distribution of a single charmed quark in $O(\alpha_s^2)$ with the p_T distribution of a pair of charmed quarks in $O(\alpha_s^3)$ is the best that one can do. It is therefore likely that charm particle production at large p_T will be predominantly due to $2 \rightarrow 3$ processes. Note that the $2 \rightarrow 3$ processes will give rise to a different topology of event where both charmed particles lie within the same jet.

III. RESULTS FOR BOTTOM

We proceed as for charm, this time setting $Q^2 = 4m_b^2$ in both the running coupling and the parton distribution functions. The integrated cross sections for bottom production in πN and pN collisions are shown in Fig. 27 for bottom quark masses $m_b = 4.7, 5.3$ GeV/c². As was the case for charm, there is considerable sensitivity to the quark mass, now at the level of a factor of three to four. In both cases, there is a significant advantage for the pion beam. This advantage is enhanced when attention is restricted to forward production ($x_F > 0.2$), as shown in Fig. 28. The comparison between the full range of longitudinal momentum and forward production is shown for pN collisions in Fig. 29, and for πN collisions in Fig. 30. In Figs. 31 and 32 we show the contributions to bottom production in pN collisions for bottom quark masses $m_b = 4.7$ and 5.3 GeV/c², respectively. In both cases the gluon fusion mechanism (b) is dominant, except at the lowest energies. For πN collisions, the situation is quite different, as shown for the two bottom quark masses in Figs. 33 and 34: The $q\bar{q}$ annihilation process (a) is pre-eminent, with gluon fusion contributing significantly only at the highest energies. The prominence of mechanism (a) is owed to the valence antiquarks in the pion.

The longitudinal momentum (or Feynman x_F) distribution $d\sigma/dx_F$ is shown in Figs. 35-40 for beam momenta from 300 to 800 GeV/c. In contrast to what we noted for charm production, here the pion beam is favored at all values of x_F .

The transverse momentum distributions $d\sigma/dp_\perp^2$ are shown in Figs. 41-52 for the full range of Feynman x_F , and for the forward range $x_F > 0.2$. The pion beam produces bottoms with somewhat larger values of the transverse momentum, and this tendency is enhanced for forward production.

In Figs. 53-56 we show three-dimensional and isopleth representations of the proton-induced and pion-induced bottom cross sections for $m_b = 5.3 \text{ GeV}/c^2$ and beam momentum of $600 \text{ GeV}/c$.

IV. CONCLUSIONS

We have presented detailed curves which describe the production of charm and beauty quarks at the energies of fixed target machines. Our curves display a great sensitivity to the value chosen for the heavy quark mass. Conversely, this indicates that the hadroproduction of charm is a good place to measure this parameter. We have not included the decay functions which describe the hadronisation of heavy quarks into specific final states. Thus the most conservative approach is to regard our curves as upper bounds on the cross sections for the production of mesons and baryons.

The comparison between pion and proton beams is less subject to these uncertainties and indicates that pions are as efficient as protons for the production of charm, and display significant advantages in the case of beauty.

FOOTNOTES AND REFERENCES

- [1] For a review see A. Kernan and G. VanDalen, *Phys. Rep.* **106**, 298 (1984); J. L. Ritchie, in *Proc. 1984 Summer Study on the Design and Utilization of the Superconducting Super Collider*, R. Donaldson and J. Morfin, (eds.), Fermilab, Batavia, Illinois, 1984, p. 237, and references therein.
- [2] J. P. Albanese *et al.*, *Phys. Lett.* **158B**, 186 (1985);
M. G. Catanesi *et al.* CERN EP/86-177 (1986);
C. Albajar *et al.*, CERN-EP/86 - 208 (1986)
- [3] G. Arnison *et al.*, *Phys. Lett.* **147B**, 493 (1984).
- [4] J. C Anjos *et al.* *Phys. Rev. Lett.* **58**, xx (1987)
- [5] J. C. Collins, D. E. Soper, and G. Sterman, *Nucl. Phys.* **B263**, 37 (1986);
P. Mazzanti and S. Wada, *Phys. Rev.* **D26**, 602 (1982).
- [6] S. J. Brodsky, J. C. Collins, S.D. Ellis, J. F. Gunion and A. H. Mueller, in *Proc. 1984 Summer Study on the Design and Utilization of the Superconducting Super Collider*, R. Donaldson and J. Morfin, (eds.), Fermilab, Batavia, Illinois, 1984, p. 227.

- [7] R. K. Ellis, in *Strong Interactions and Gauge Theories*, edited by J. Tran Thanh Van, Editions Frontières, Gif-sur-Yvette, 1986, p. 339.
- [8] see for example, G. Altarelli, *Phys. Rep.* **81**, 1 (1982);
- [9] B. L. Combridge, *Nucl. Phys.* **B151**, 4299 (1979).
- [10] J. Babcock, D. Sivers and S. Wolfram, *Phys. Rev.* **D18**, 162 (1978).
- [11] K. Hagiwara and T. Yoshino, *Phys. Lett.* **80B**, 282 (1979);
L. M. Jones and H. Wyld, *Phys. Rev.* **D17**, 782 (1978);
H. Georgi *et al.*, *Ann. Phys. (NY)* **114**, 273 (1978).
- [12] M. E. Duffy *et al.*, *Phys. Rev. Lett.* **55**, 1816 (1985);
- [13] M. Aguilar-Benitez *et al.*, *Phys. Lett.* **161B**, 400 (1985);
- [14] C. Quigg, "b \bar{b} Production in Tevatron II Experiments," memorandum, July, 1985 (unpublished).
- [15] J. F. Owens, *Phys. Rev.* **D30**, 983 (1984).
- [16] D. W. Duke and J. F. Owens, *Phys. Rev.* **D30**, 49 (1984).
- [17] Z. Kunszt and E. Pietarinen, *Nucl. Phys.* **B164**, 45 (1980);
- [18] F. Halzen and G. Herzog, *Phys. Rev.* **D30**, 2326 (1984);
F. Halzen and P. Hoyer, *Phys. Lett.* **154B**, 324 (1985);
V. Barger and R. J. N. Phillips, *Phys. Rev.* **D31**, 215 (1985);
A. Ali and G. Ingelman, *Phys. Lett.* **156B**, 111 (1985);
G. Kopp, J. H. Kühn and P. Zerwas, CERN preprint CERN-TH-4081 (1984);
E. W. N. Glover, *et al.*, *Phys. Lett.* **168B**, 289 (1986).
- [19] R. K. Ellis and J. C. Sexton, *Nucl. Phys.* **B282**, 642 (1987)

FIGURE CAPTIONS

- Figure 1: Integrated cross sections for the production of charmed quarks in πN (solid lines) and pN (dashed lines) collisions.
- Figure 2: Integrated cross sections for the forward production ($x_F > 0.2$) of charmed quarks in πN (solid lines) and pN (dashed lines) collisions.
- Figure 3: Contribution of gluon fusion to the integrated cross sections for the production of charmed quarks in πN (solid lines) and pN (dashed lines) collisions.
- Figure 4: Differential cross section $d\sigma/dx_F$ for the production of charmed quarks in πN (solid lines) and pN (dashed lines) collisions at $\sqrt{s} = 23.7$ GeV ($p_{beam} = 300$ GeV/c).
- Figure 5: Differential cross section $d\sigma/dx_F$ for the production of charmed quarks in πN (solid lines) and pN (dashed lines) collisions at $\sqrt{s} = 27.4$ GeV ($p_{beam} = 400$ GeV/c).
- Figure 6: Differential cross section $d\sigma/dx_F$ for the production of charmed quarks in πN (solid lines) and pN (dashed lines) collisions at $\sqrt{s} = 30.6$ GeV ($p_{beam} = 500$ GeV/c).
- Figure 7: Differential cross section $d\sigma/dx_F$ for the production of charmed quarks in πN (solid lines) and pN (dashed lines) collisions at $\sqrt{s} = 33.6$ GeV ($p_{beam} = 600$ GeV/c).
- Figure 8: Differential cross section $d\sigma/dx_F$ for the production of charmed quarks in πN (solid lines) and pN (dashed lines) collisions at $\sqrt{s} = 36.3$ GeV ($p_{beam} = 700$ GeV/c).
- Figure 9: Differential cross section $d\sigma/dx_F$ for the production of charmed quarks in πN (solid lines) and pN (dashed lines) collisions at $\sqrt{s} = 38.8$ GeV ($p_{beam} = 800$ GeV/c).
- Figure 10: Differential cross section $d\sigma/dp_{\perp}^2$ for the production of charmed quarks in πN (solid lines) and pN (dashed lines) collisions at $\sqrt{s} = 23.7$ GeV ($p_{beam} = 300$ GeV/c).
- Figure 11: Differential cross section $d\sigma/dp_{\perp}^2$ for the forward production ($x_F > 0.2$) of charmed quarks in πN (solid lines) and pN (dashed lines) collisions at $\sqrt{s} = 23.7$ GeV ($p_{beam} = 300$ GeV/c).

- Figure 12: Differential cross section $d\sigma/dp_{\perp}^2$ for the production of charmed quarks in πN (solid lines) and pN (dashed lines) collisions at $\sqrt{s} = 27.4$ GeV ($p_{beam} = 400$ GeV/c).
- Figure 13: Differential cross section $d\sigma/dp_{\perp}^2$ for the forward production ($x_F > 0.2$) of charmed quarks in πN (solid lines) and pN (dashed lines) collisions at $\sqrt{s} = 27.4$ GeV ($p_{beam} = 400$ GeV/c).
- Figure 14: Differential cross section $d\sigma/dp_{\perp}^2$ for the production of charmed quarks in πN (solid lines) and pN (dashed lines) collisions at $\sqrt{s} = 30.6$ GeV ($p_{beam} = 500$ GeV/c).
- Figure 15: Differential cross section $d\sigma/dp_{\perp}^2$ for the forward production ($x_F > 0.2$) of charmed quarks in πN (solid lines) and pN (dashed lines) collisions at $\sqrt{s} = 30.6$ GeV ($p_{beam} = 500$ GeV/c).
- Figure 16: Differential cross section $d\sigma/dp_{\perp}^2$ for the production of charmed quarks in πN (solid lines) and pN (dashed lines) collisions at $\sqrt{s} = 33.6$ GeV ($p_{beam} = 600$ GeV/c).
- Figure 17: Differential cross section $d\sigma/dp_{\perp}^2$ for the forward production ($x_F > 0.2$) of charmed quarks in πN (solid lines) and pN (dashed lines) collisions at $\sqrt{s} = 33.6$ GeV ($p_{beam} = 600$ GeV/c).
- Figure 18: Differential cross section $d\sigma/dp_{\perp}^2$ for the production of charmed quarks in πN (solid lines) and pN (dashed lines) collisions at $\sqrt{s} = 36.3$ GeV ($p_{beam} = 700$ GeV/c).
- Figure 19: Differential cross section $d\sigma/dp_{\perp}^2$ for the forward production ($x_F > 0.2$) of charmed quarks in πN (solid lines) and pN (dashed lines) collisions at $\sqrt{s} = 36.3$ GeV ($p_{beam} = 700$ GeV/c).
- Figure 20: Differential cross section $d\sigma/dp_{\perp}^2$ for the production of charmed quarks in πN (solid lines) and pN (dashed lines) collisions at $\sqrt{s} = 38.8$ GeV ($p_{beam} = 800$ GeV/c).
- Figure 21: Differential cross section $d\sigma/dp_{\perp}^2$ for the forward production ($x_F > 0.2$) of charmed quarks in πN (solid lines) and pN (dashed lines) collisions at $\sqrt{s} = 38.8$ GeV ($p_{beam} = 800$ GeV/c).
- Figure 22: Three-dimensional representation of $\log E d\sigma/d^3p$ for the production of charmed quarks with $m_c = 1.5$ GeV/c² in 600 GeV/c pN collisions.
- Figure 23: Contour plot of $E d\sigma/d^3p$ for the production of charmed quarks with $m_c = 1.5$ GeV/c² in 600 GeV/c pN collisions.

- Figure 24: Three-dimensional representation of $\log E d\sigma/d^3p$ for the production of charmed quarks with $m_c = 1.5 \text{ GeV}/c^2$ in $600 \text{ GeV}/c$ πN collisions.
- Figure 25: Contour plot of $E d\sigma/d^3p$ for the production of charmed quarks with $m_c = 1.5 \text{ GeV}/c^2$ in $600 \text{ GeV}/c$ πN collisions.
- Figure 26: Relative importance of two-to-two and two-to-three processes.
- Figure 27: Integrated cross sections for the production of bottom quarks in πN (solid lines) and pN (dashed lines) collisions.
- Figure 28: Integrated cross sections for the forward production ($x_F > 0.2$) of bottom quarks in πN (solid lines) and pN (dashed lines) collisions.
- Figure 29: Integrated cross sections for the production of bottom quarks in pN collisions, for all x_F (solid lines), and restricted to $x_F > 0.2$ (dashed lines).
- Figure 30: Integrated cross sections for the production of bottom quarks in πN collisions, for all x_F (solid lines), and restricted to $x_F > 0.2$ (dashed lines).
- Figure 31: Contributions to the cross section for the production of bottom quarks in pN collisions, for $m_b = 4.7 \text{ GeV}/c^2$.
- Figure 32: Contributions to the cross section for the production of bottom quarks in pN collisions, for $m_b = 5.3 \text{ GeV}/c^2$.
- Figure 33: Contributions to the cross section for the production of bottom quarks in πN collisions, for $m_b = 4.7 \text{ GeV}/c^2$.
- Figure 34: Contributions to the cross section for the production of bottom quarks in πN collisions, for $m_b = 5.3 \text{ GeV}/c^2$.
- Figure 35: Differential cross section $d\sigma/dx_F$ for the production of bottom quarks in πN (solid lines) and pN (dashed lines) collisions at $\sqrt{s} = 23.7 \text{ GeV}$ ($p_{beam} = 300 \text{ GeV}/c$).
- Figure 36: Differential cross section $d\sigma/dx_F$ for the production of bottom quarks in πN (solid lines) and pN (dashed lines) collisions at $\sqrt{s} = 27.4 \text{ GeV}$ ($p_{beam} = 400 \text{ GeV}/c$).
- Figure 37: Differential cross section $d\sigma/dx_F$ for the production of bottom quarks in πN (solid lines) and pN (dashed lines) collisions at $\sqrt{s} = 30.6 \text{ GeV}$ ($p_{beam} = 500 \text{ GeV}/c$).

- Figure 38: Differential cross section $d\sigma/dx_F$ for the production of bottom quarks in πN (solid lines) and pN (dashed lines) collisions at $\sqrt{s} = 33.6$ GeV ($p_{beam} = 600$ GeV/c).
- Figure 39: Differential cross section $d\sigma/dx_F$ for the production of bottom quarks in πN (solid lines) and pN (dashed lines) collisions at $\sqrt{s} = 36.3$ GeV ($p_{beam} = 700$ GeV/c).
- Figure 40: Differential cross section $d\sigma/dx_F$ for the production of bottom quarks in πN (solid lines) and pN (dashed lines) collisions at $\sqrt{s} = 38.8$ GeV ($p_{beam} = 800$ GeV/c).
- Figure 41: Differential cross section $d\sigma/dp_{\perp}^2$ for the production of bottom quarks in πN (solid lines) and pN (dashed lines) collisions at $\sqrt{s} = 23.7$ GeV ($p_{beam} = 300$ GeV/c).
- Figure 42: Differential cross section $d\sigma/dp_{\perp}^2$ for the forward production ($x_F > 0.2$) of bottom quarks in πN (solid lines) and pN (dashed lines) collisions at $\sqrt{s} = 23.7$ GeV ($p_{beam} = 300$ GeV/c).
- Figure 43: Differential cross section $d\sigma/dp_{\perp}^2$ for the production of bottom quarks in πN (solid lines) and pN (dashed lines) collisions at $\sqrt{s} = 27.4$ GeV ($p_{beam} = 400$ GeV/c).
- Figure 44: Differential cross section $d\sigma/dp_{\perp}^2$ for the forward production ($x_F > 0.2$) of bottom quarks in πN (solid lines) and pN (dashed lines) collisions at $\sqrt{s} = 27.4$ GeV ($p_{beam} = 400$ GeV/c).
- Figure 45: Differential cross section $d\sigma/dp_{\perp}^2$ for the production of bottom quarks in πN (solid lines) and pN (dashed lines) collisions at $\sqrt{s} = 30.6$ GeV ($p_{beam} = 500$ GeV/c).
- Figure 46: Differential cross section $d\sigma/dp_{\perp}^2$ for the forward production ($x_F > 0.2$) of bottom quarks in πN (solid lines) and pN (dashed lines) collisions at $\sqrt{s} = 30.6$ GeV ($p_{beam} = 500$ GeV/c).
- Figure 47: Differential cross section $d\sigma/dp_{\perp}^2$ for the production of bottom quarks in πN (solid lines) and pN (dashed lines) collisions at $\sqrt{s} = 33.6$ GeV ($p_{beam} = 600$ GeV/c).
- Figure 48: Differential cross section $d\sigma/dp_{\perp}^2$ for the forward production ($x_F > 0.2$) of bottom quarks in πN (solid lines) and pN (dashed lines) collisions at $\sqrt{s} = 33.6$ GeV ($p_{beam} = 600$ GeV/c).

- Figure 49: Differential cross section $d\sigma/dp_{\perp}^2$ for the production of bottom quarks in πN (solid lines) and pN (dashed lines) collisions at $\sqrt{s} = 36.3$ GeV ($p_{beam} = 700$ GeV/c).
- Figure 50: Differential cross section $d\sigma/dp_{\perp}^2$ for the forward production ($x_F > 0.2$) of bottom quarks in πN (solid lines) and pN (dashed lines) collisions at $\sqrt{s} = 36.3$ GeV ($p_{beam} = 700$ GeV/c).
- Figure 51: Differential cross section $d\sigma/dp_{\perp}^2$ for the production of bottom quarks in πN (solid lines) and pN (dashed lines) collisions at $\sqrt{s} = 38.8$ GeV ($p_{beam} = 800$ GeV/c).
- Figure 52: Differential cross section $d\sigma/dp_{\perp}^2$ for the forward production ($x_F > 0.2$) of bottom quarks in πN (solid lines) and pN (dashed lines) collisions at $\sqrt{s} = 38.8$ GeV ($p_{beam} = 800$ GeV/c).
- Figure 53: Three-dimensional representation of $\log E d\sigma/d^3p$ for the production of bottom quarks with $m_b = 5.3$ GeV/c² in 600 GeV/c pN collisions.
- Figure 54: Contour plot of $\log E d\sigma/d^3p$ for the production of bottom quarks with $m_b = 5.3$ GeV/c² in 600 GeV/c pN collisions.
- Figure 55: Three-dimensional representation of $\log E d\sigma/d^3p$ for the production of bottom quarks with $m_b = 5.3$ GeV/c² in 600 GeV/c πN collisions.
- Figure 56: Contour plot of $\log E d\sigma/d^3p$ for the production of bottom quarks with $m_b = 5.3$ GeV/c² in 600 GeV/c πN collisions.

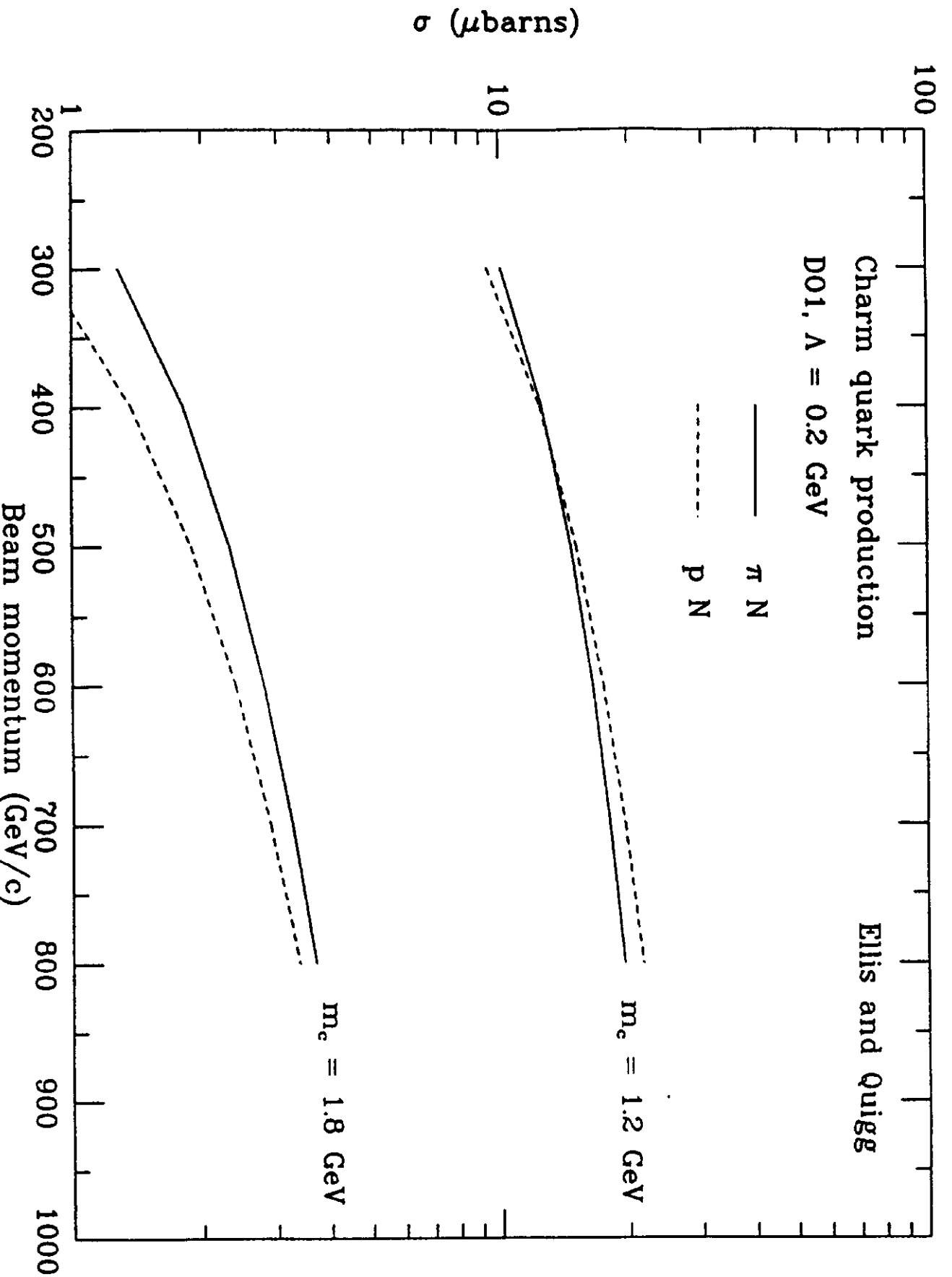


Figure 1: Integrated cross sections for the production of charmed quarks in πN (solid lines) and $p N$ (dashed lines) collisions.

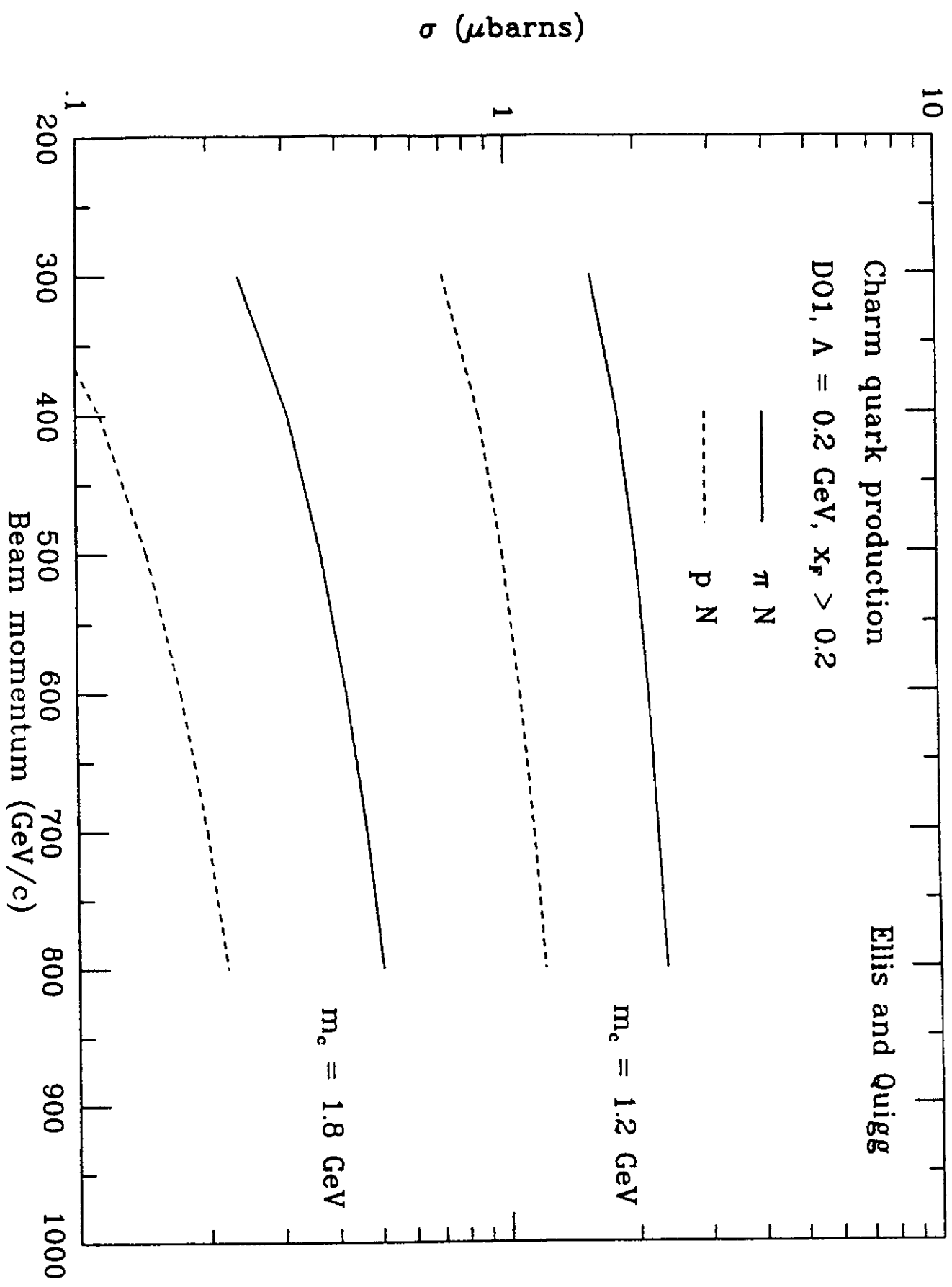


Figure 2: Integrated cross sections for the forward production ($x_F > 0.2$) of charmed quarks in πN (solid lines) and pN (dashed lines) collisions.

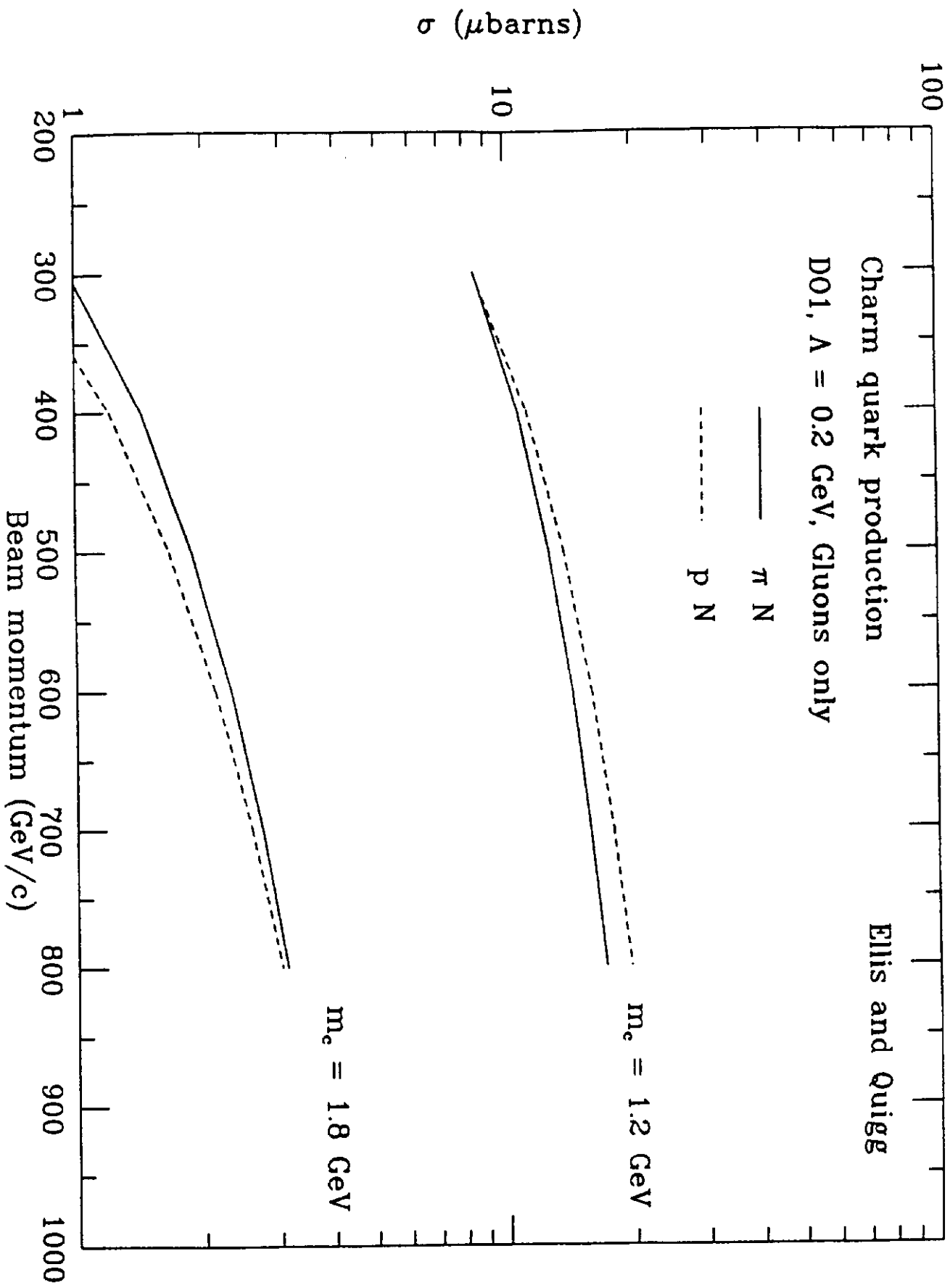


Figure 3: Contribution of gluon fusion to the integrated cross sections for the production of charmed quarks in πN (solid lines) and pN (dashed lines) collisions.

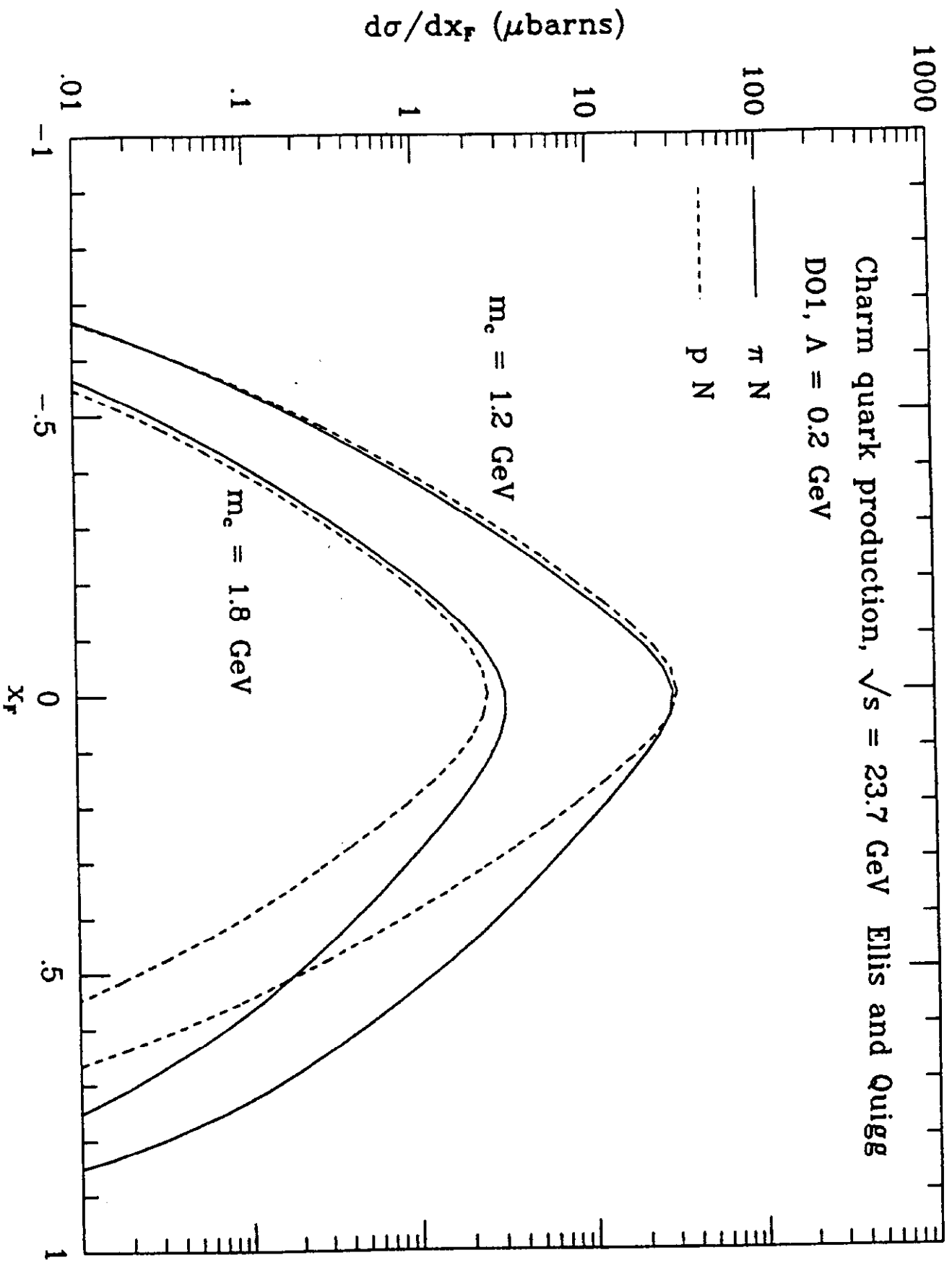


Figure 4: Differential cross section $d\sigma/dx_f$ for the production of charmed quarks in πN (solid lines) and pN (dashed lines) collisions at $\sqrt{s} = 23.7 \text{ GeV}$ ($p_{beam} = 300 \text{ GeV}/c$).

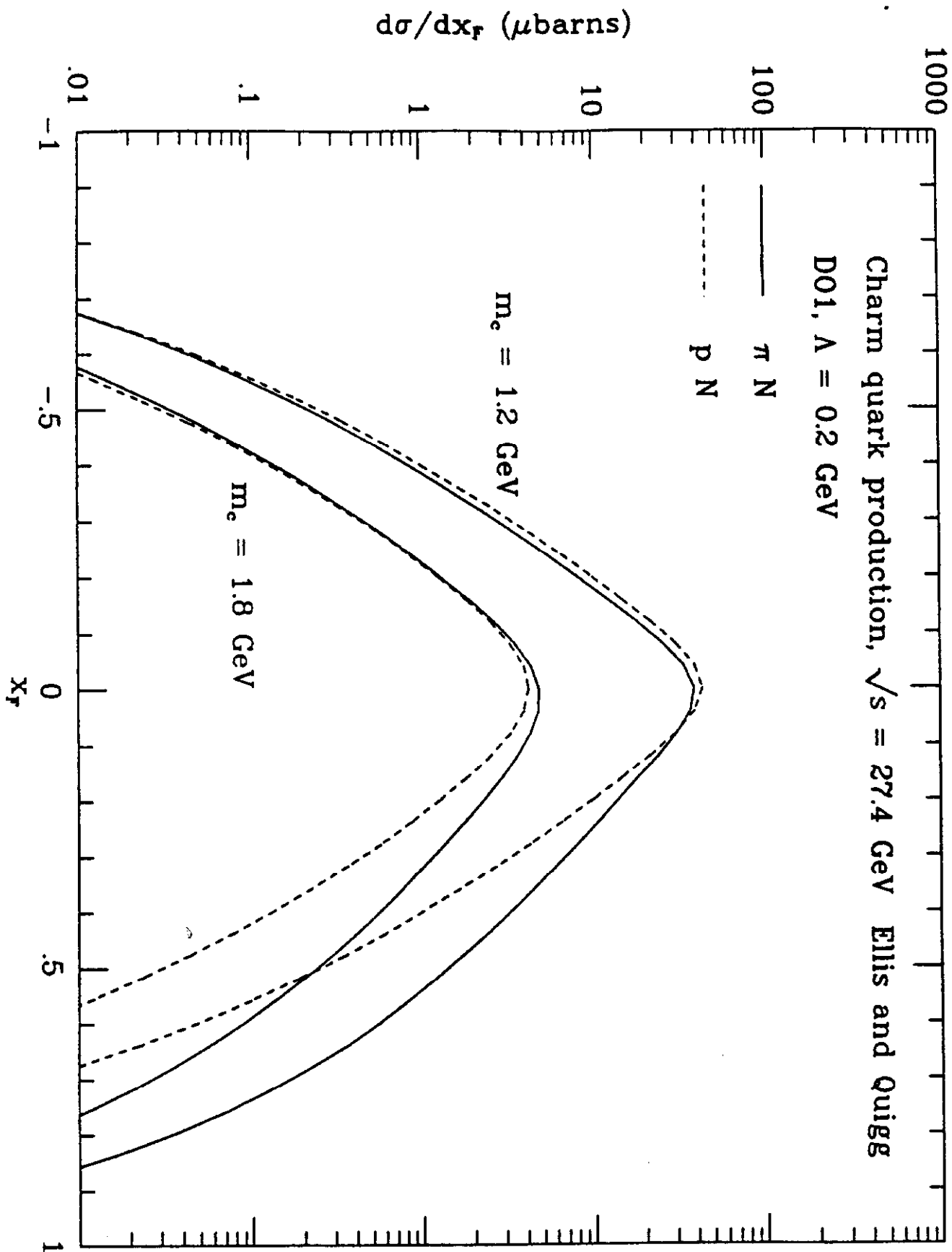


Figure 5: Differential cross section $d\sigma/dx_f$ for the production of charmed quarks in πN (solid lines) and pN (dashed lines) collisions at $\sqrt{s} = 27.4$ GeV ($p_{beam} = 400$ GeV/c).

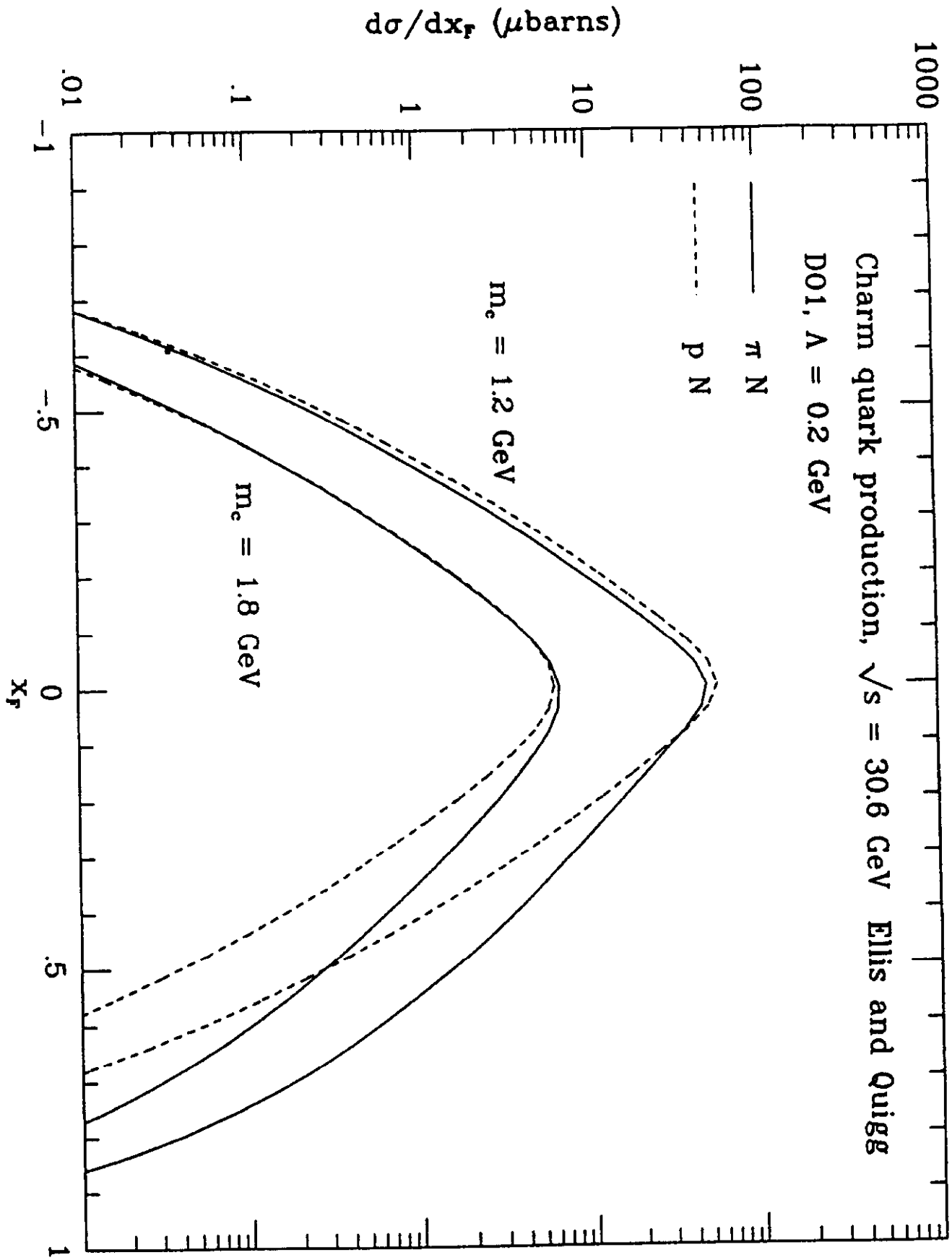


Figure 6: Differential cross section $d\sigma/dx_f$ for the production of charmed quarks in πN (solid lines) and pN (dashed lines) collisions at $\sqrt{s} = 30.6$ GeV ($p_{beam} = 500$ GeV/c).

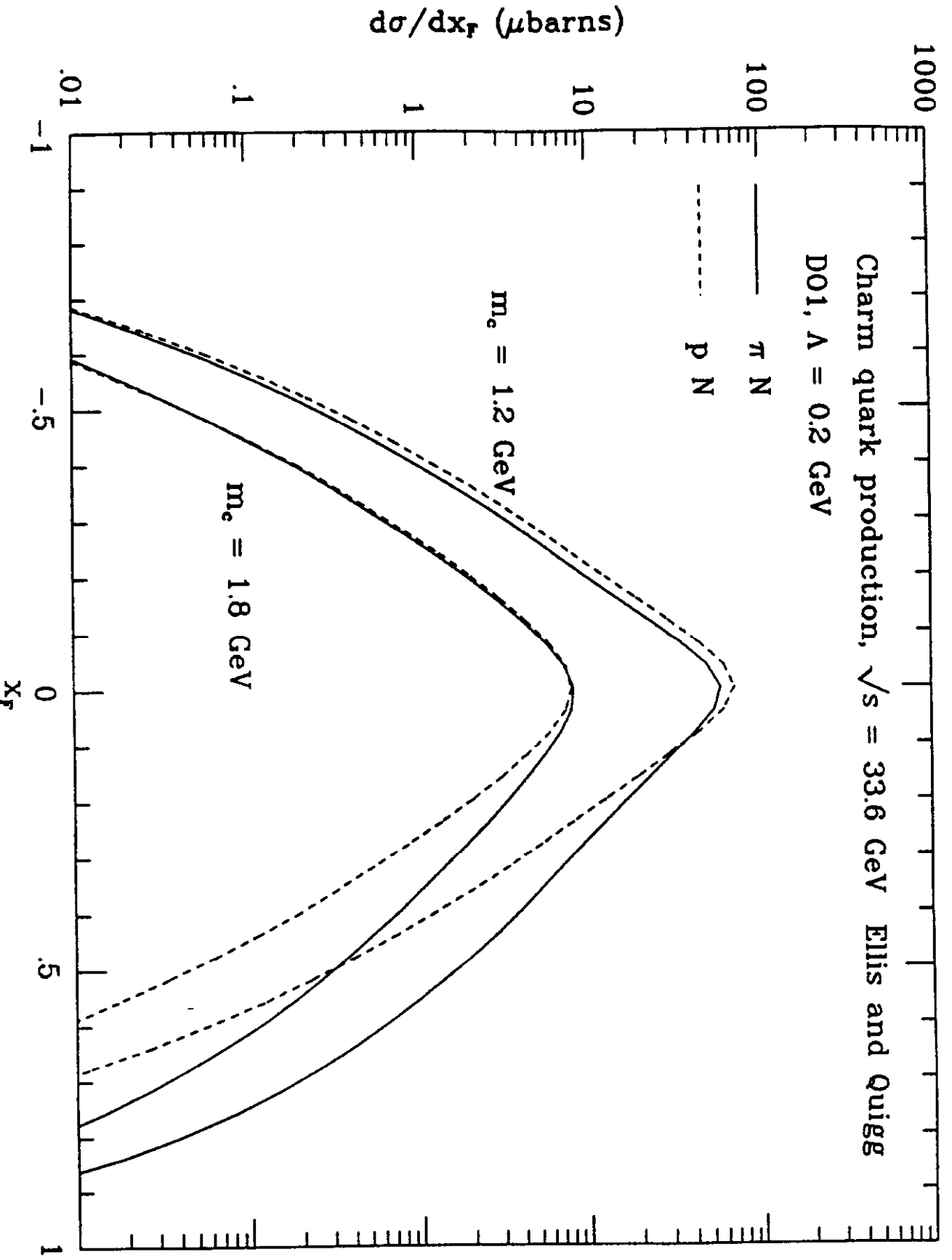


Figure 7: Differential cross section $d\sigma/dx_f$ for the production of charmed quarks in πN (solid lines) and pN (dashed lines) collisions at $\sqrt{s} = 33.6$ GeV ($p_{beam} = 600$ GeV/c).

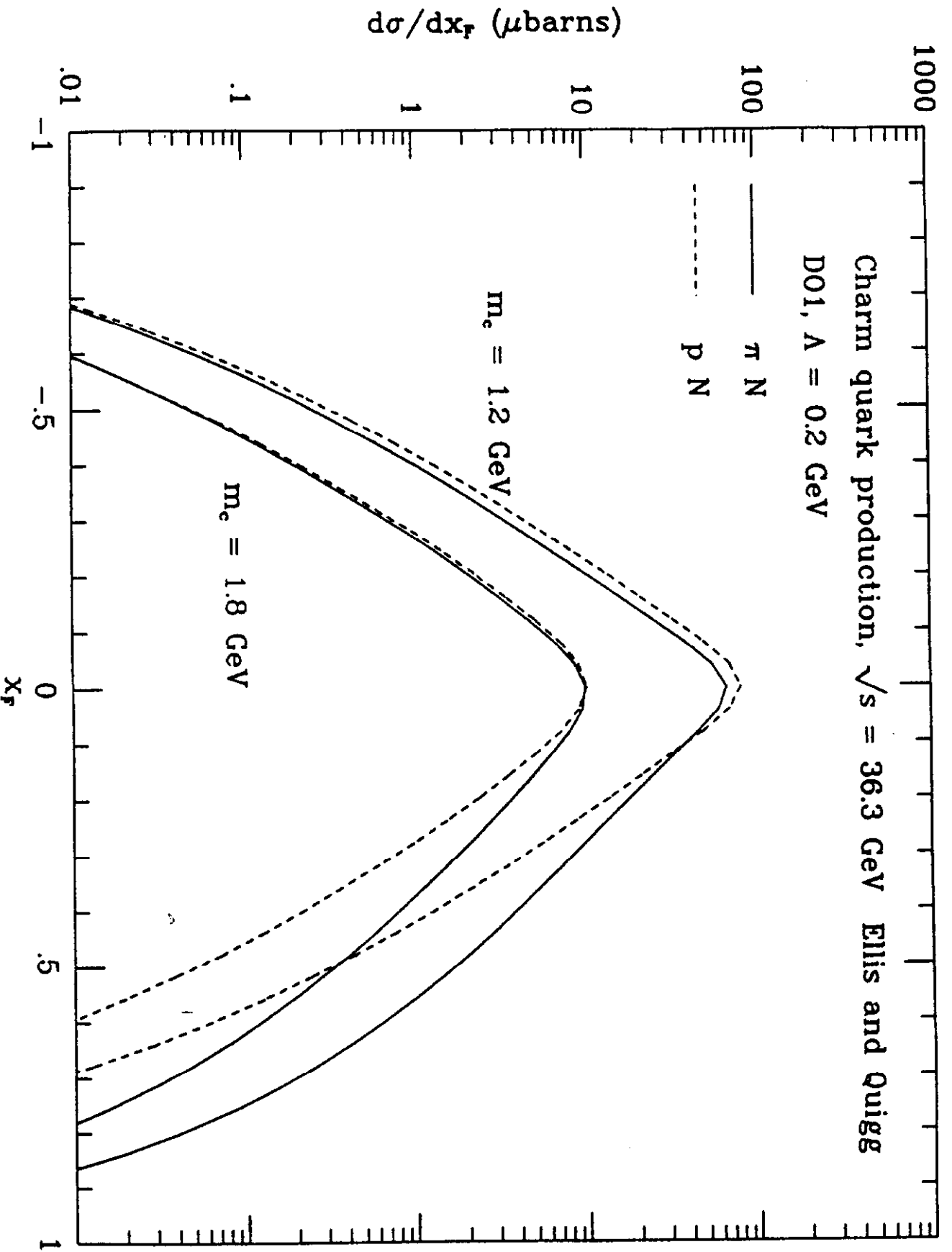


Figure 8: Differential cross section $d\sigma/dx_f$ for the production of charmed quarks in πN (solid lines) and pN (dashed lines) collisions at $\sqrt{s} = 36.3$ GeV ($p_{beam} = 700$ GeV/c).

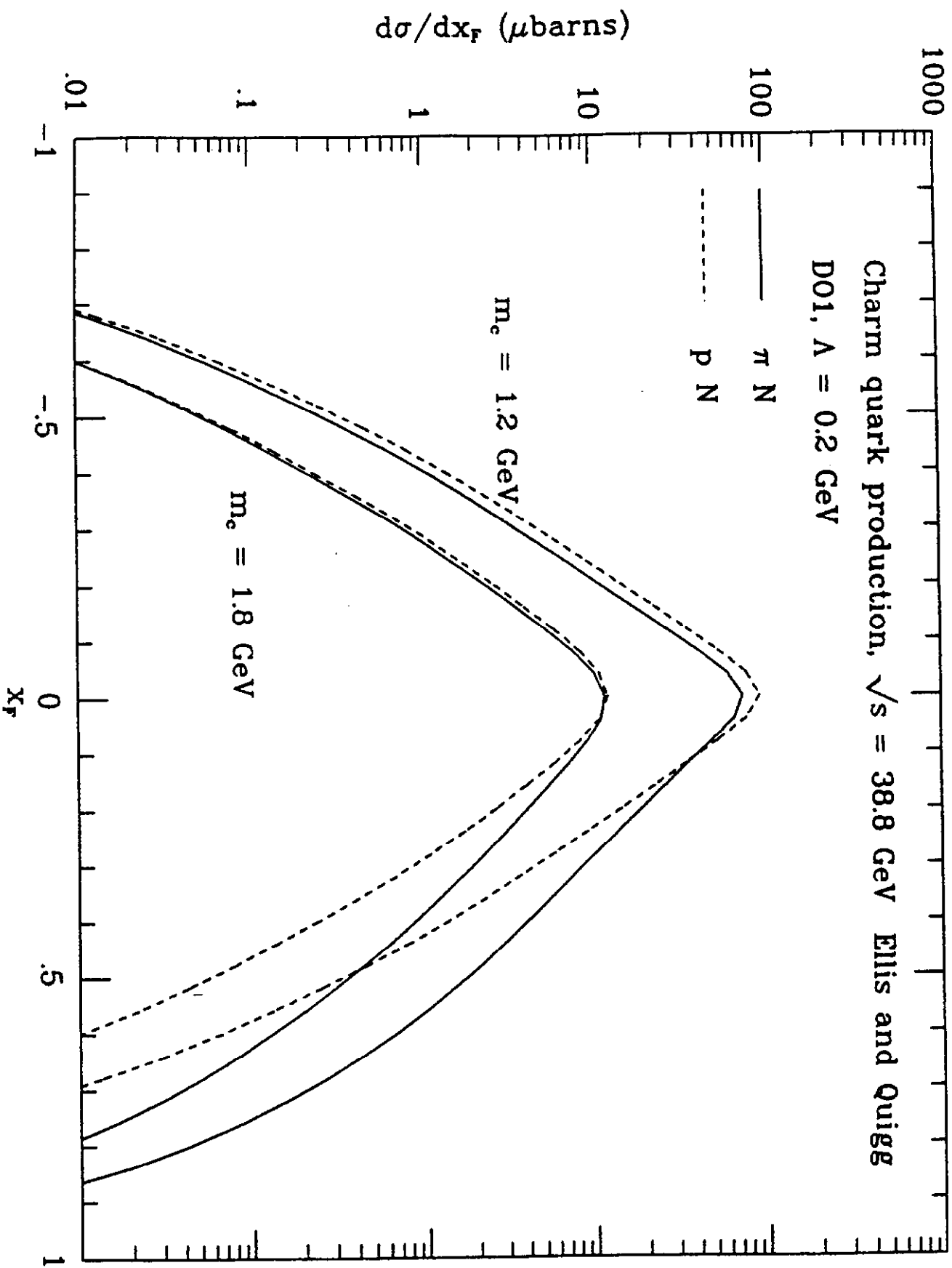


Figure 9: Differential cross section $d\sigma/dx_f$ for the production of charmed quarks in πN (solid lines) and pN (dashed lines) collisions at $\sqrt{s} = 38.8 \text{ GeV}$ ($p_{beam} = 800 \text{ GeV}/c$).

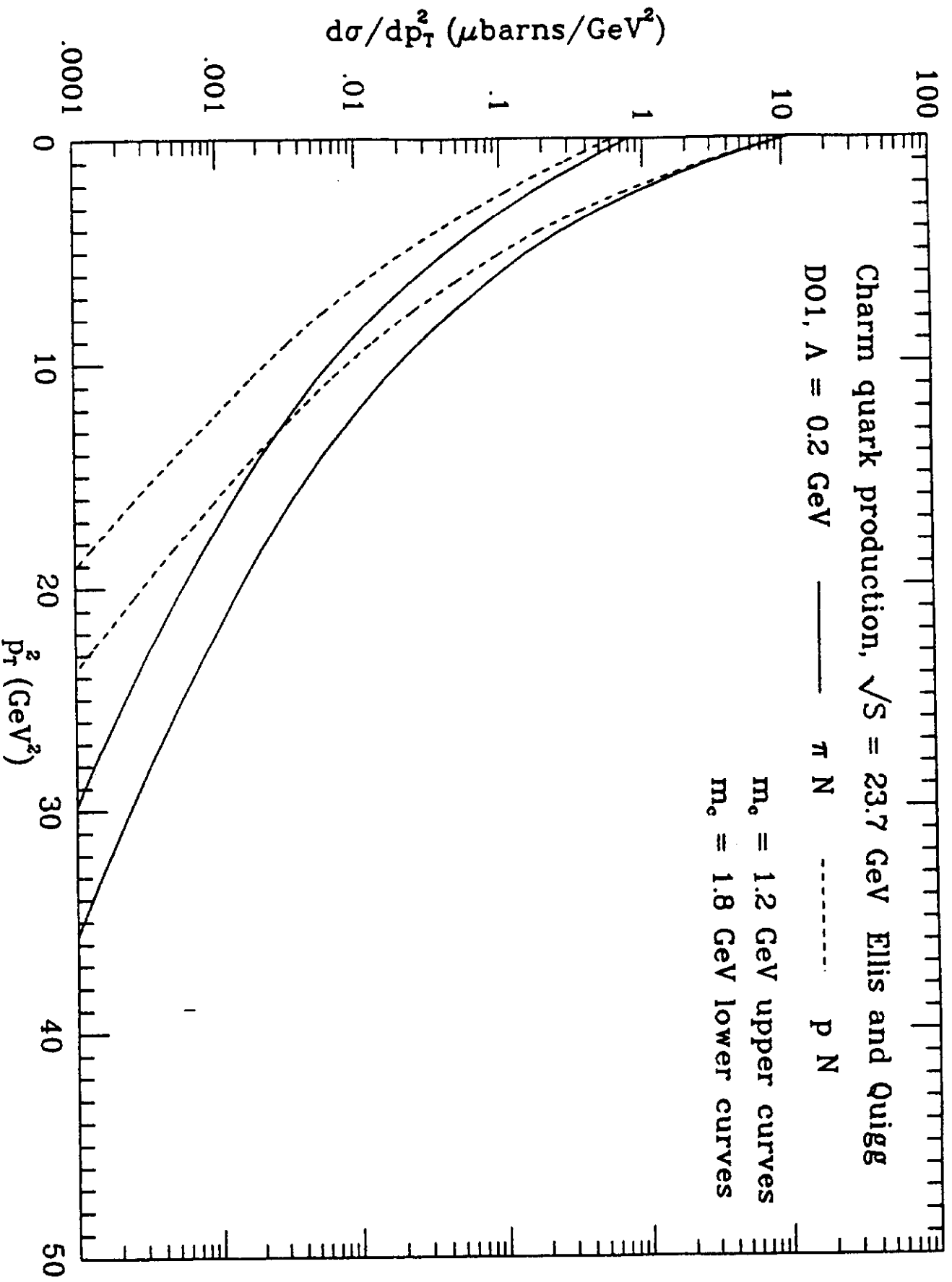


Figure 10: Differential cross section $d\sigma/dp_T^2$ for the production of charmed quarks in πN (solid lines) and pN (dashed lines) collisions at $\sqrt{s} = 23.7$ GeV ($p_{beam} = 300$ GeV/c).

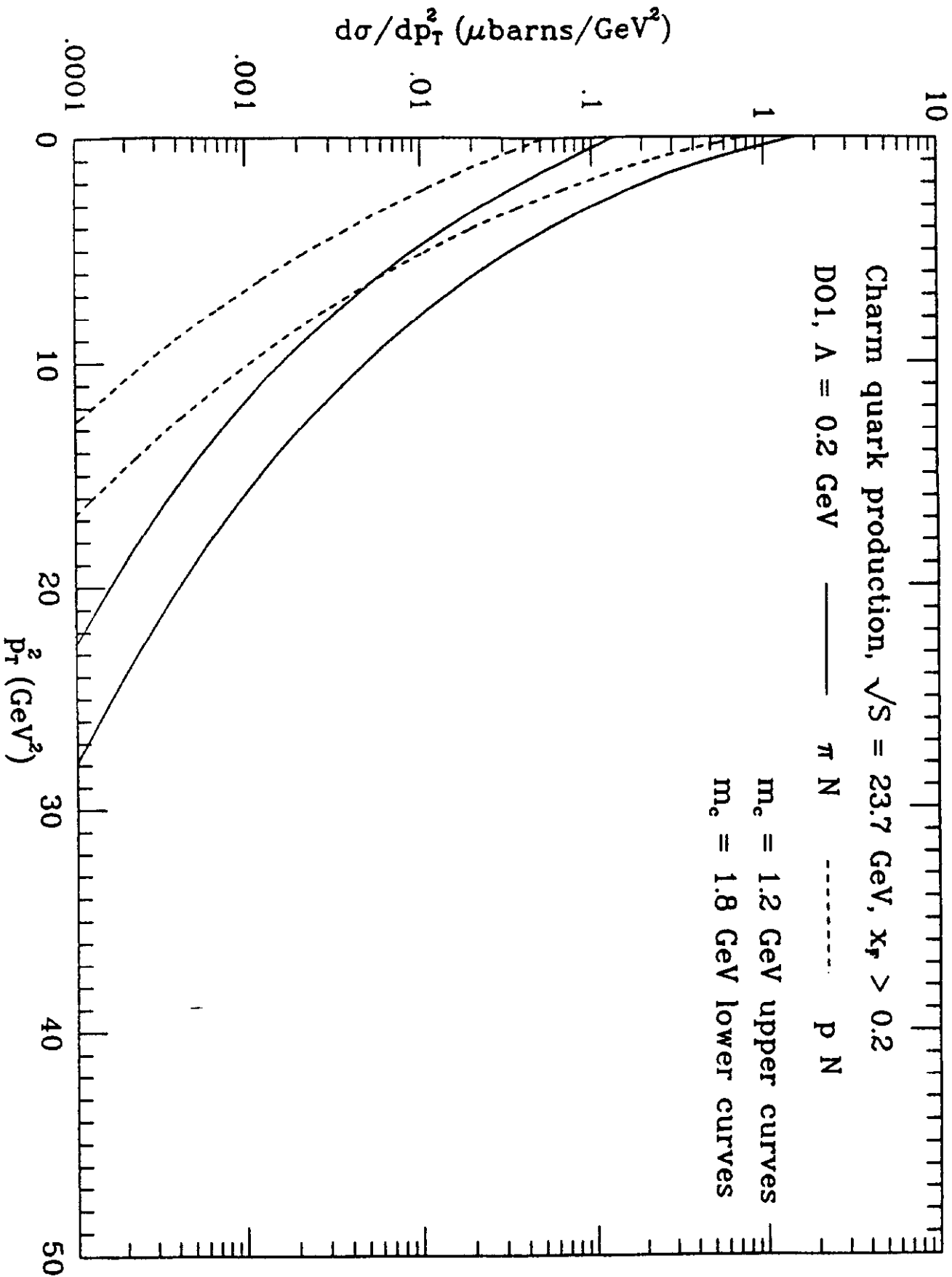


Figure 11: Differential cross section $d\sigma/dp_T^2$ for the forward production ($x_F > 0.2$) of charmed quarks in πN (solid lines) and pN (dashed lines) collisions at $\sqrt{s} = 23.7$ GeV ($p_{beam} = 300$ GeV/c).

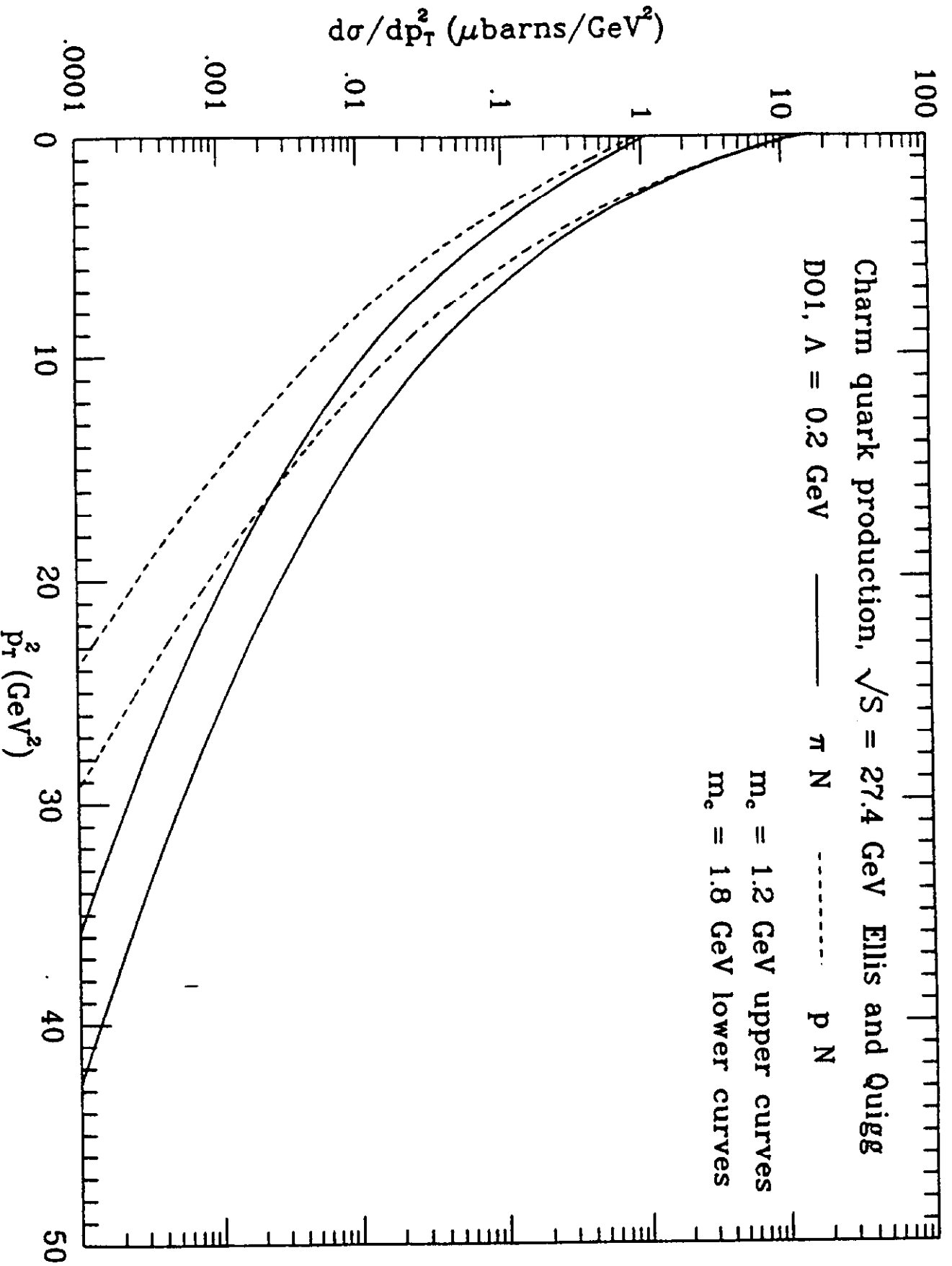


Figure 12: Differential cross section $d\sigma/dp_T^2$ for the production of charmed quarks in πN (solid lines) and $p N$ (dashed lines) collisions at $\sqrt{s} = 27.4$ GeV ($p_{beam} = 400$ GeV/c).

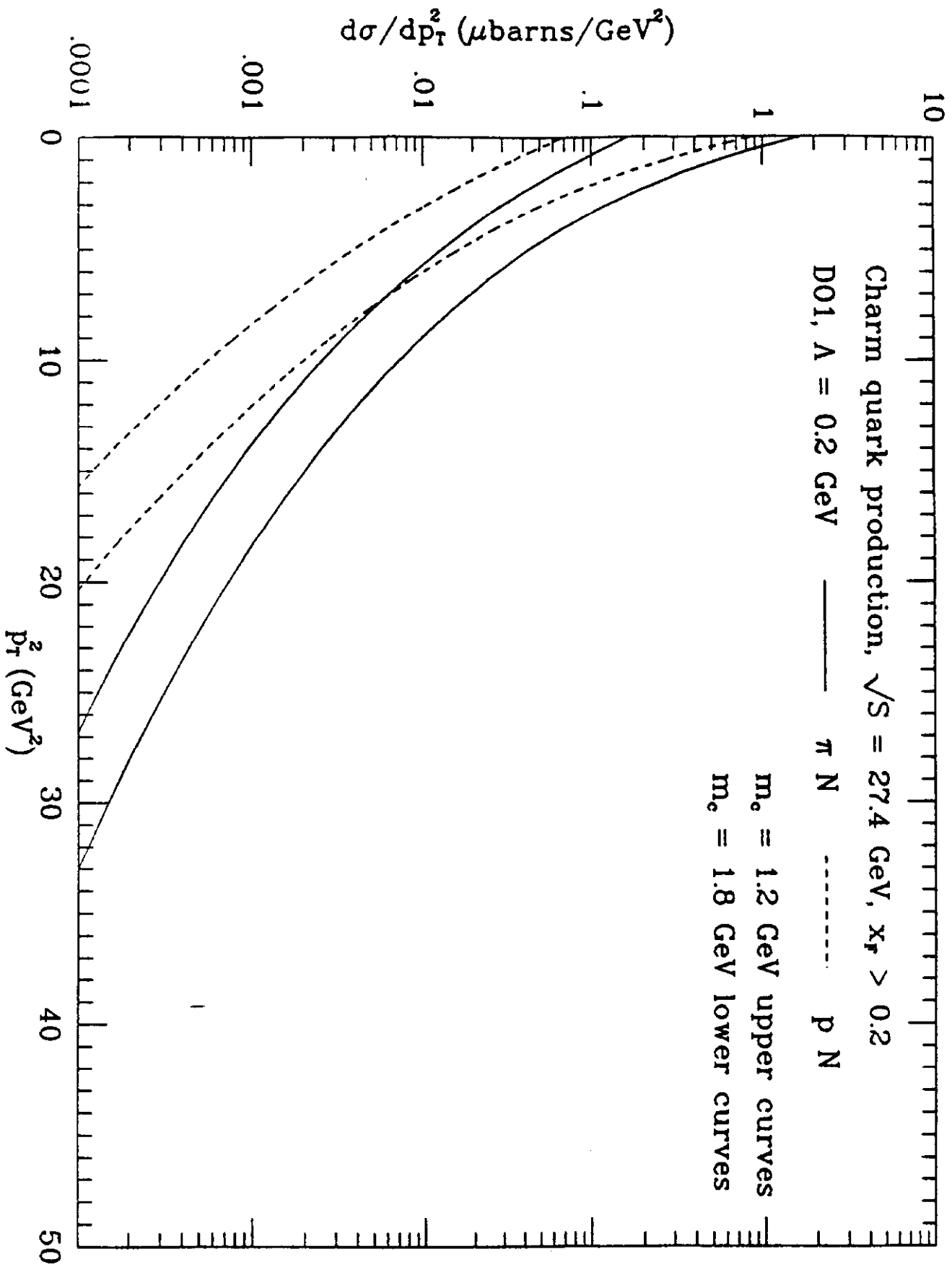


Figure 13: Differential cross section $d\sigma/dp_T^2$ for the forward production ($x_F > 0.2$) of charmed quarks in πN (solid lines) and pN (dashed lines) collisions at $\sqrt{s} = 27.4 \text{ GeV}$ ($p_{beam} = 400 \text{ GeV}/c$).

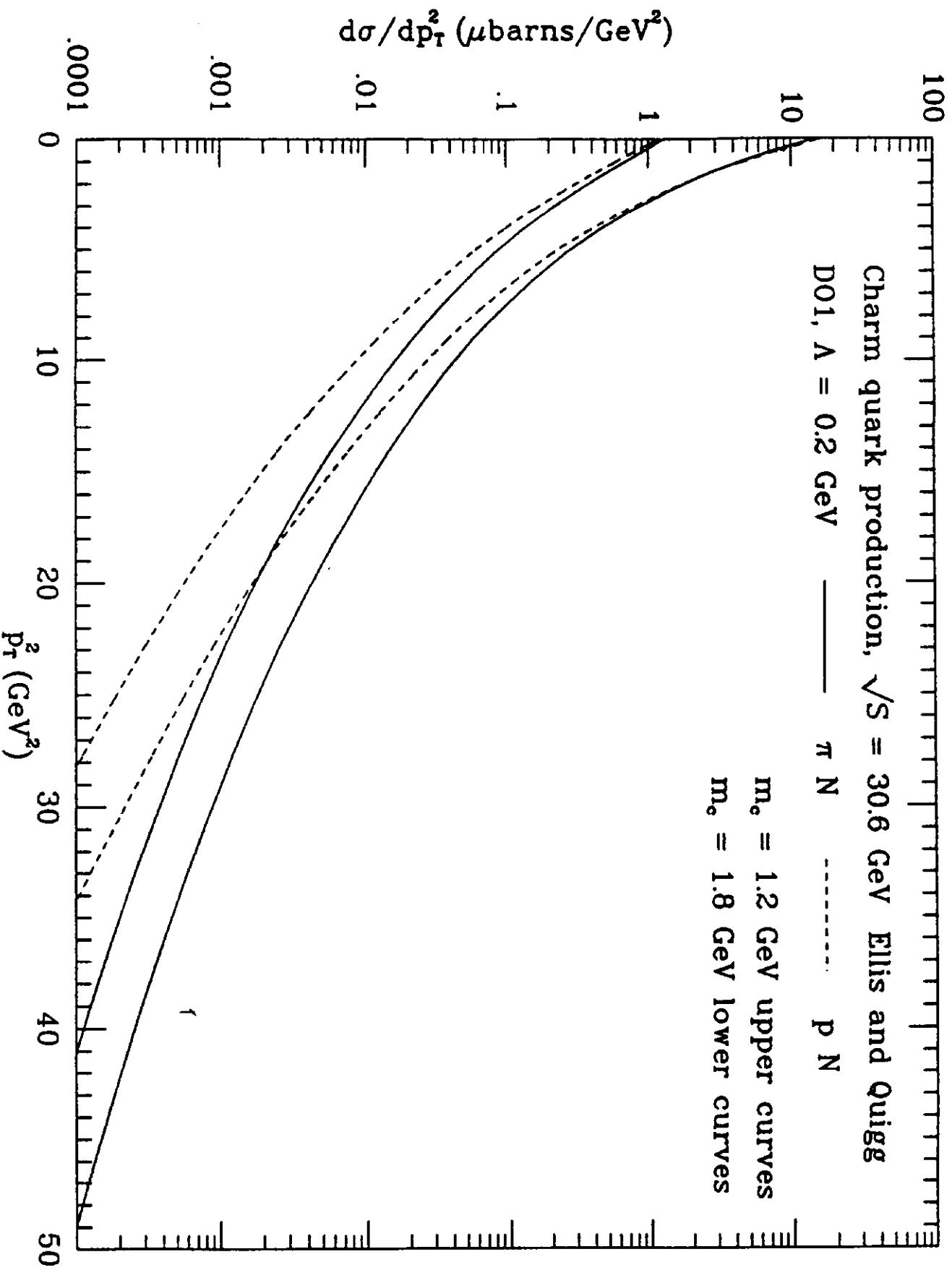


Figure 14: Differential cross section $d\sigma/dp_T^2$ for the production of charmed quarks in πN (solid lines) and pN (dashed lines) collisions at $\sqrt{s} = 30.6$ GeV ($p_{beam} = 500$ GeV/c).

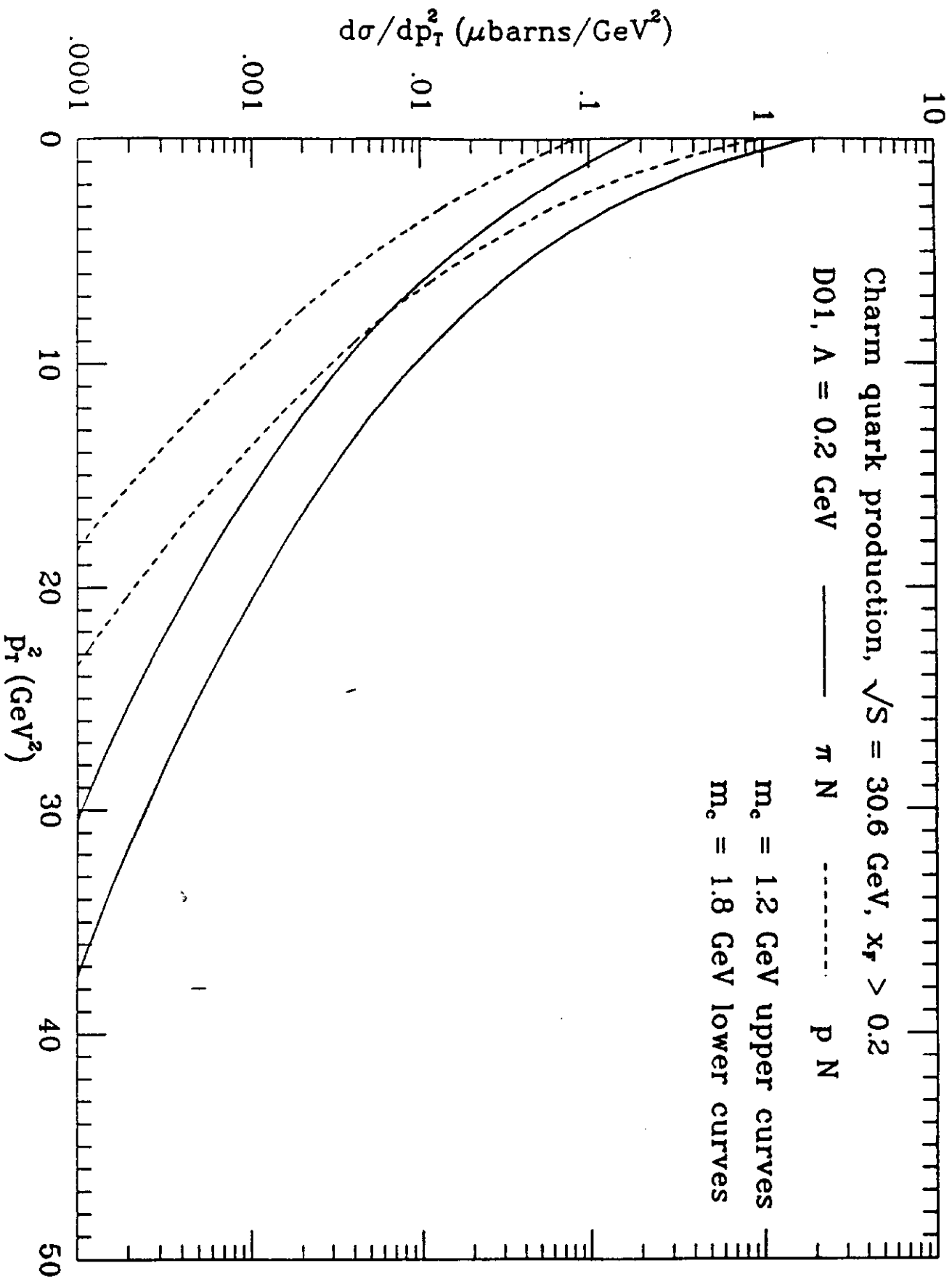


Figure 15: Differential cross section $d\sigma/dp_T^2$ for the forward production ($x_F > 0.2$) of charmed quarks in πN (solid lines) and pN (dashed lines) collisions at $\sqrt{s} = 30.6 \text{ GeV}$ ($p_{beam} = 500 \text{ GeV}/c$).

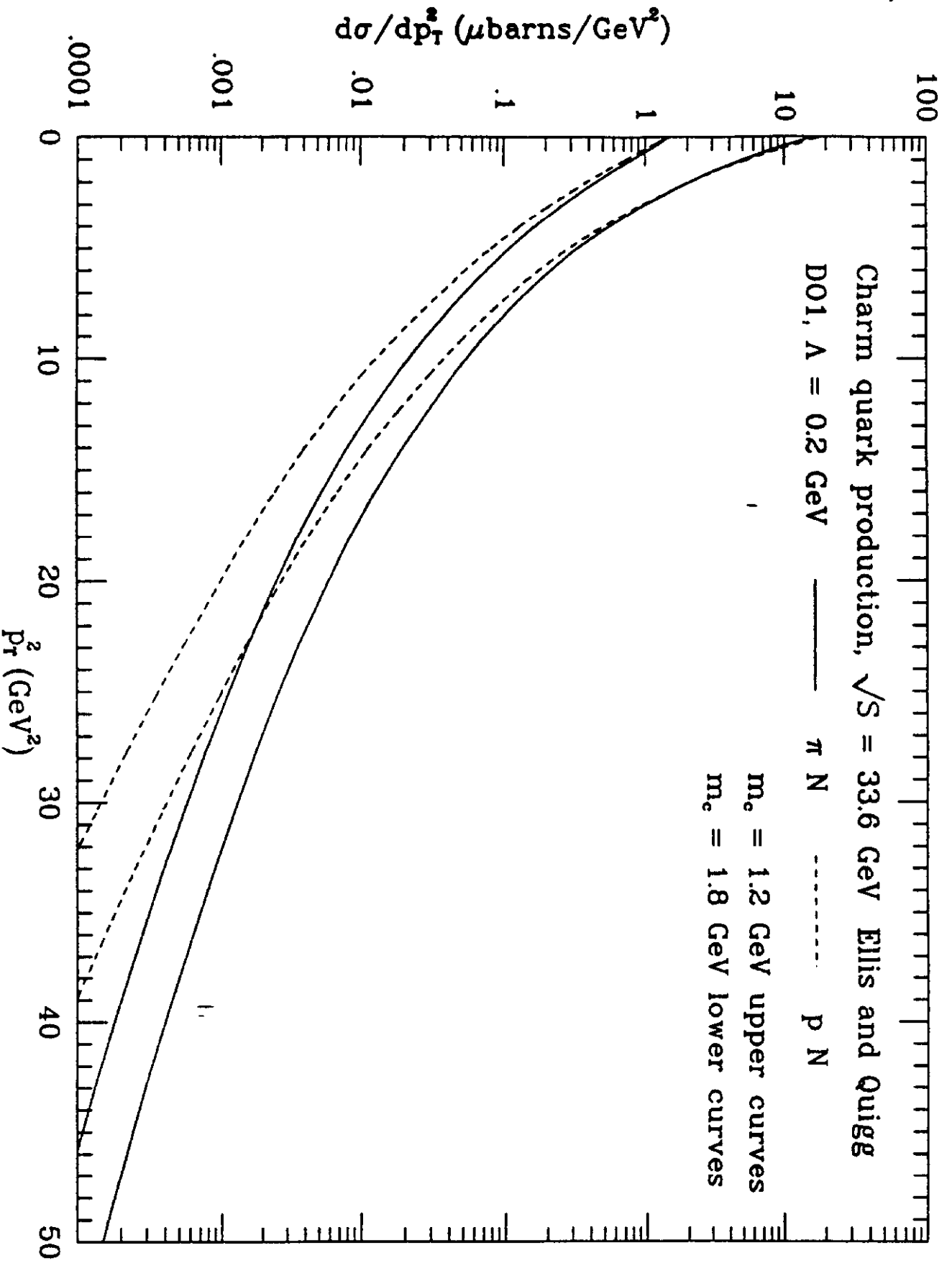


Figure 16: Differential cross section $d\sigma/dp_T^2$ for the production of charmed quarks in πN (solid lines) and pN (dashed lines) collisions at $\sqrt{s} = 33.6$ GeV ($p_{beam} = 600$ GeV/c).

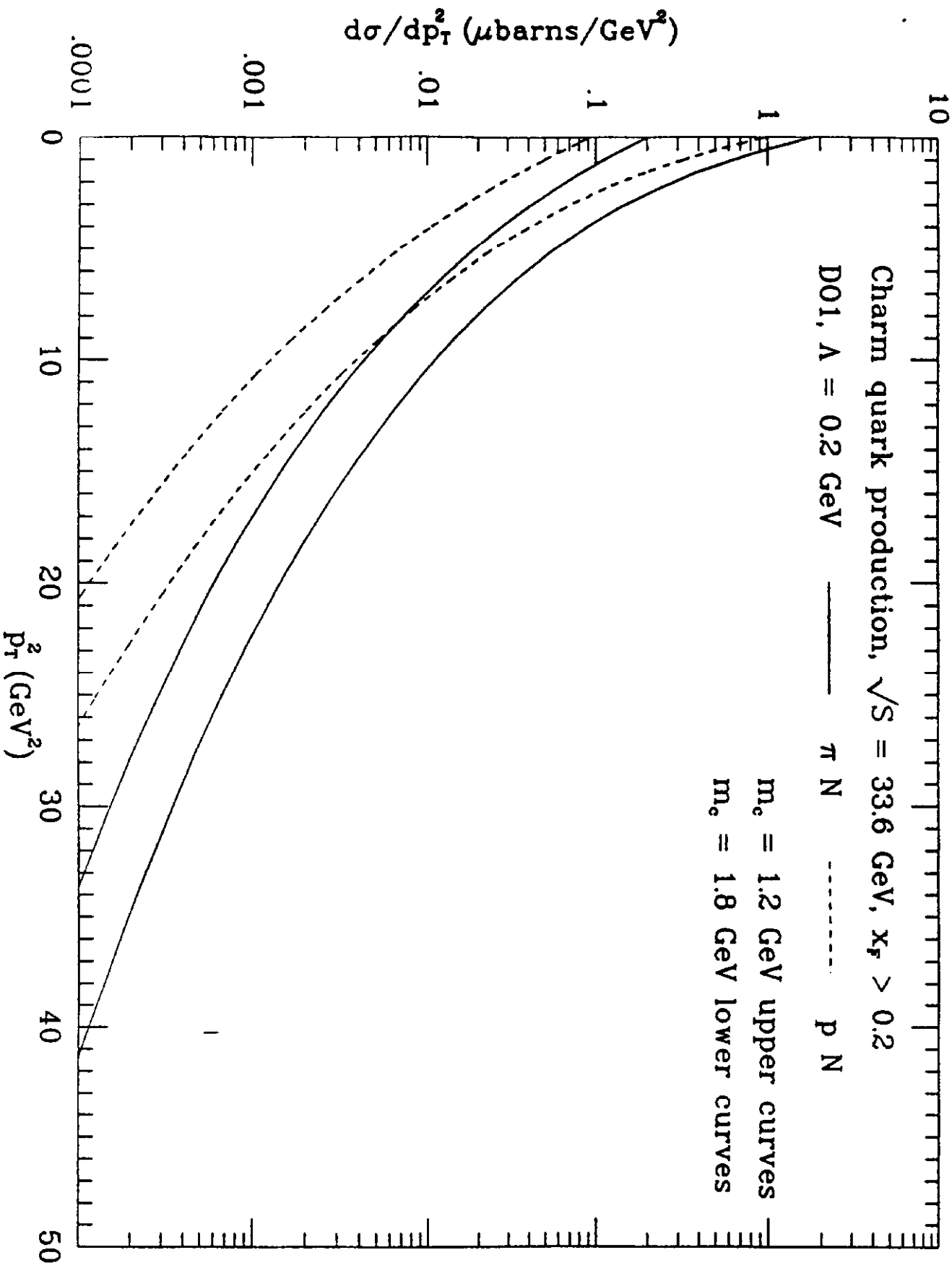


Figure 17: Differential cross section $d\sigma/dp_T^2$ for the forward production ($x_F > 0.2$) of charmed quarks in πN (solid lines) and pN (dashed lines) collisions at $\sqrt{s} = 33.6$ GeV ($p_{beam} = 600$ GeV/c).

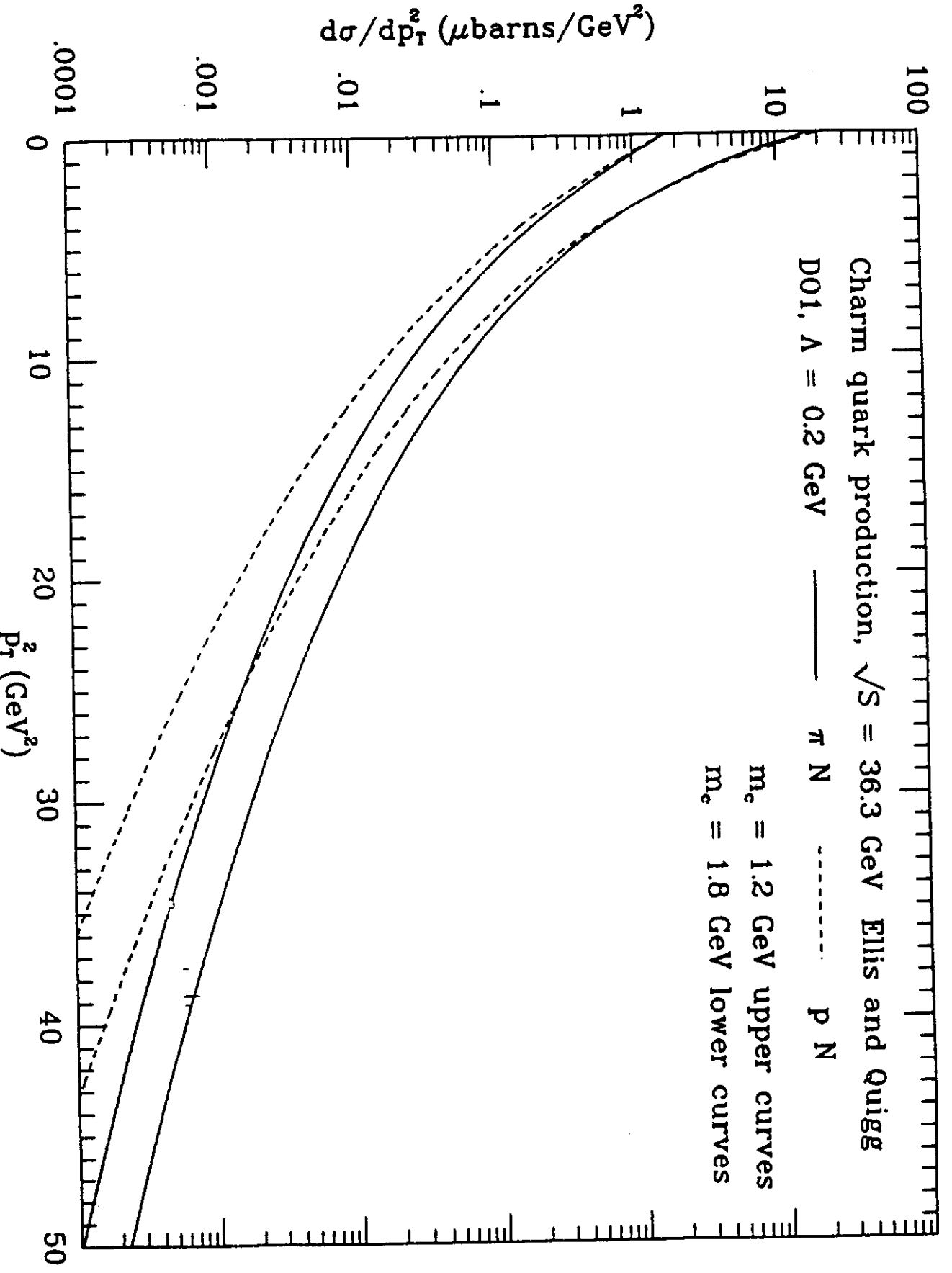


Figure 18: Differential cross section $d\sigma/dp_T^2$ for the production of charmed quarks in πN (solid lines) and pN (dashed lines) collisions at $\sqrt{s} = 36.3$ GeV ($p_{\text{beam}} = 700$ GeV/c).

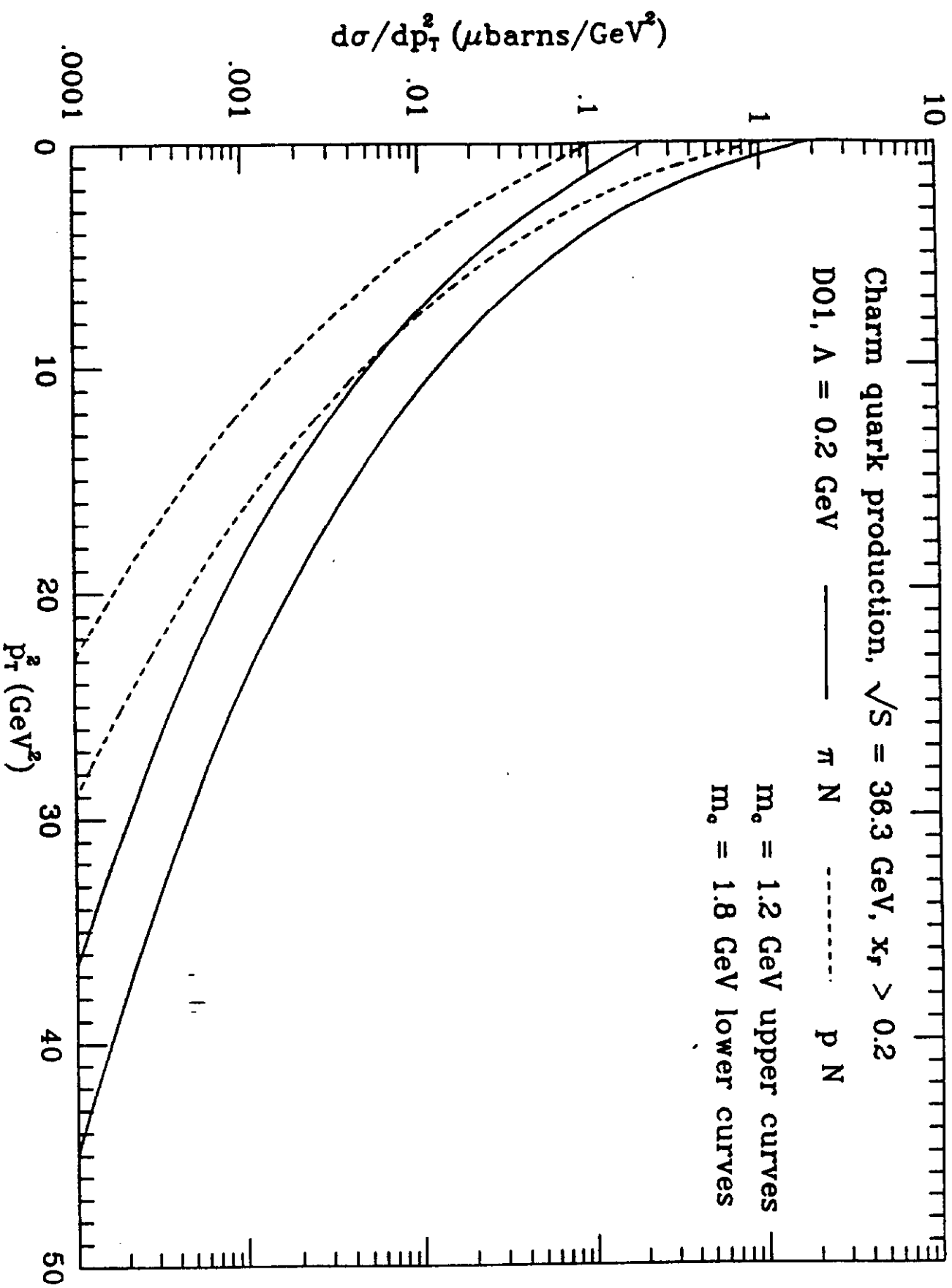


Figure 19: Differential cross section $d\sigma/dp_T^2$ for the forward production ($x_f > 0.2$) of charmed quarks in πN (solid lines) and pN (dashed lines) collisions at $\sqrt{s} = 36.3 \text{ GeV}$ ($p_{beam} = 700 \text{ GeV}/c$).

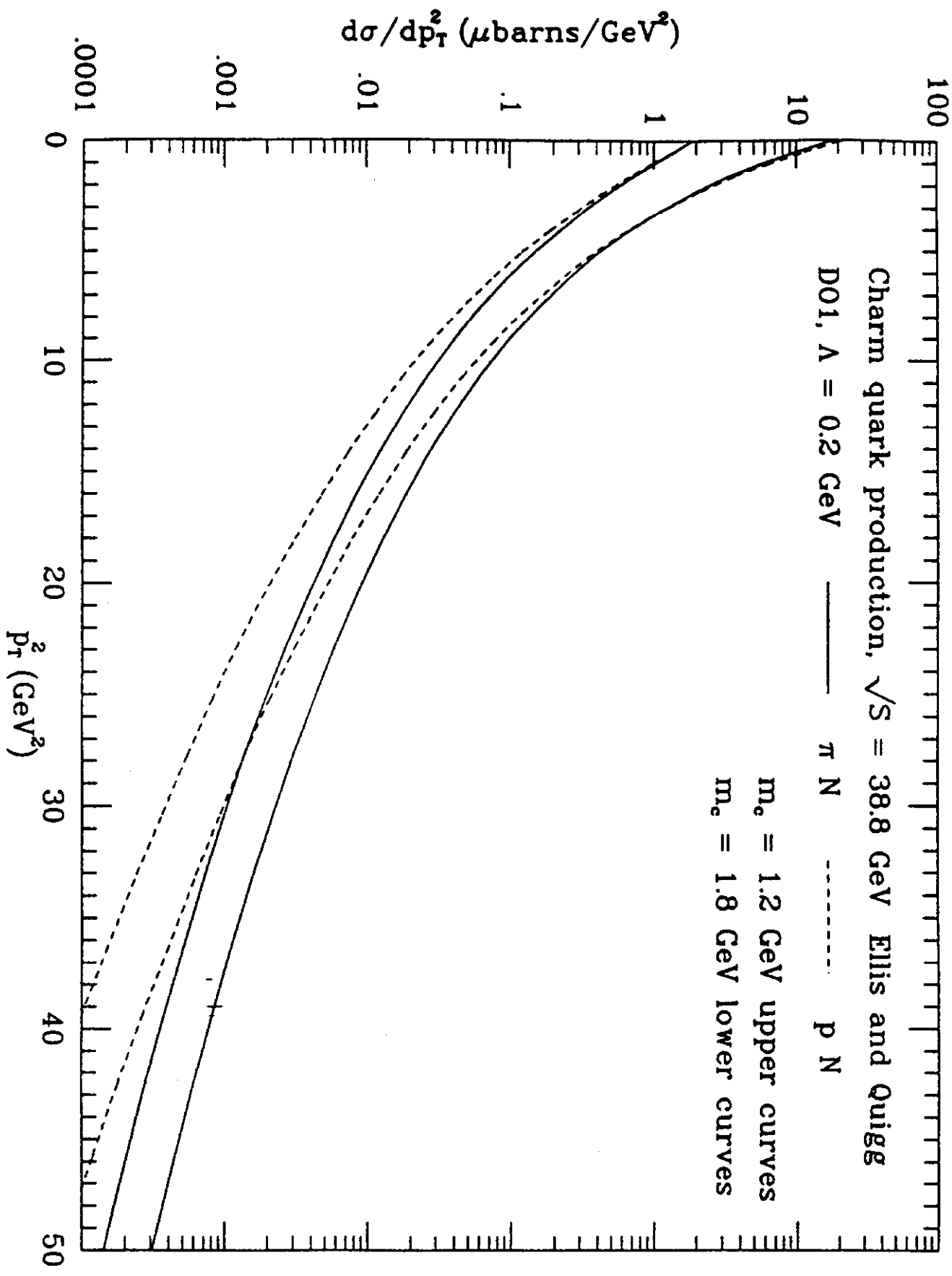


Figure 20: Differential cross section $d\sigma/dp_T^2$ for the production of charmed quarks in πN (solid lines) and pN (dashed lines) collisions at $\sqrt{s} = 38.8$ GeV ($p_{beam} = 800$ GeV/c).

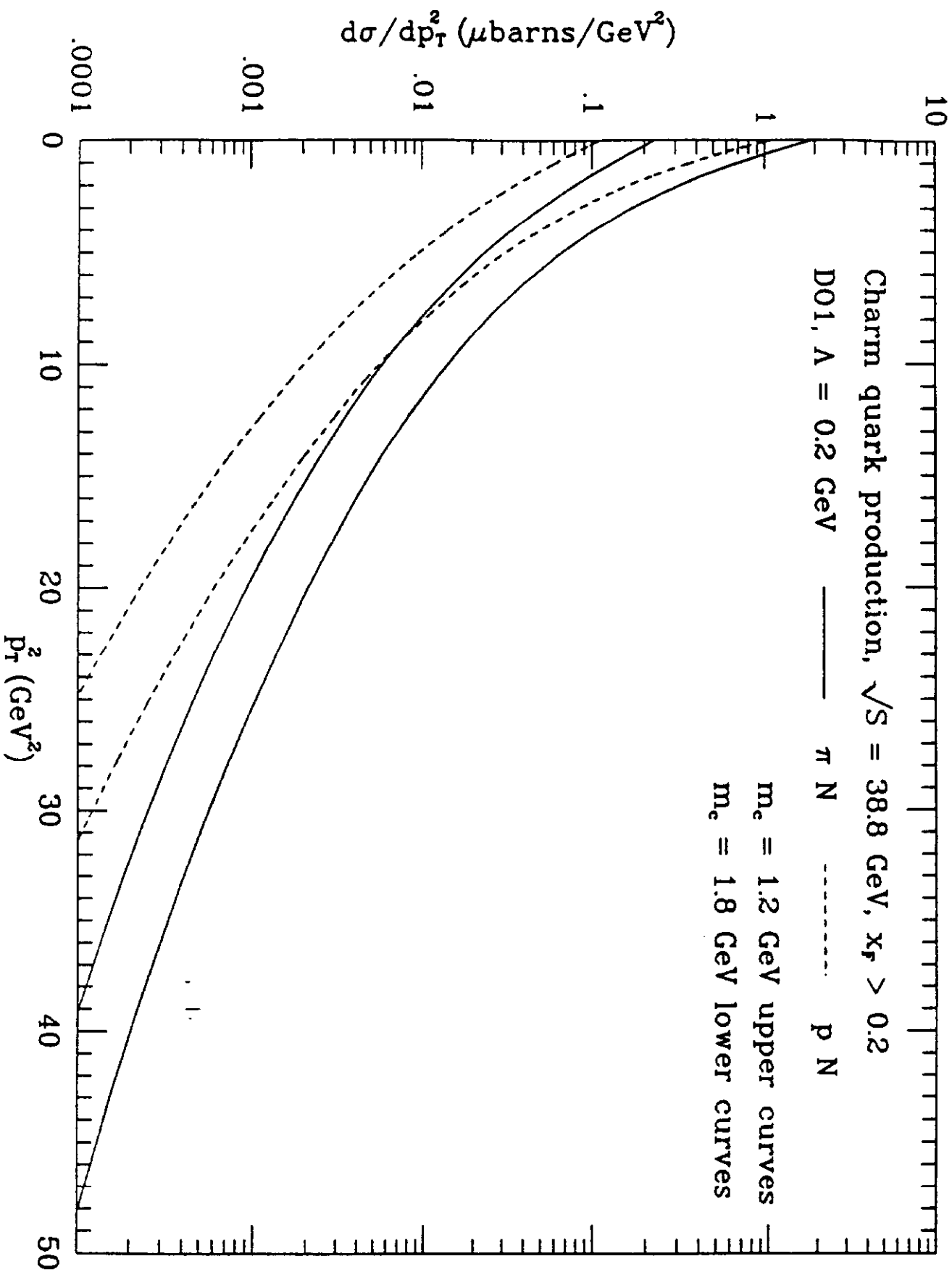


Figure 21: Differential cross section $d\sigma/dp_T^2$ for the forward production ($x_F > 0.2$) of charmed quarks in πN (solid lines) and pN (dashed lines) collisions at $\sqrt{s} = 38.8 \text{ GeV}$ ($p_{beam} = 800 \text{ GeV}/c$).

$pN \rightarrow cc + \text{anything}$

$$P_p = 600 \text{ GeV}/c$$

$$m_c = 1.5 \text{ GeV}/c^2$$

Ellis and Quigg

D01

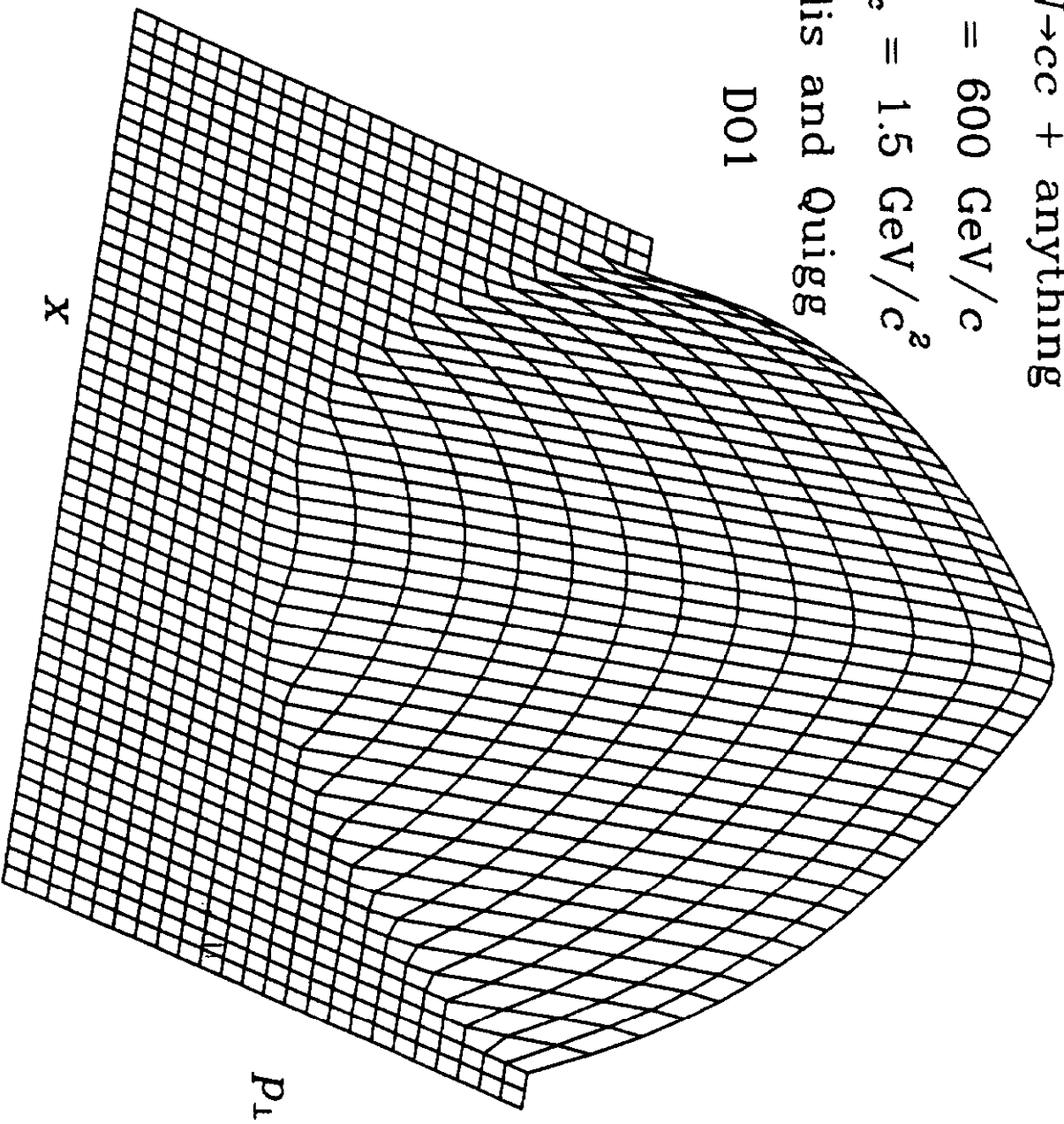


Figure 22: Three-dimensional representation of $\log E d\sigma/d^3p$ for the production of charmed quarks with $m_c = 1.5 \text{ GeV}/c^2$ in $600 \text{ GeV}/c$ pN collisions.

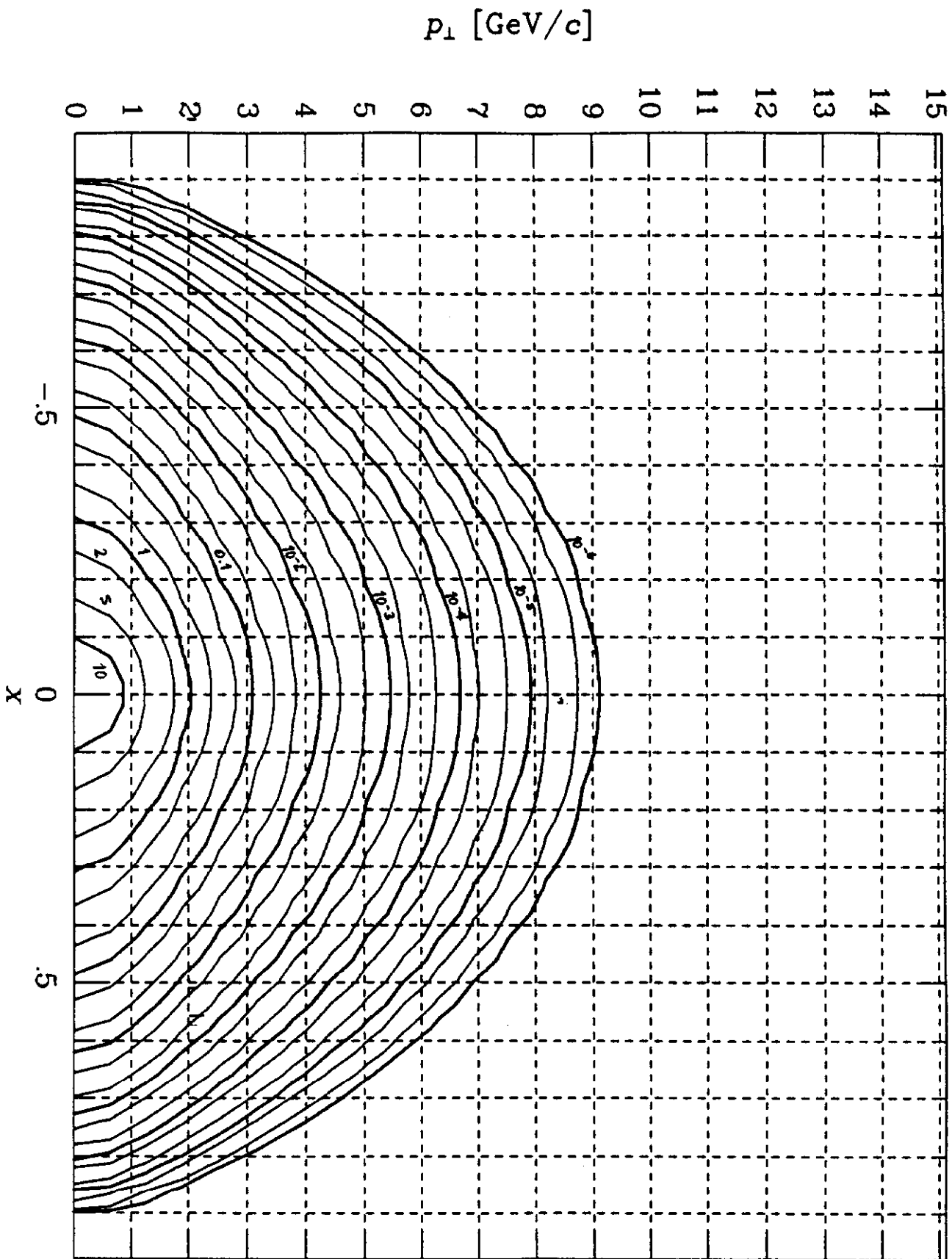


Figure 23: Contour plot of $E ds/d^3p$ for the production of charmed quarks with $m_c = 1.5 \text{ GeV}/c^2$ in $800 \text{ GeV}/c$ pN collisions.

$\pi N \rightarrow cc + \text{anything}$

$$p_\pi = 600 \text{ GeV}/c$$

$$m_c = 1.5 \text{ GeV}/c^2$$

Ellis and Quigg

D01

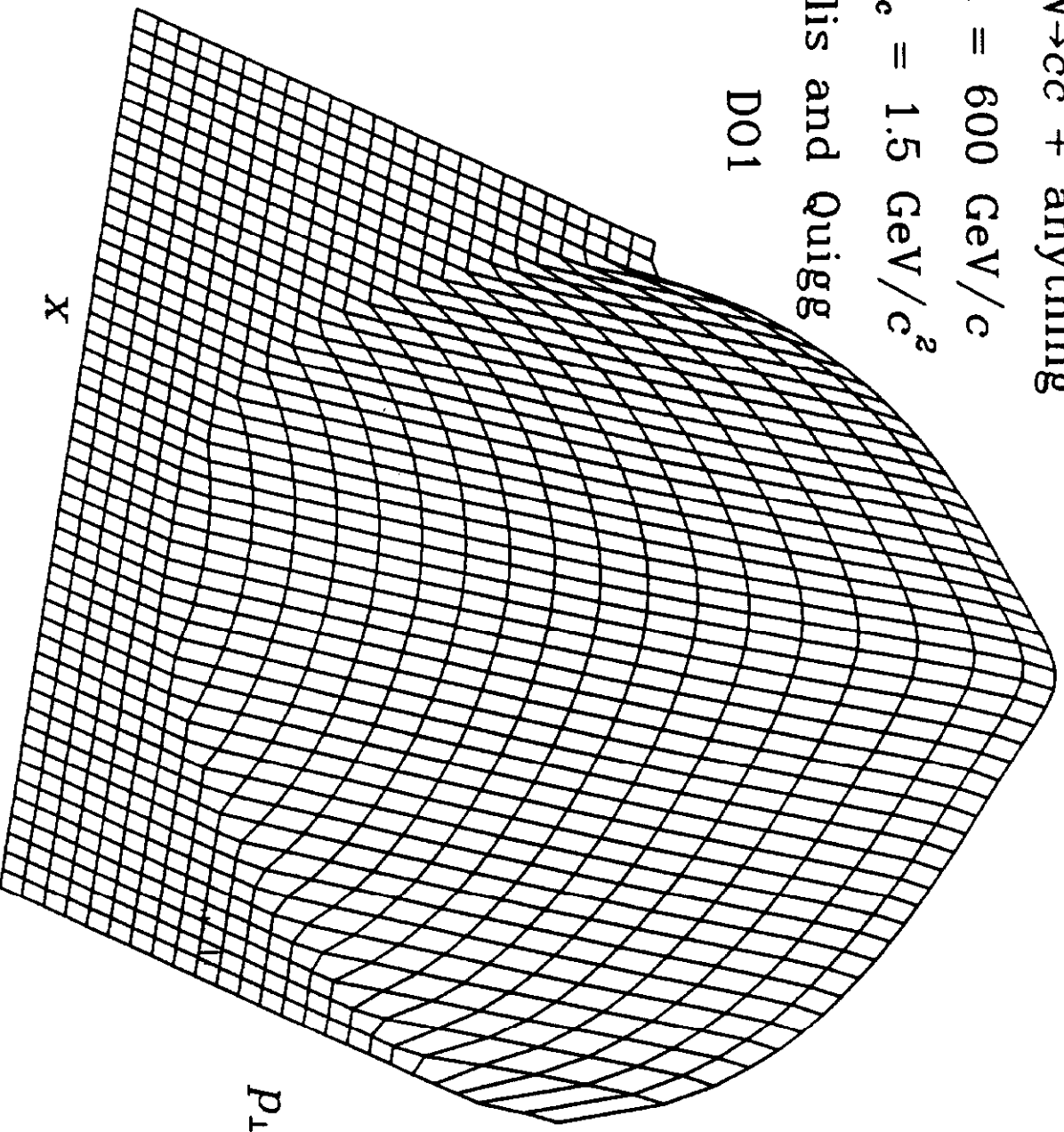


Figure 24: Three-dimensional representation of $\log E d\sigma/d^3p$ for the production of charmed quarks with $m_c = 1.5 \text{ GeV}/c^2$ in $600 \text{ GeV}/c$ πN collisions.

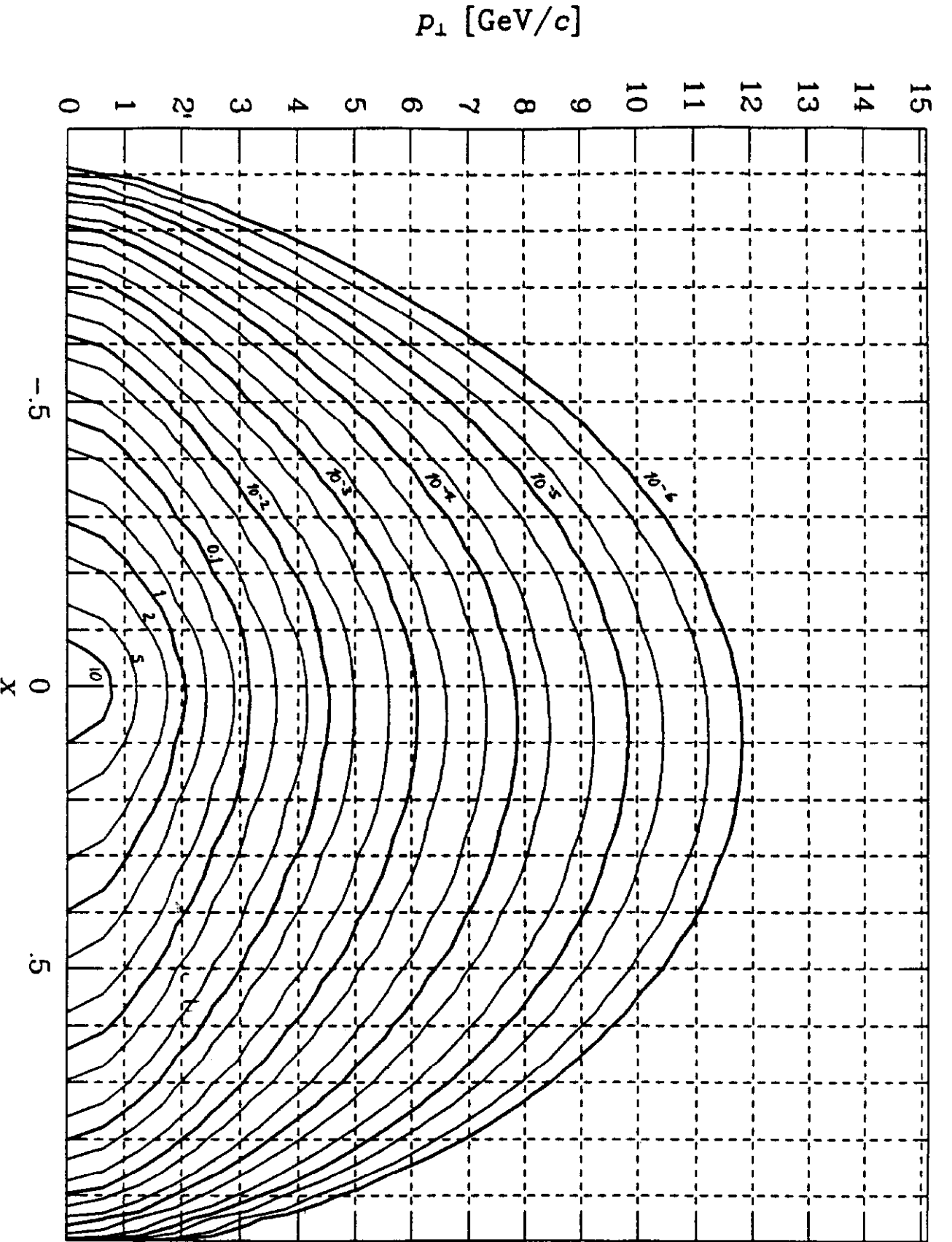


Figure 25: Contour plot of $E d\sigma/d^3p$ for the production of charmed quarks with $m_c = 1.5$ GeV/ c^2 in 800 GeV/ c πN collisions.

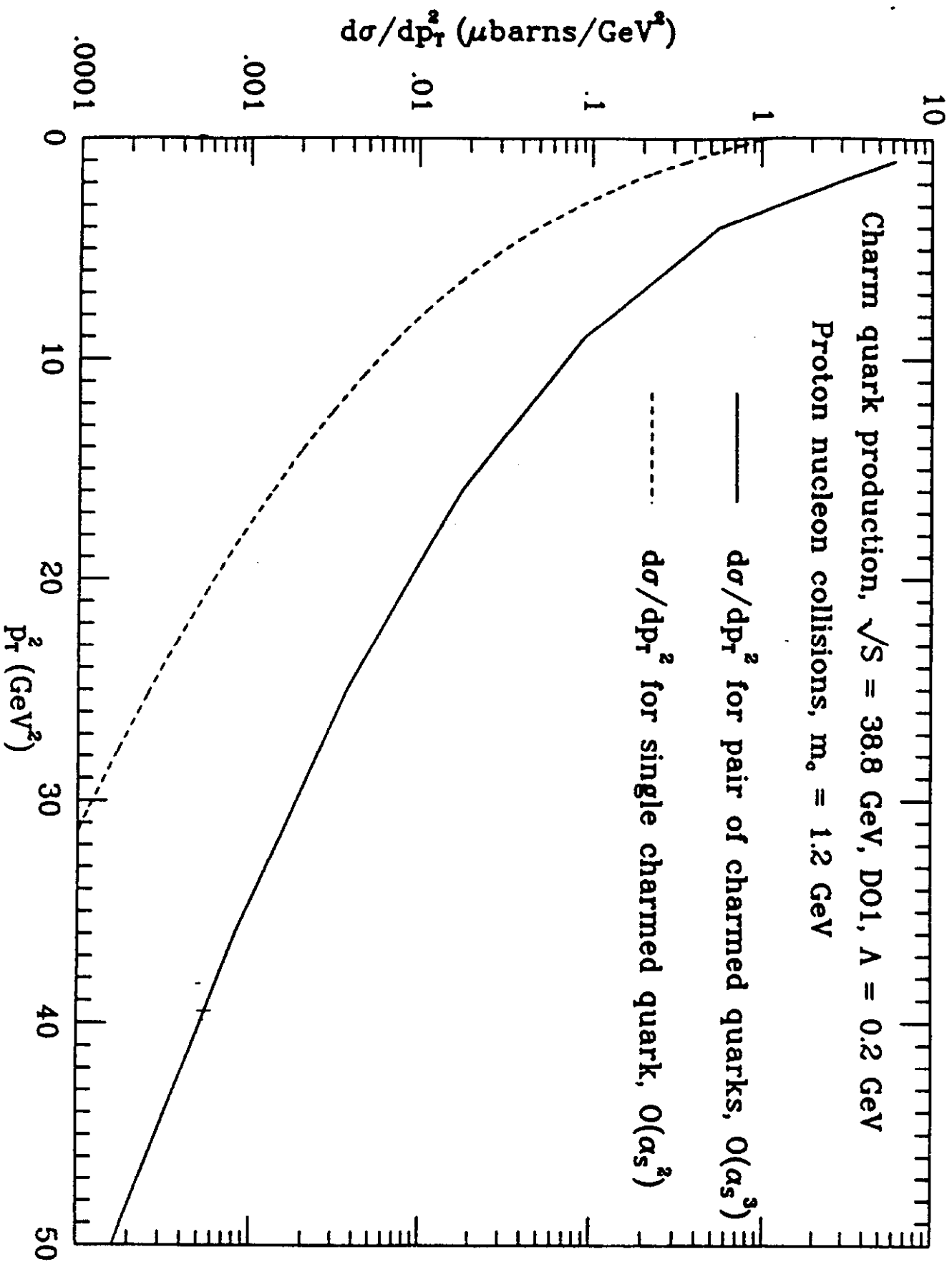


Figure 26: Relative importance of two-to-two and two-to-three processes.

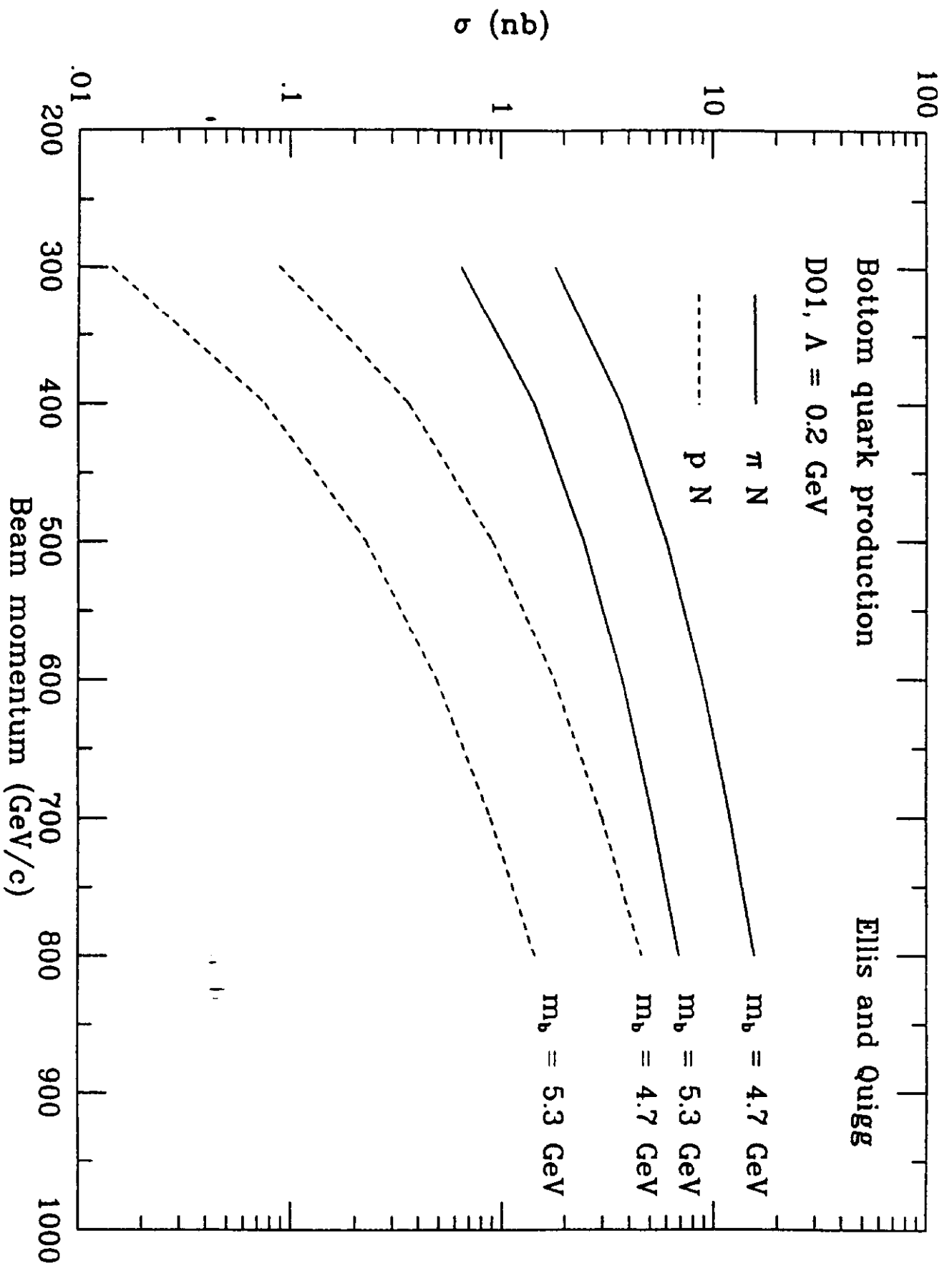


Figure 27: Integrated cross sections for the production of bottom quarks in πN (solid lines) and $p N$ (dashed lines) collisions.

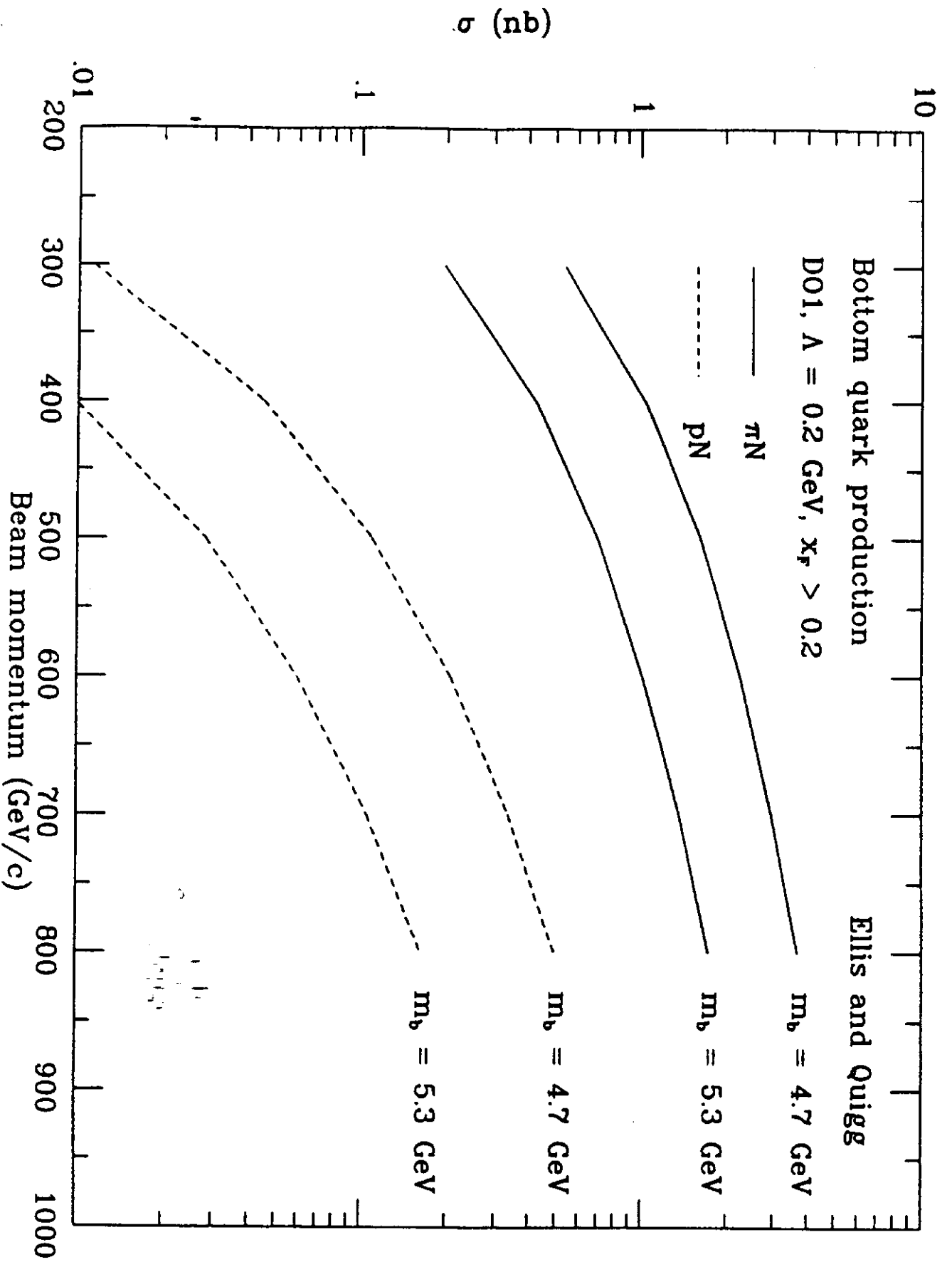


Figure 28: Integrated cross sections for the forward production ($x_F > 0.2$) of bottom quarks in πN (solid lines) and pN (dashed lines) collisions.

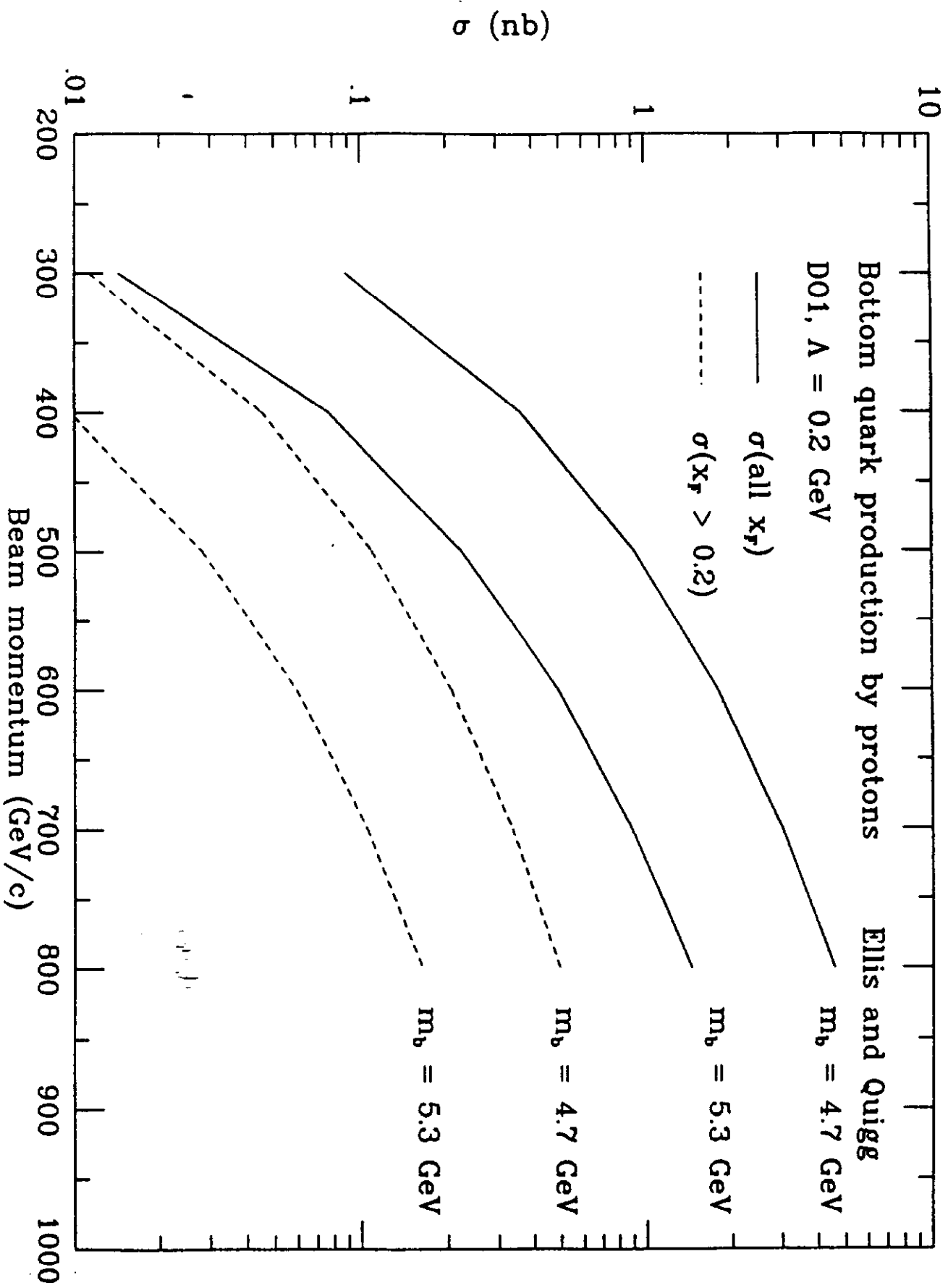


Figure 29: Integrated cross sections for the production of bottom quarks in pN collisions, for all x_F (solid lines), and restricted to $x_F > 0.2$ (dashed lines).

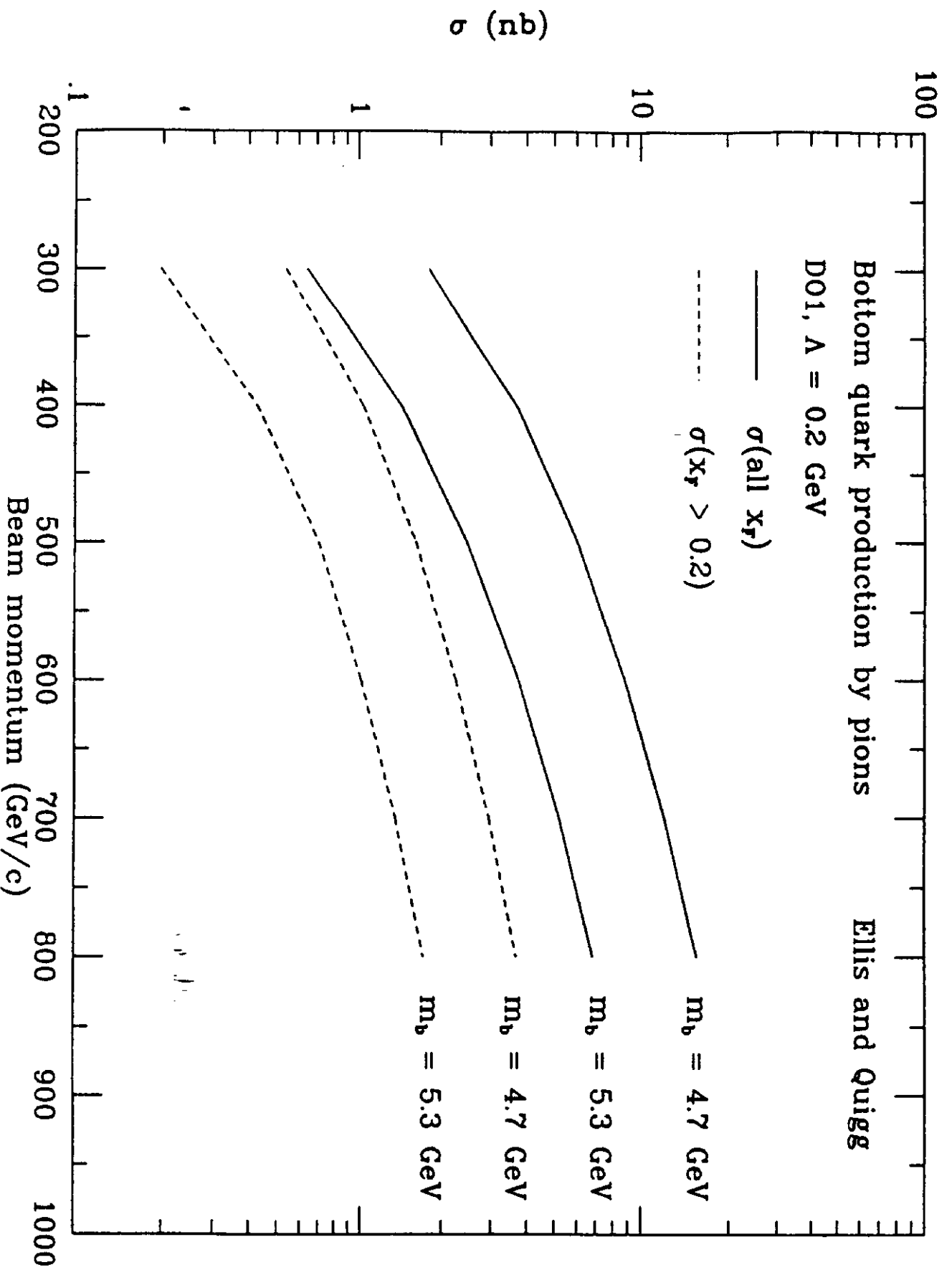


Figure 30: Integrated cross sections for the production of bottom quarks in πN collisions, for all x_F (solid lines), and restricted to $x_F > 0.2$ (dashed lines).

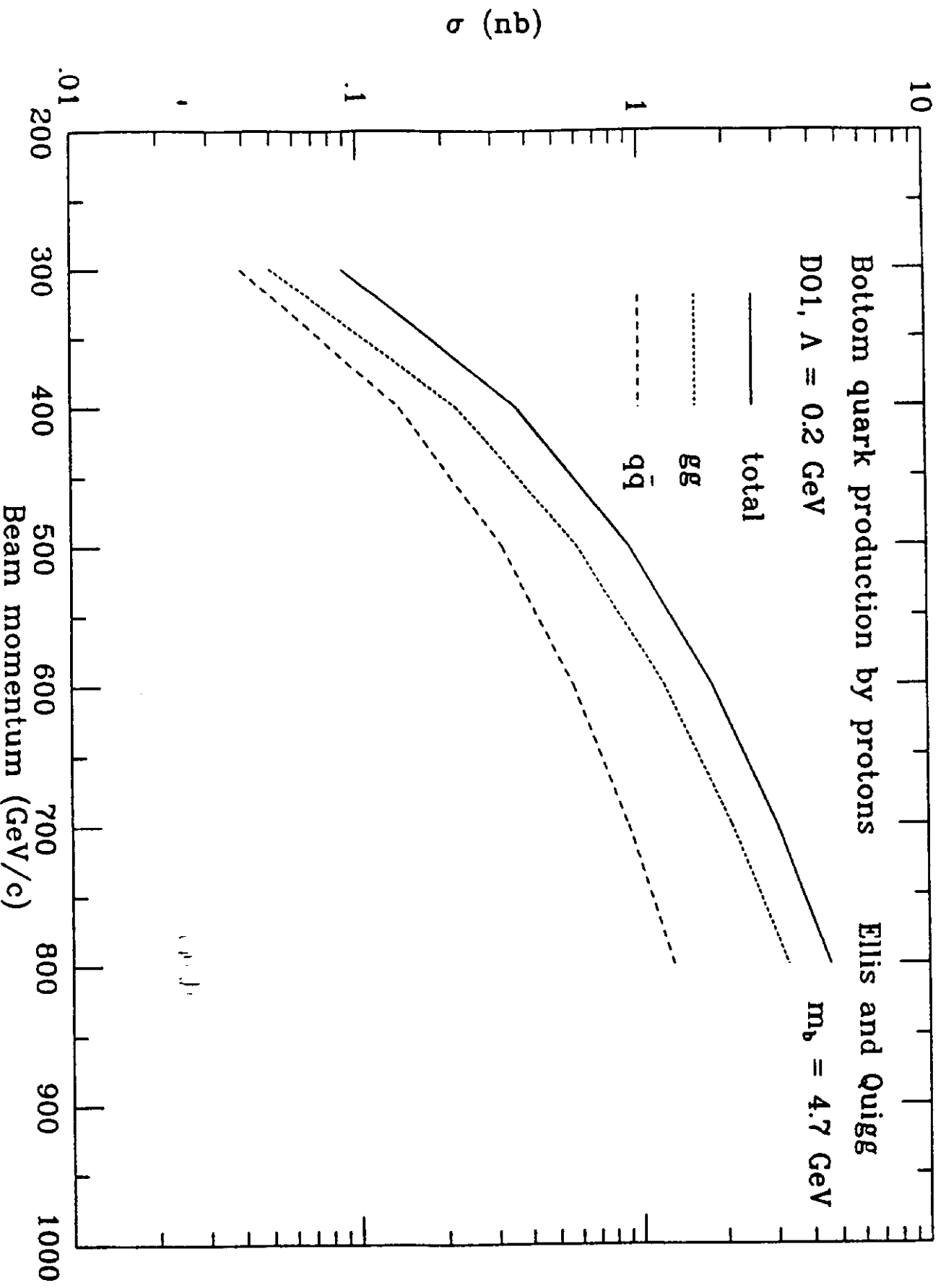


Figure 31: Contributions to the cross section for the production of bottom quarks in pN collisions, for $m_b = 4.7 \text{ GeV}/c^2$.

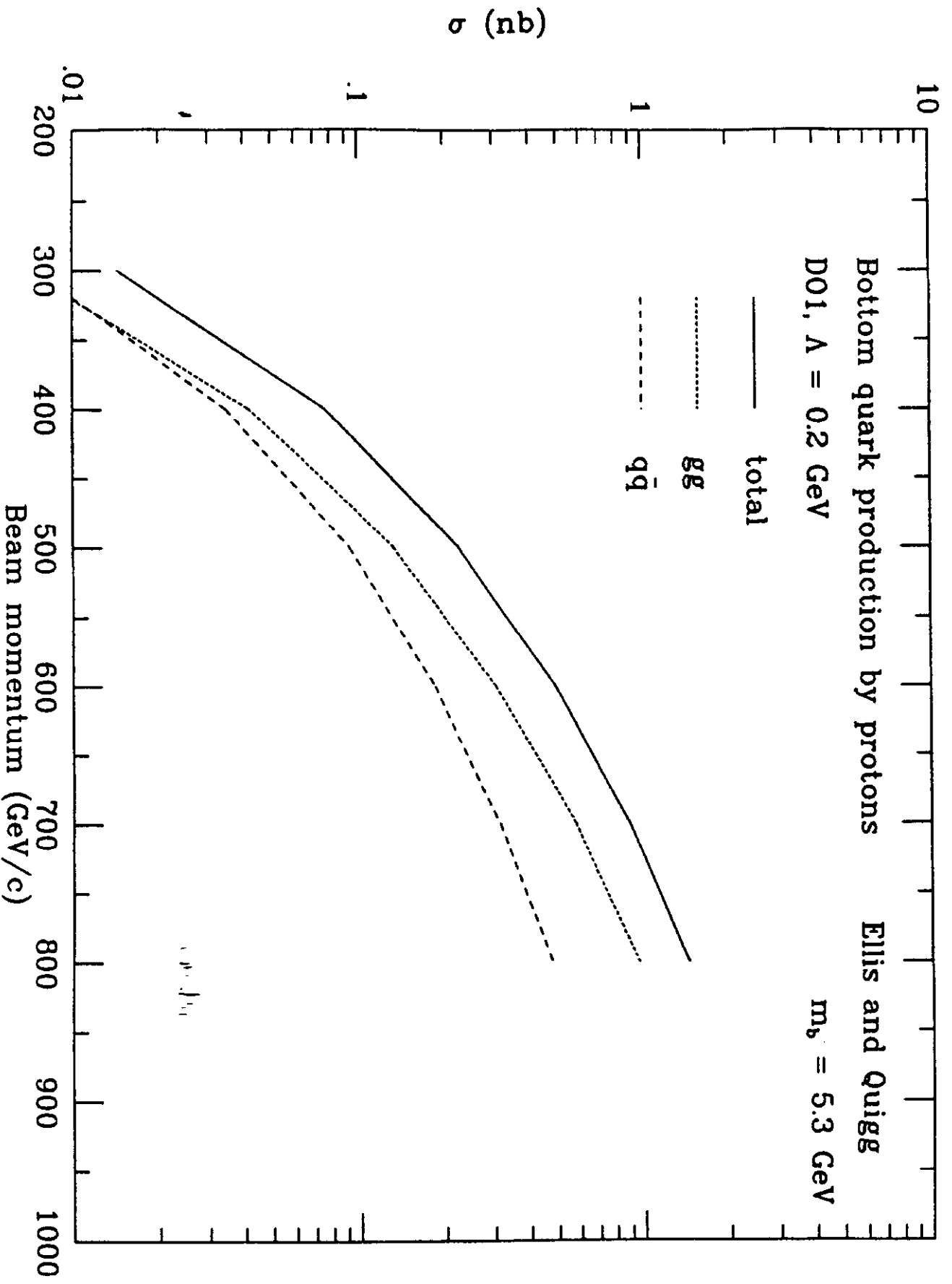


Figure 32: Contributions to the cross section for the production of bottom quarks in pN collisions, for $m_b = 5.3 \text{ GeV}/c^2$.

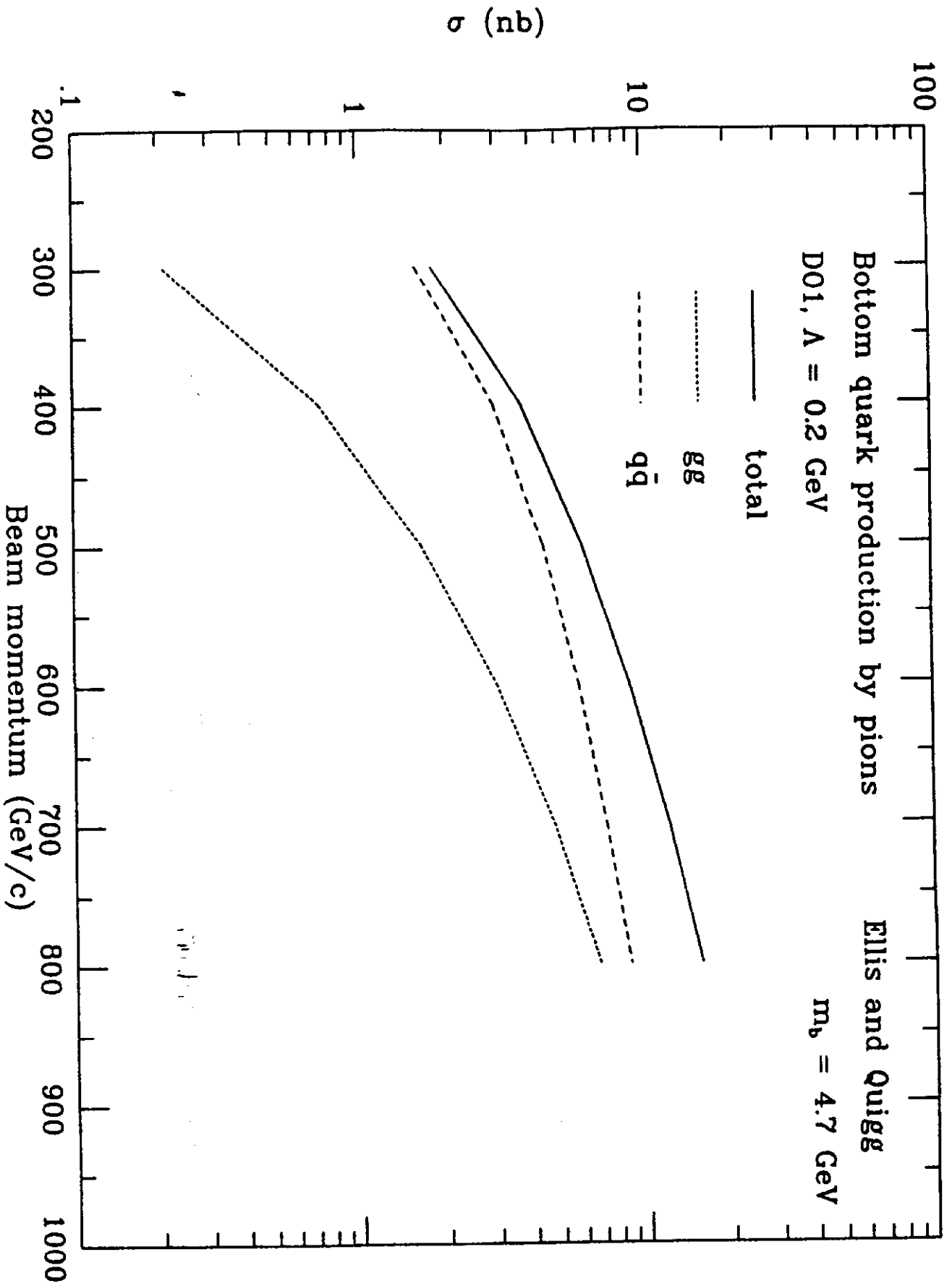


Figure 33: Contributions to the cross section for the production of bottom quarks in πN collisions, for $m_b = 4.7 \text{ GeV}/c^2$.

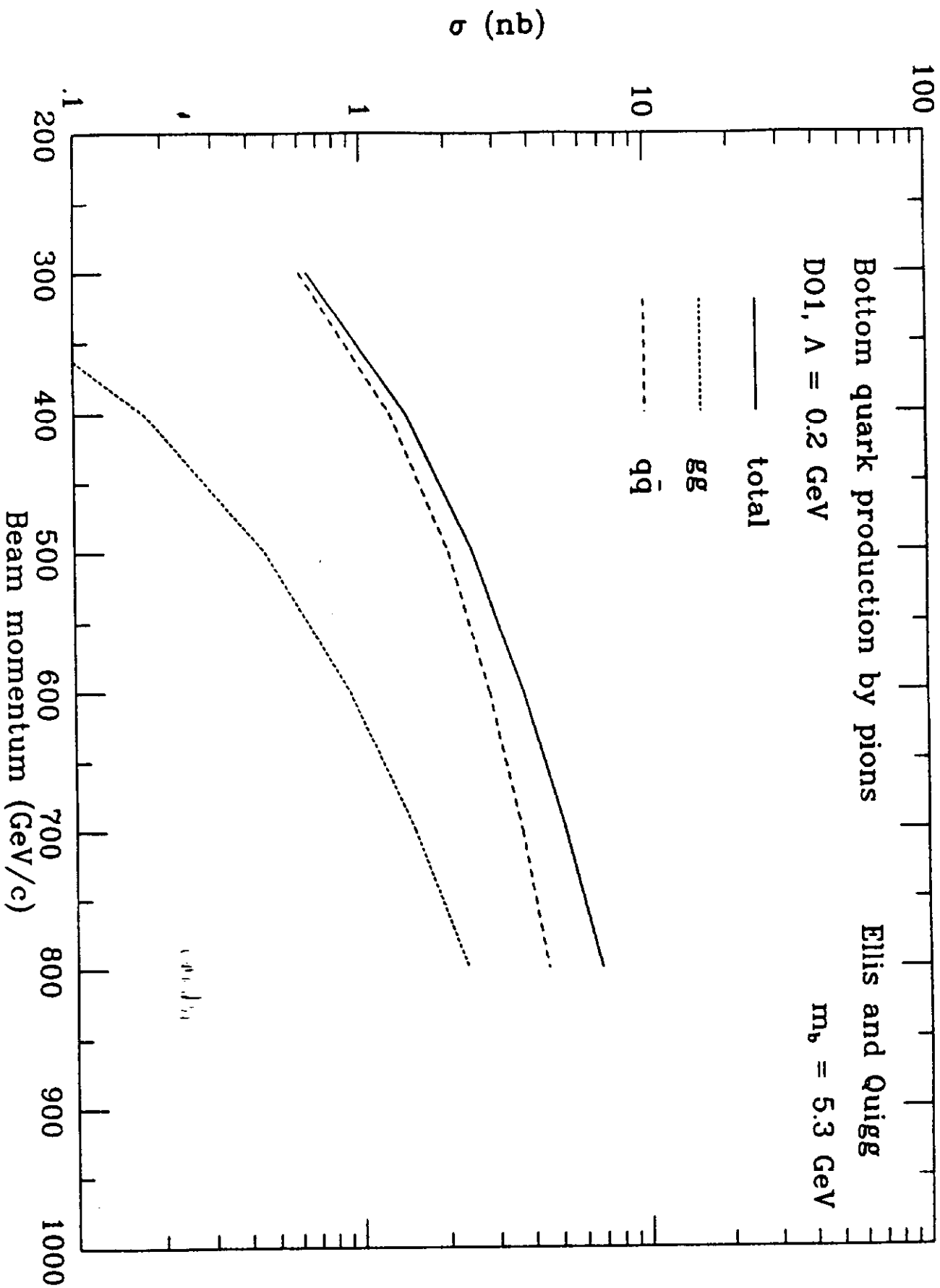


Figure 34: Contributions to the cross section for the production of bottom quarks in πN collisions, for $m_b = 5.3 \text{ GeV}/c^2$.

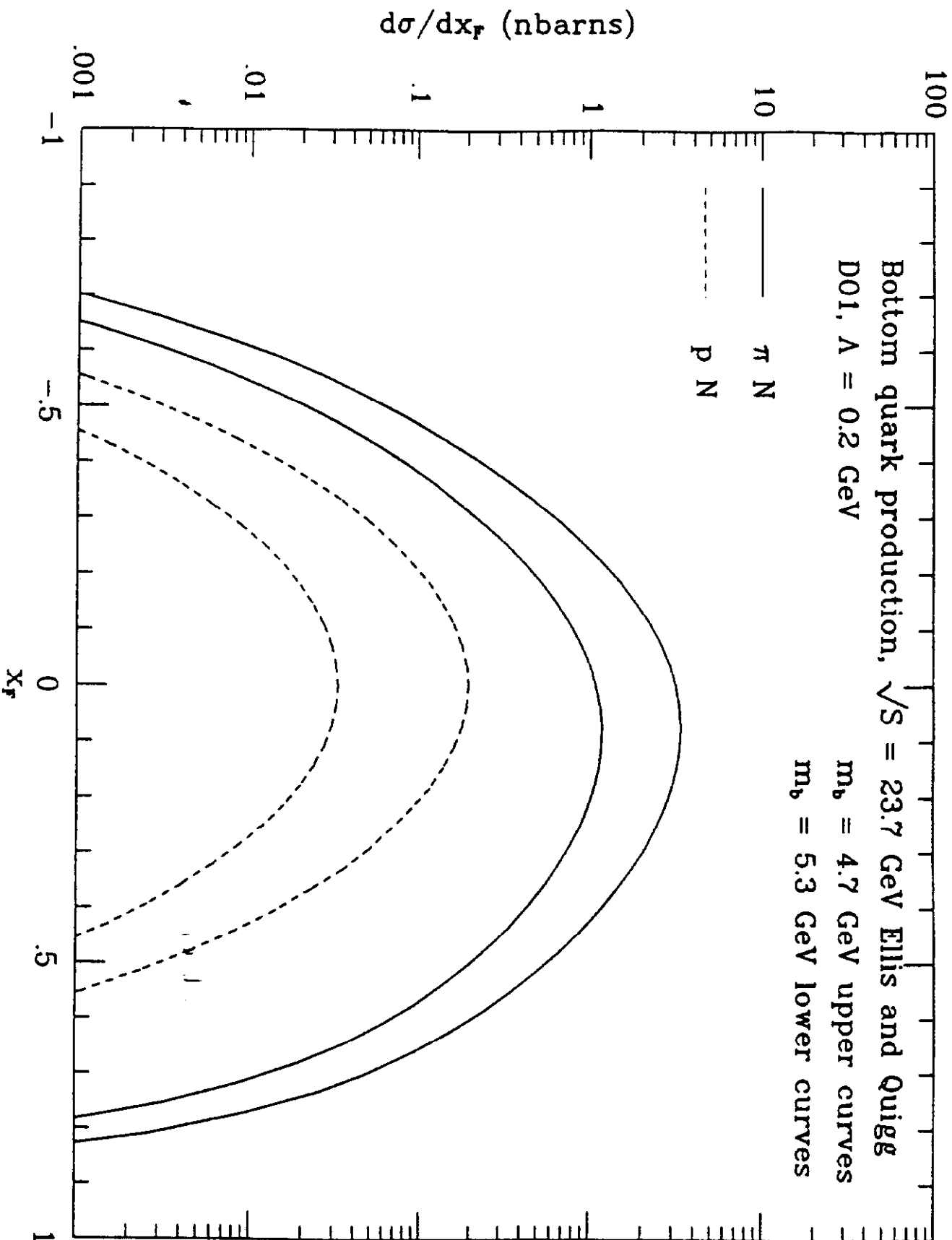


Figure 35: Differential cross section $d\sigma/dx_F$ for the production of bottom quarks in πN (solid lines) and pN (dashed lines) collisions at $\sqrt{s} = 23.7$ GeV ($p_{beam} = 300$ GeV/c).

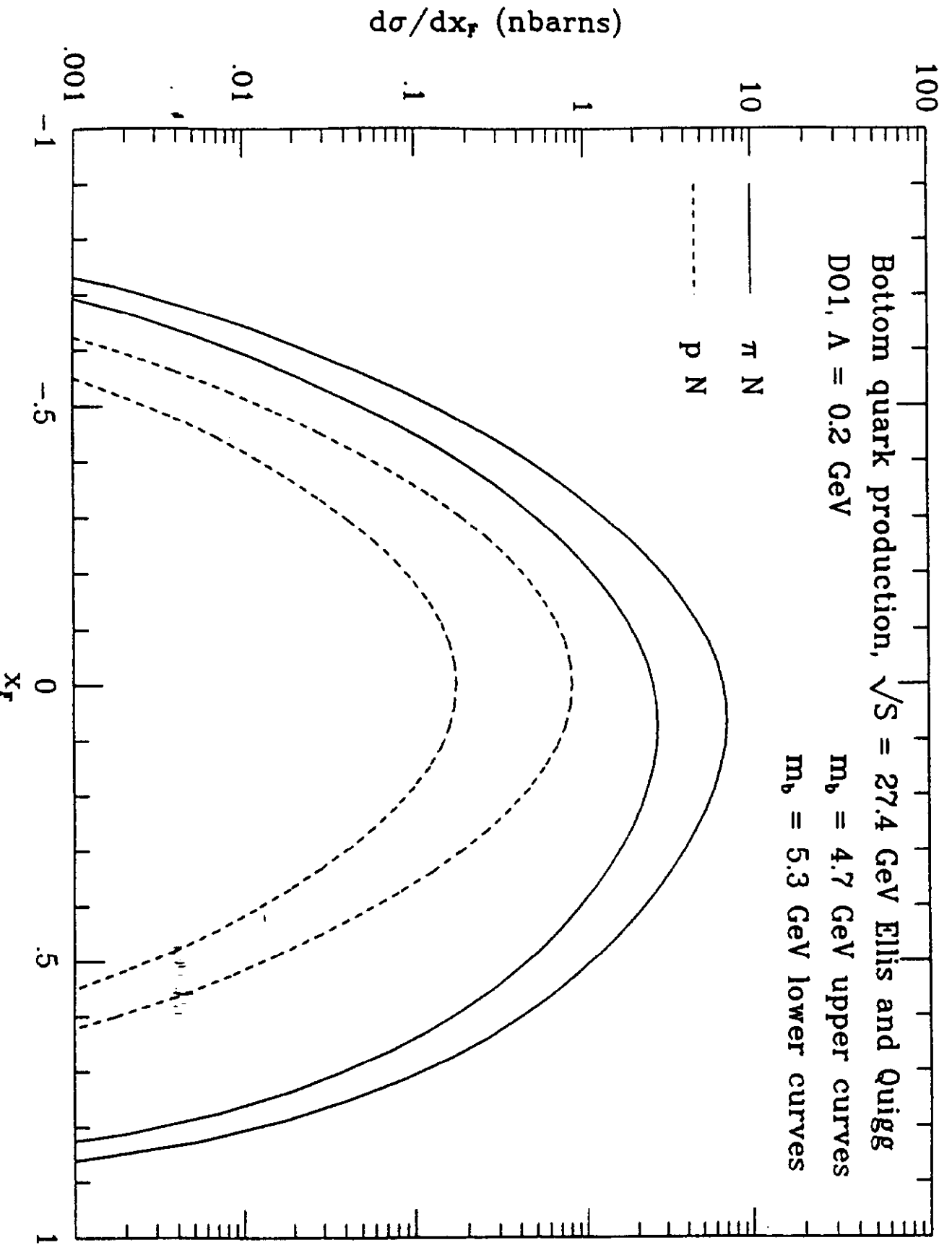


Figure 36: Differential cross section $d\sigma/dx_F$ for the production of bottom quarks in πN (solid lines) and pN (dashed lines) collisions at $\sqrt{s} = 27.4$ GeV ($p_{beam} = 400$ GeV/c).

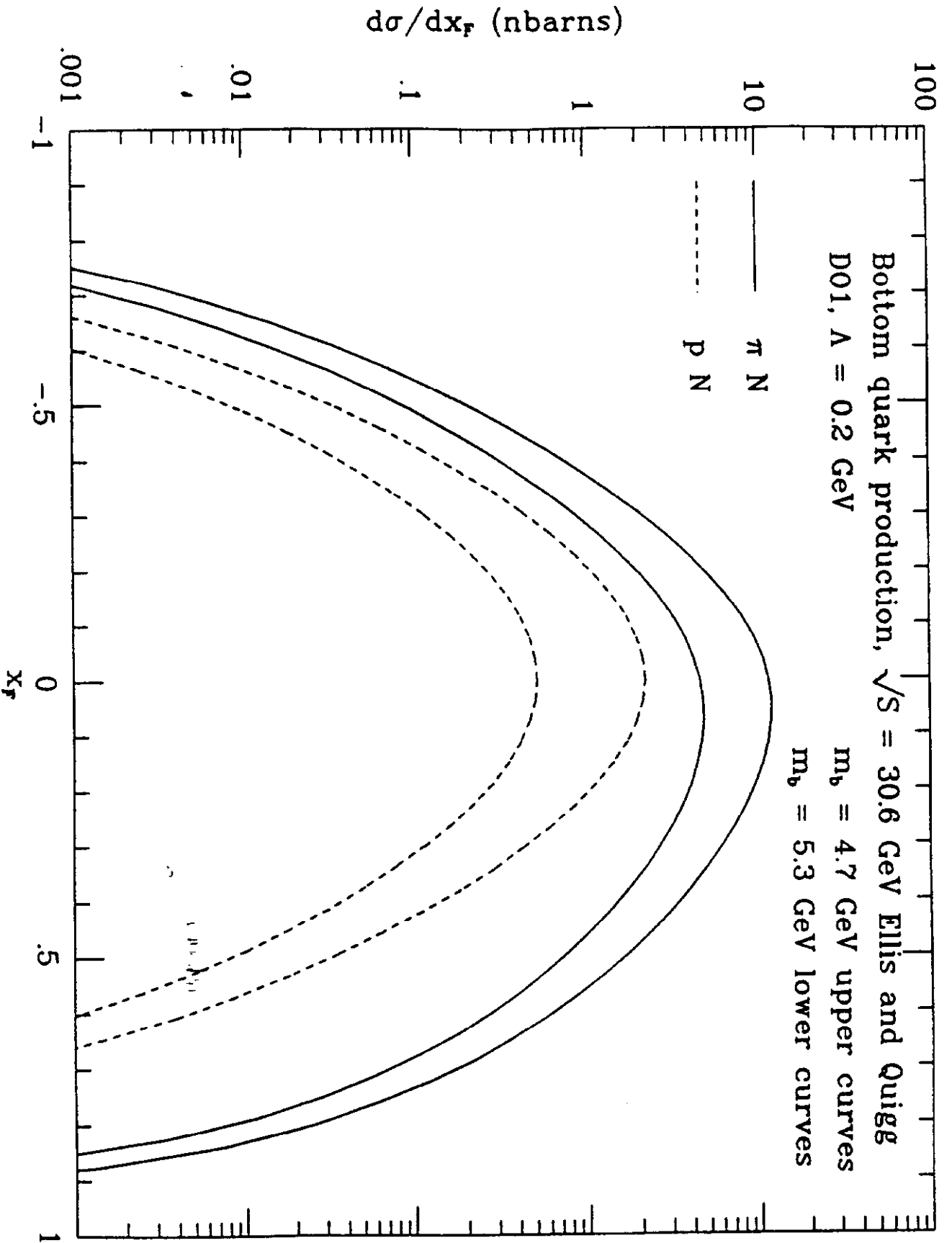


Figure 37: Differential cross section $d\sigma/dx_f$ for the production of bottom quarks in πN (solid lines) and pN (dashed lines) collisions at $\sqrt{s} = 30.6$ GeV ($p_{beam} = 500$ GeV/c).

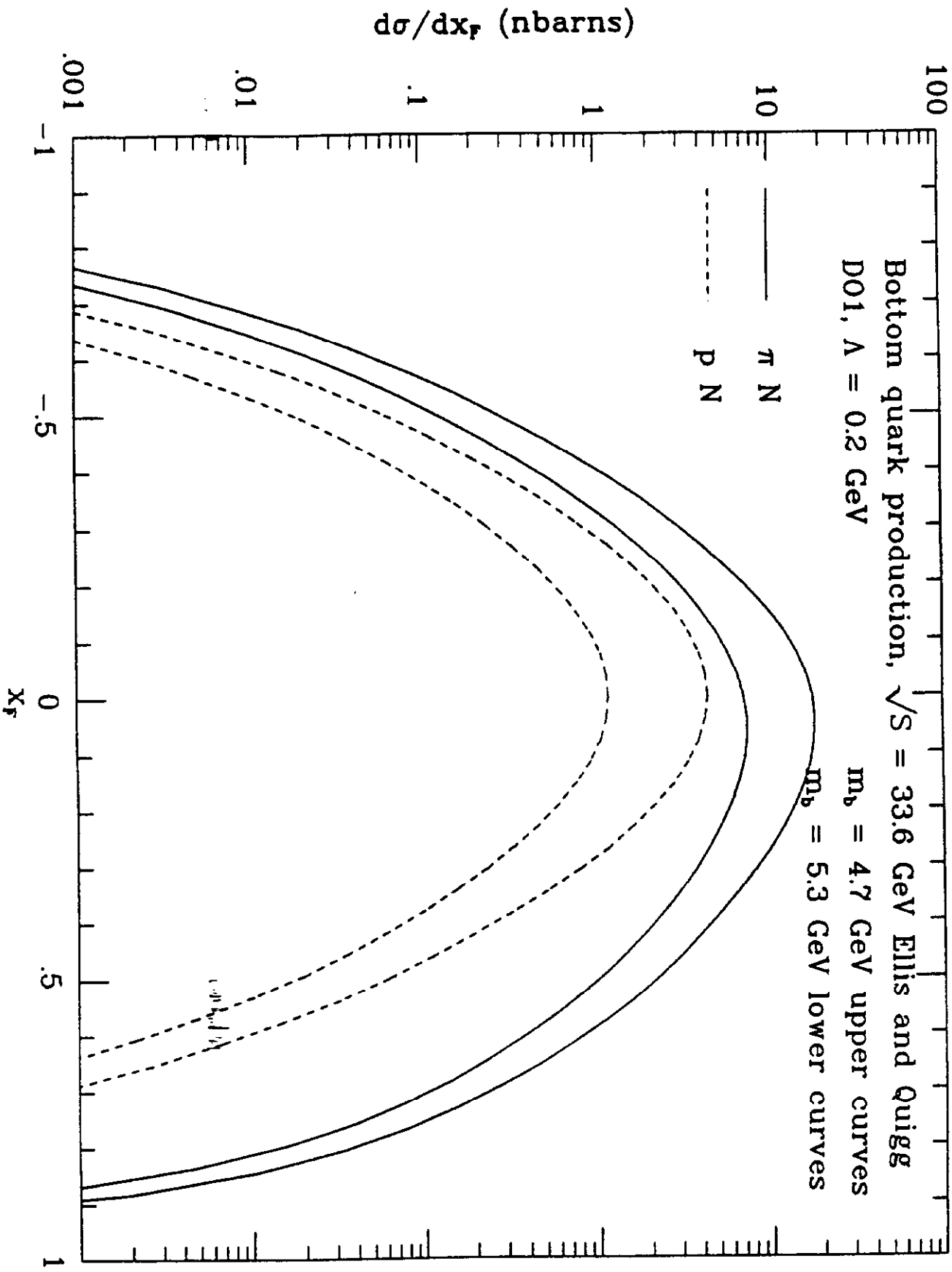


Figure 38: Differential cross section $d\sigma/dx_F$ for the production of bottom quarks in πN (solid lines) and pN (dashed lines) collisions at $\sqrt{s} = 33.6$ GeV ($p_{beam} = 600$ GeV/c).

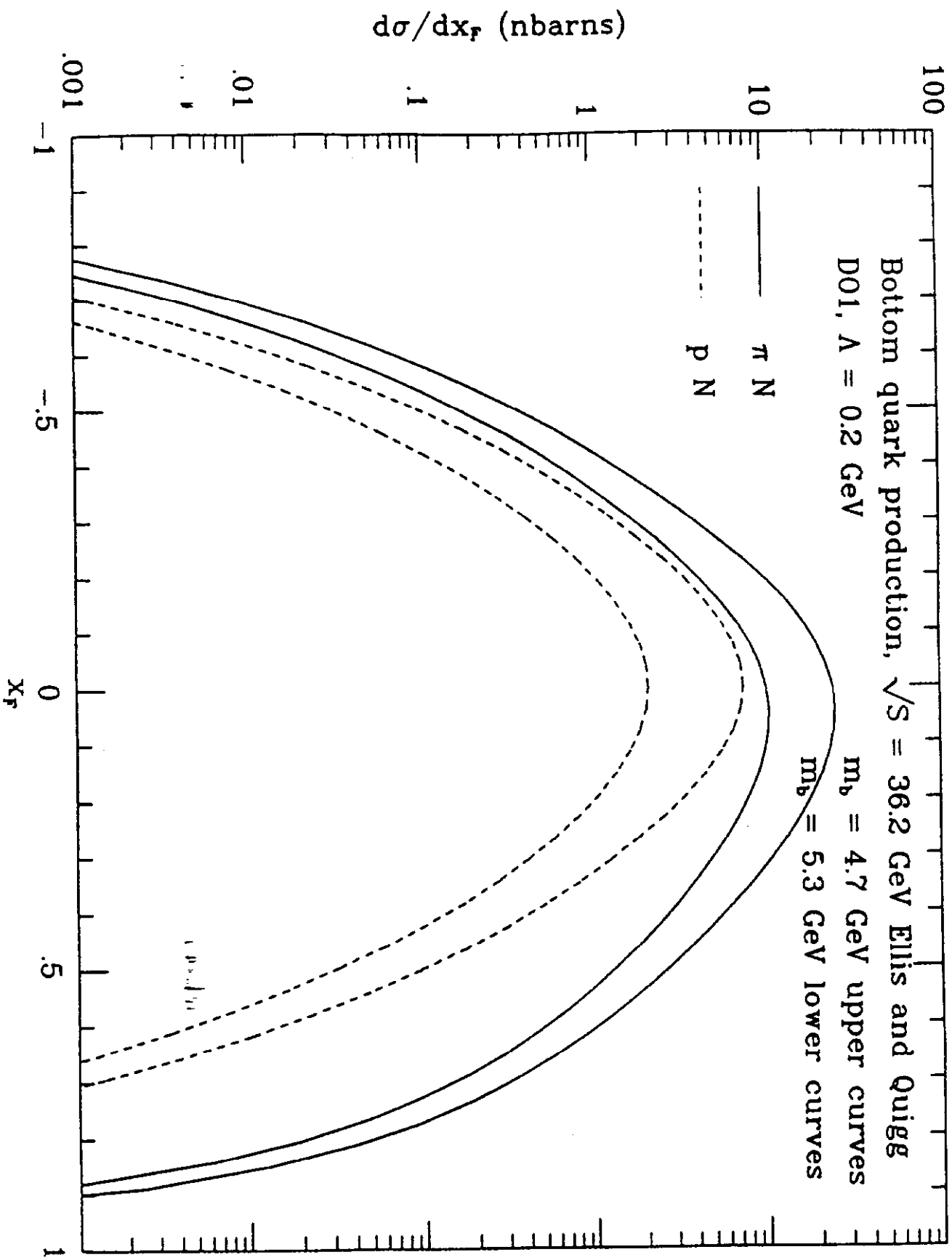


Figure 39: Differential cross section $d\sigma/dx_F$ for the production of bottom quarks in πN (solid lines) and pN (dashed lines) collisions at $\sqrt{s} = 36.3$ GeV ($p_{beam} = 700$ GeV/c).

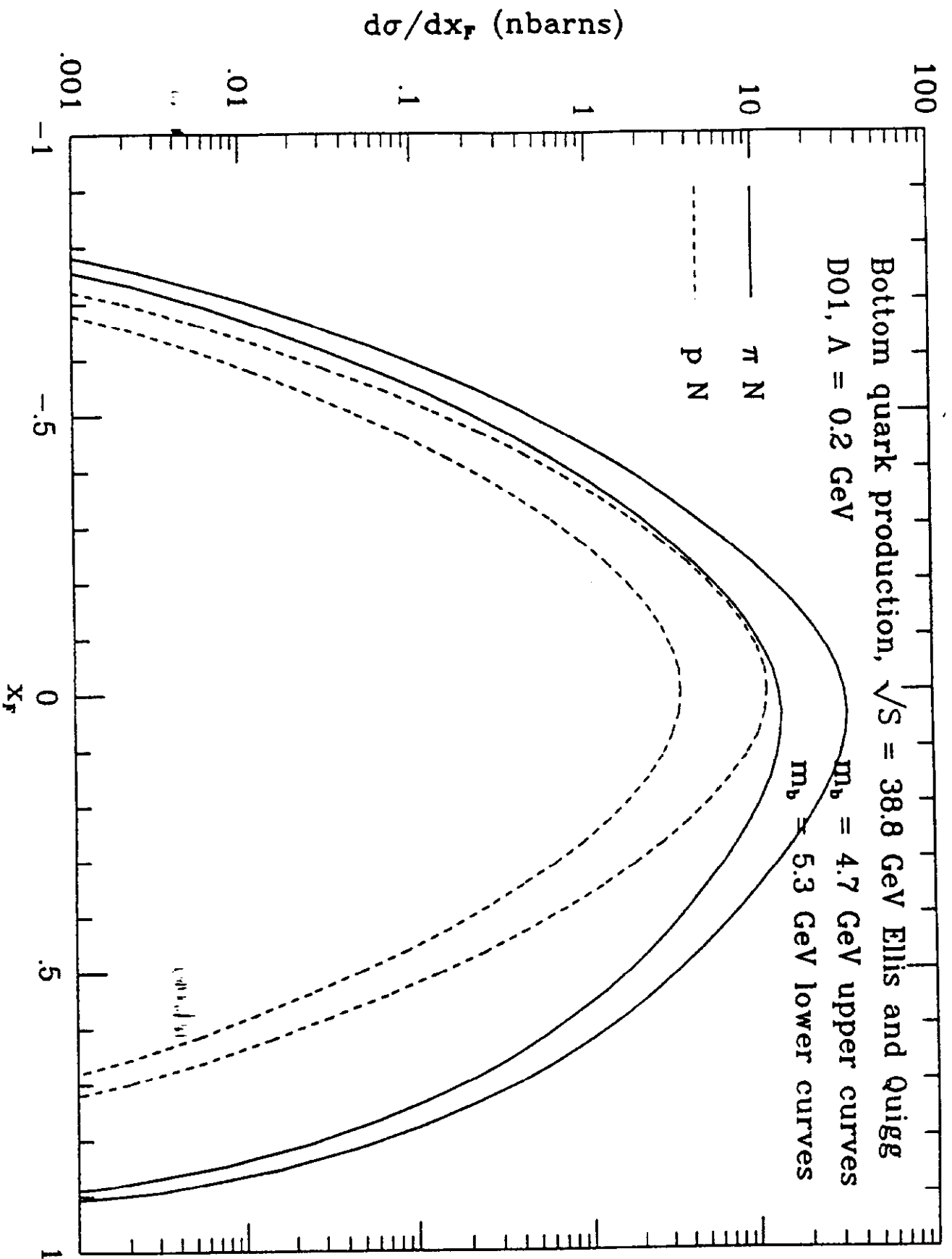


Figure 40: Differential cross section $d\sigma/dx_F$ for the production of bottom quarks in πN (solid lines) and pN (dashed lines) collisions at $\sqrt{s} = 38.8$ GeV ($p_{beam} = 800$ GeV/c).

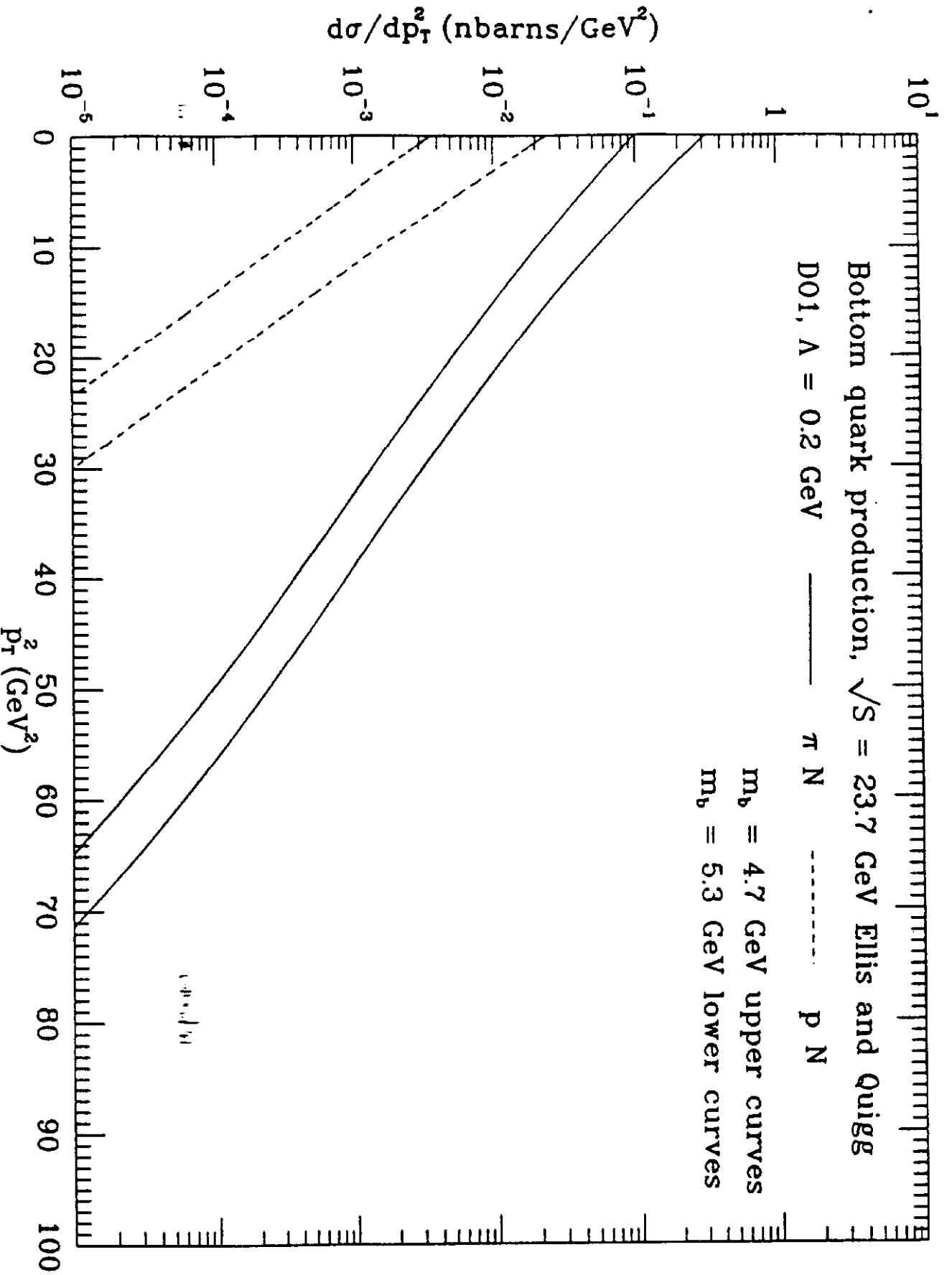


Figure 41: Differential cross section $d\sigma/dp_T^2$ for the production of bottom quarks in πN (solid lines) and pN (dashed lines) collisions at $\sqrt{s} = 23.7$ GeV ($p_{beam} = 300$ GeV/c).

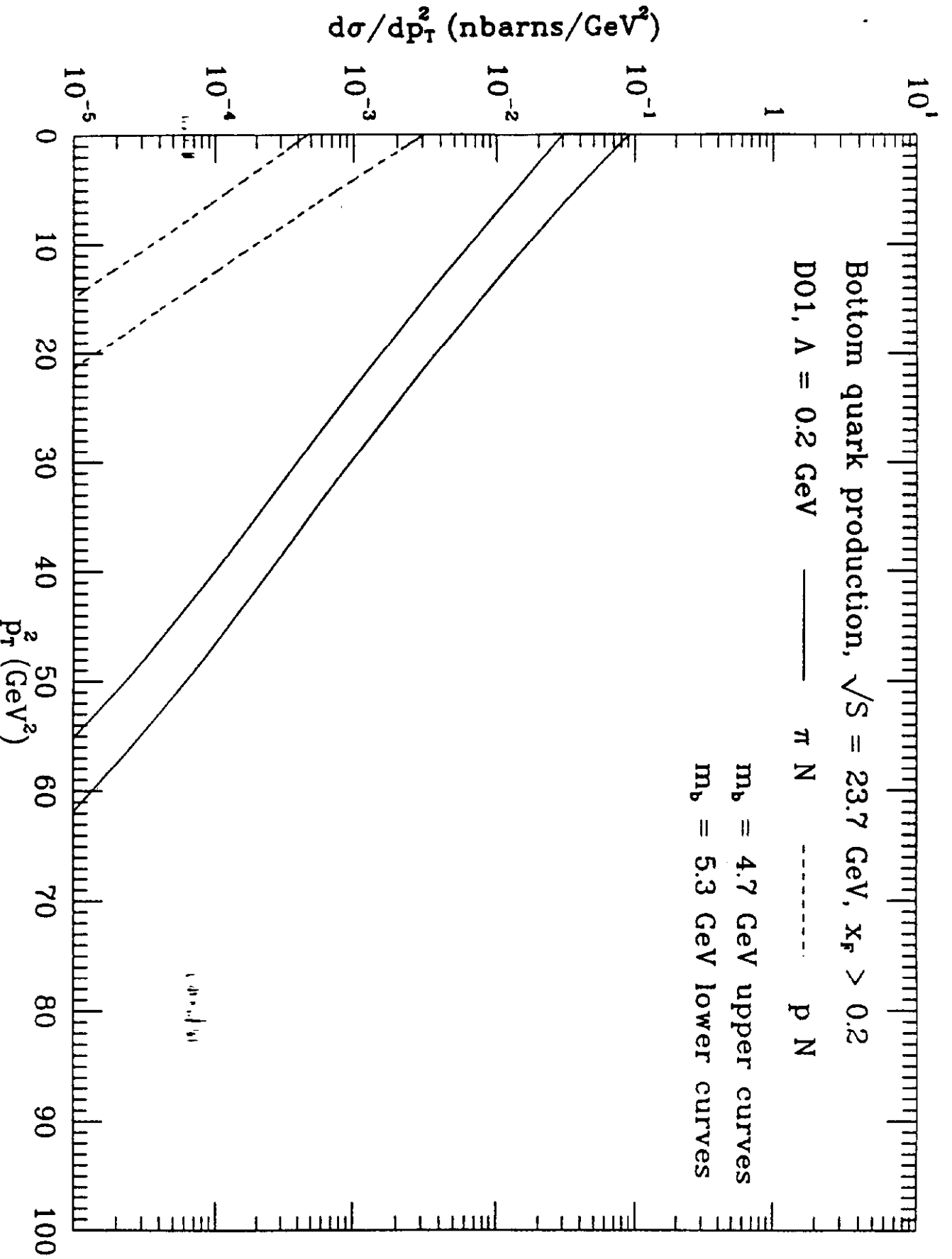


Figure 42: Differential cross section $d\sigma/dp_T^2$ for the forward production ($x_F > 0.2$) of bottom quarks in πN (solid lines) and pN (dashed lines) collisions at $\sqrt{s} = 23.7$ GeV ($p_{beam} = 300$ GeV/c).

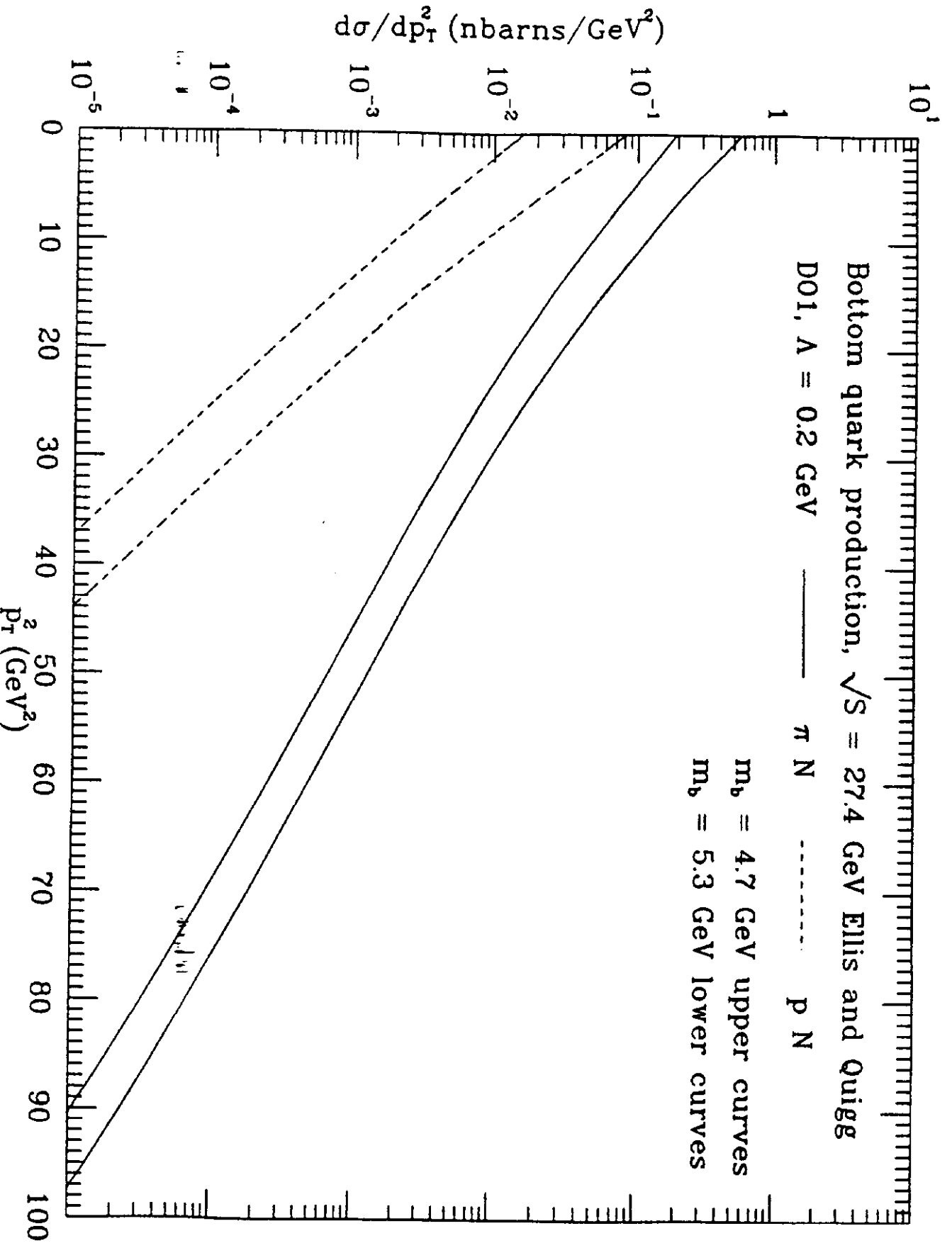


Figure 43: Differential cross section $d\sigma/dp_T^2$ for the production of bottom quarks in πN (solid lines) and pN (dashed lines) collisions at $\sqrt{s} = 27.4$ GeV ($p_{beam} = 400$ GeV/c).

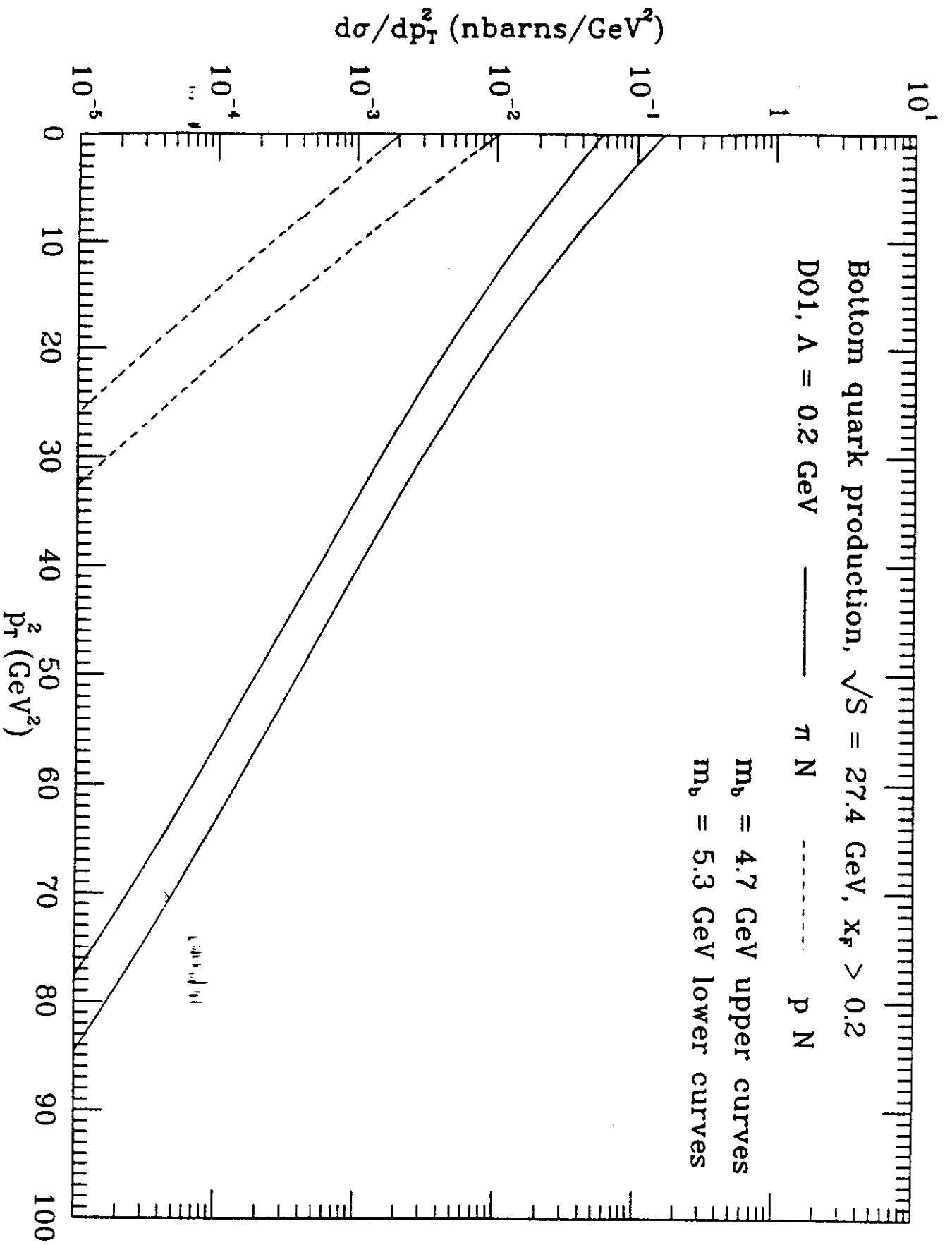


Figure 44: Differential cross section $d\sigma/dp_T^2$ for the forward production ($x_F > 0.2$) of bottom quarks in πN (solid lines) and pN (dashed lines) collisions at $\sqrt{s} = 27.4$ GeV ($p_{beam} = 400$ GeV/c).

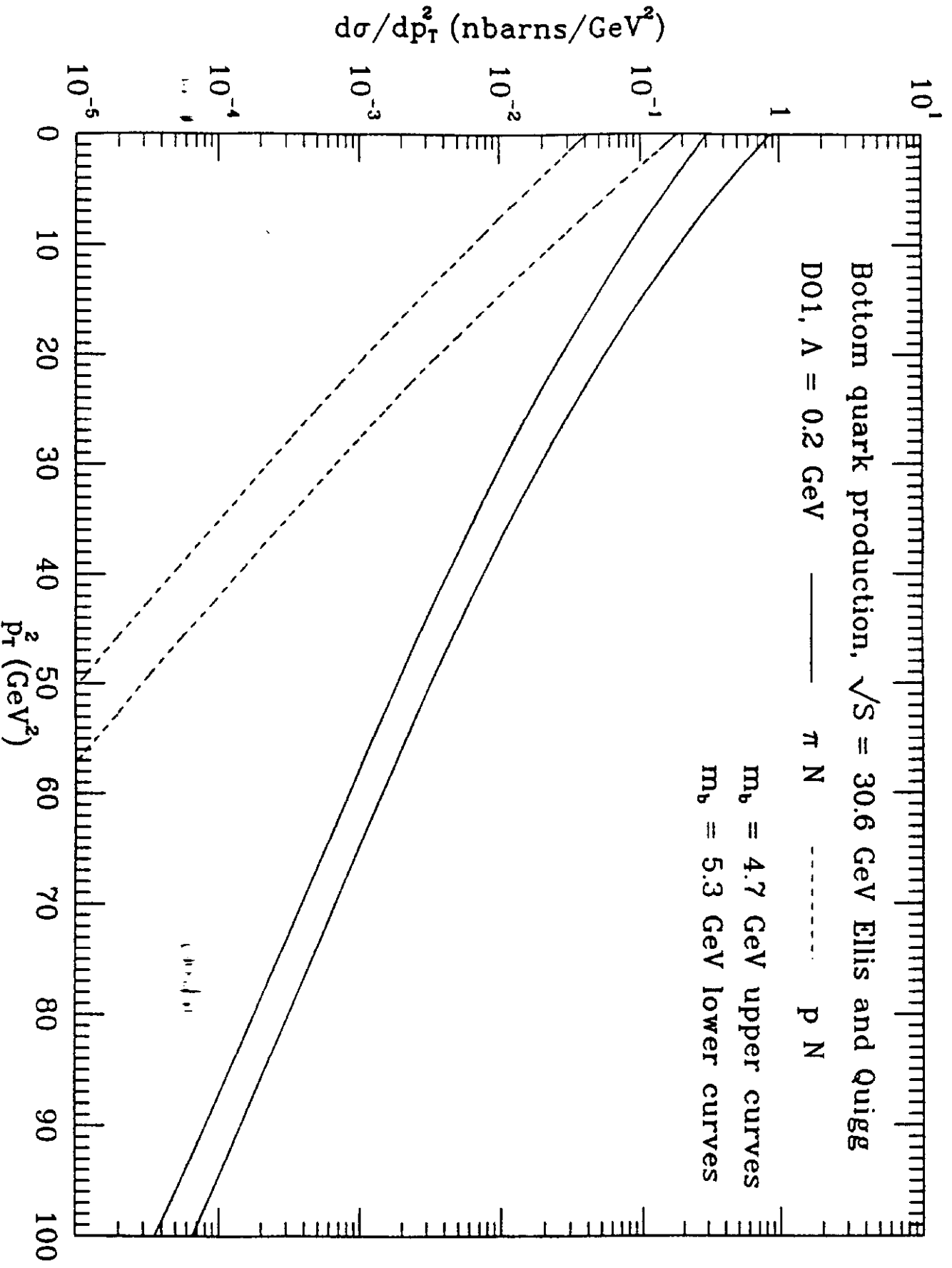


Figure 45: Differential cross section $d\sigma/dp_T^2$ for the production of bottom quarks in πN (solid lines) and pN (dashed lines) collisions at $\sqrt{s} = 30.6$ GeV ($p_{beam} = 500$ GeV/c).

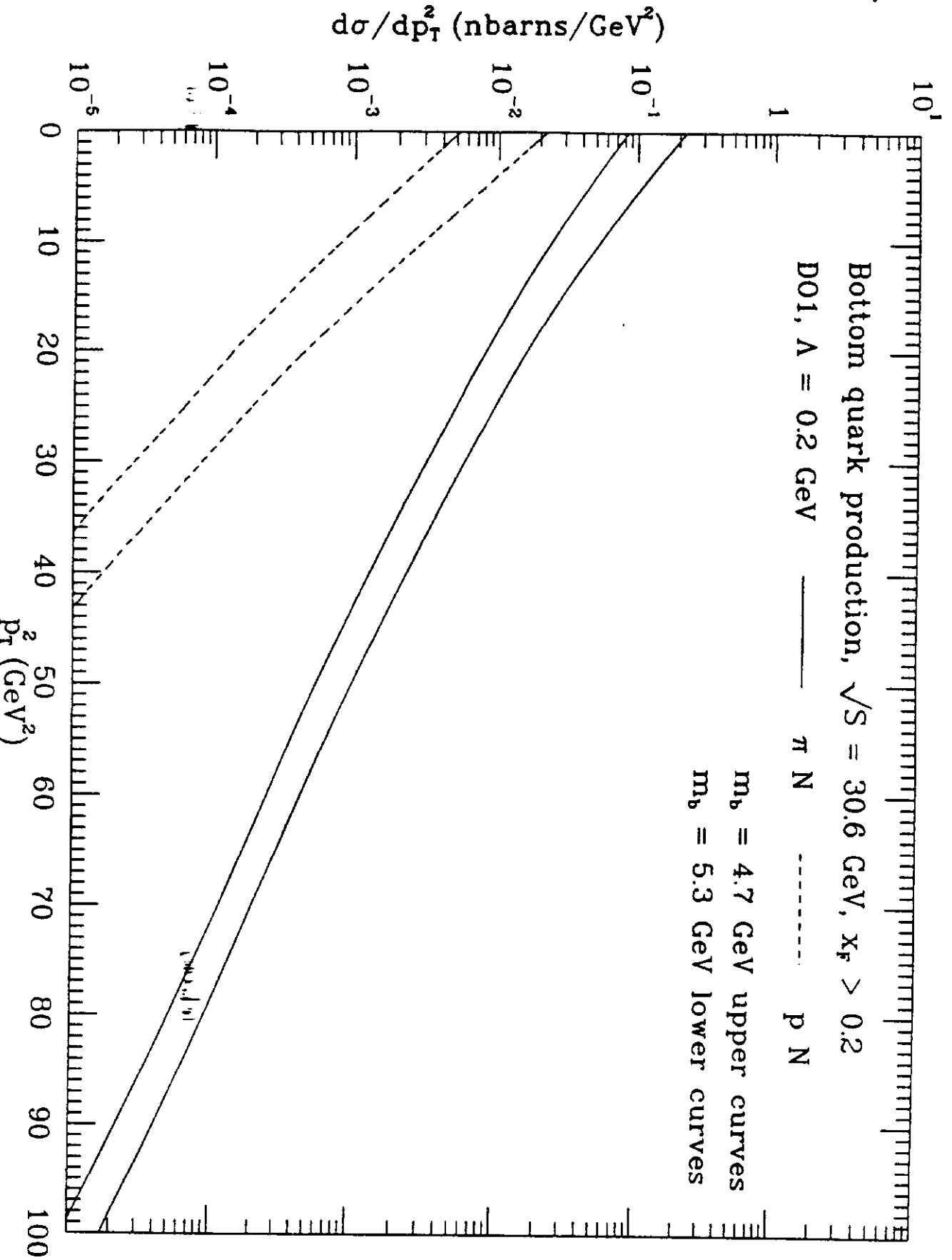


Figure 46: Differential cross section $d\sigma/dp_T^2$ for the forward production ($x_F > 0.2$) of bottom quarks in πN (solid lines) and pN (dashed lines) collisions at $\sqrt{s} = 30.6 \text{ GeV}$ ($p_{beam} = 500 \text{ GeV}/c$).

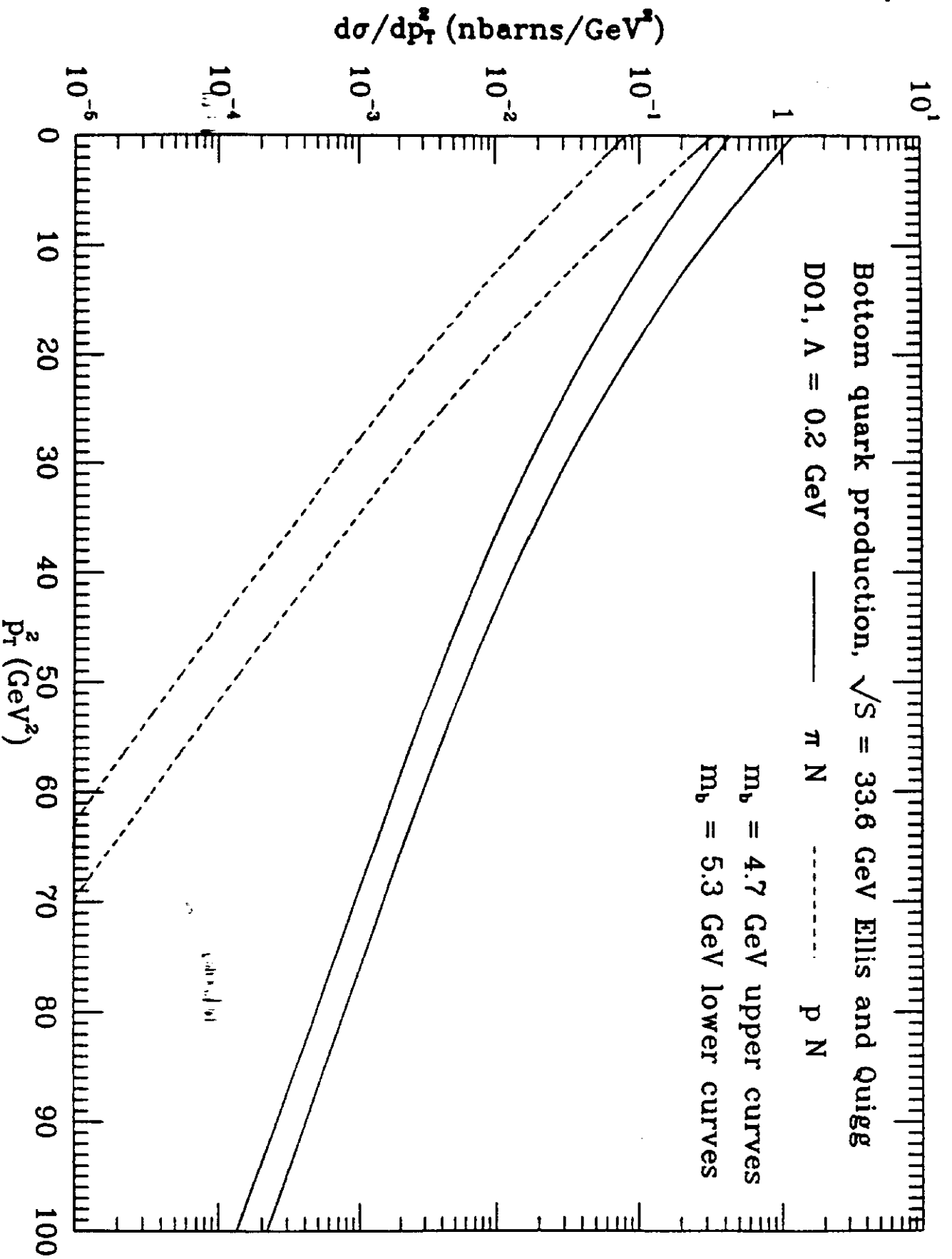


Figure 47: Differential cross section $d\sigma/dp_T^2$ for the production of bottom quarks in πN (solid lines) and pN (dashed lines) collisions at $\sqrt{s} = 33.6$ GeV ($p_{beam} = 600$ GeV/c).

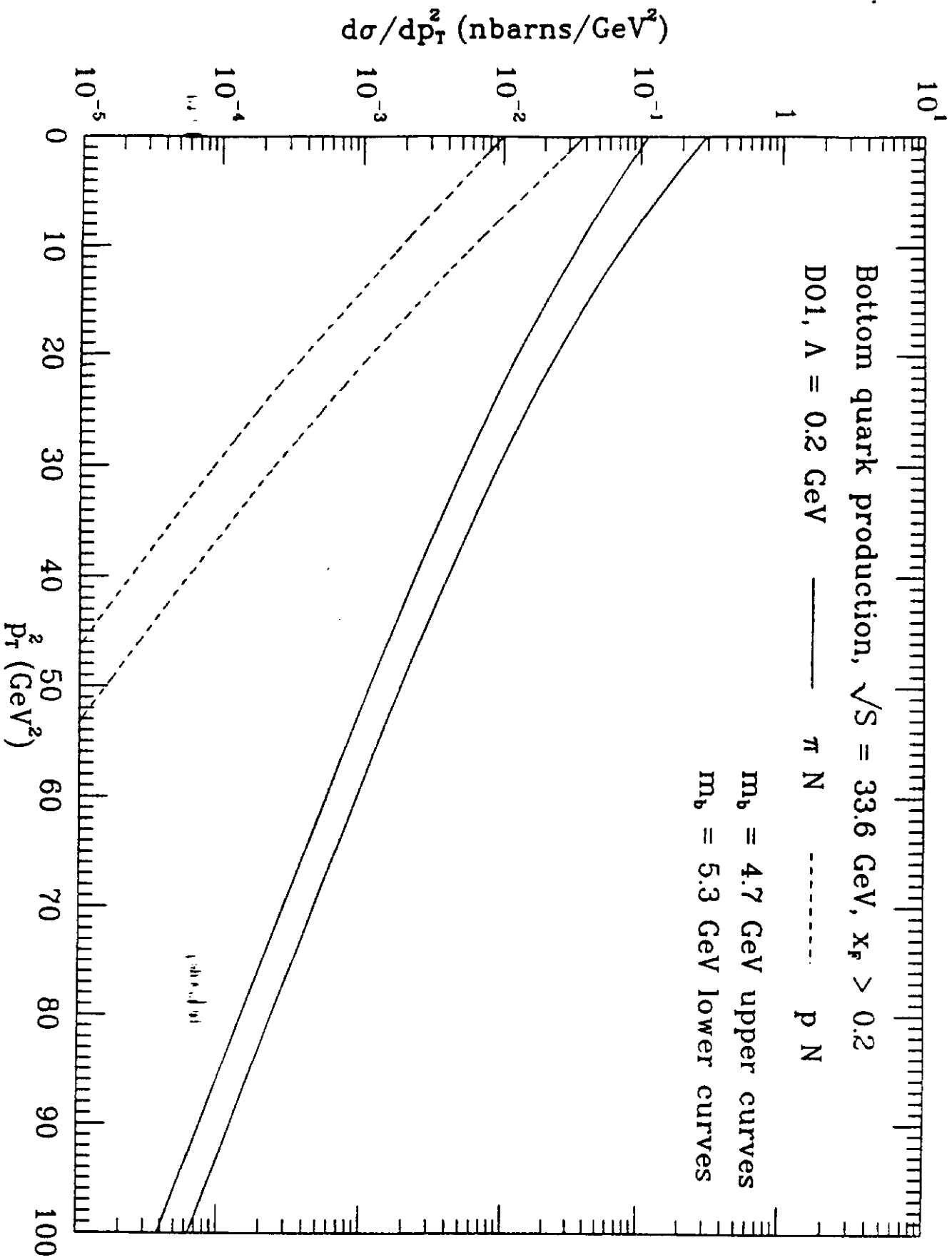


Figure 48: Differential cross section $d\sigma/dp_T^2$ for the forward production ($x_F > 0.2$) of bottom quarks in πN (solid lines) and $p N$ (dashed lines) collisions at $\sqrt{s} = 33.6$ GeV ($p_{beam} = 800$ GeV/c).

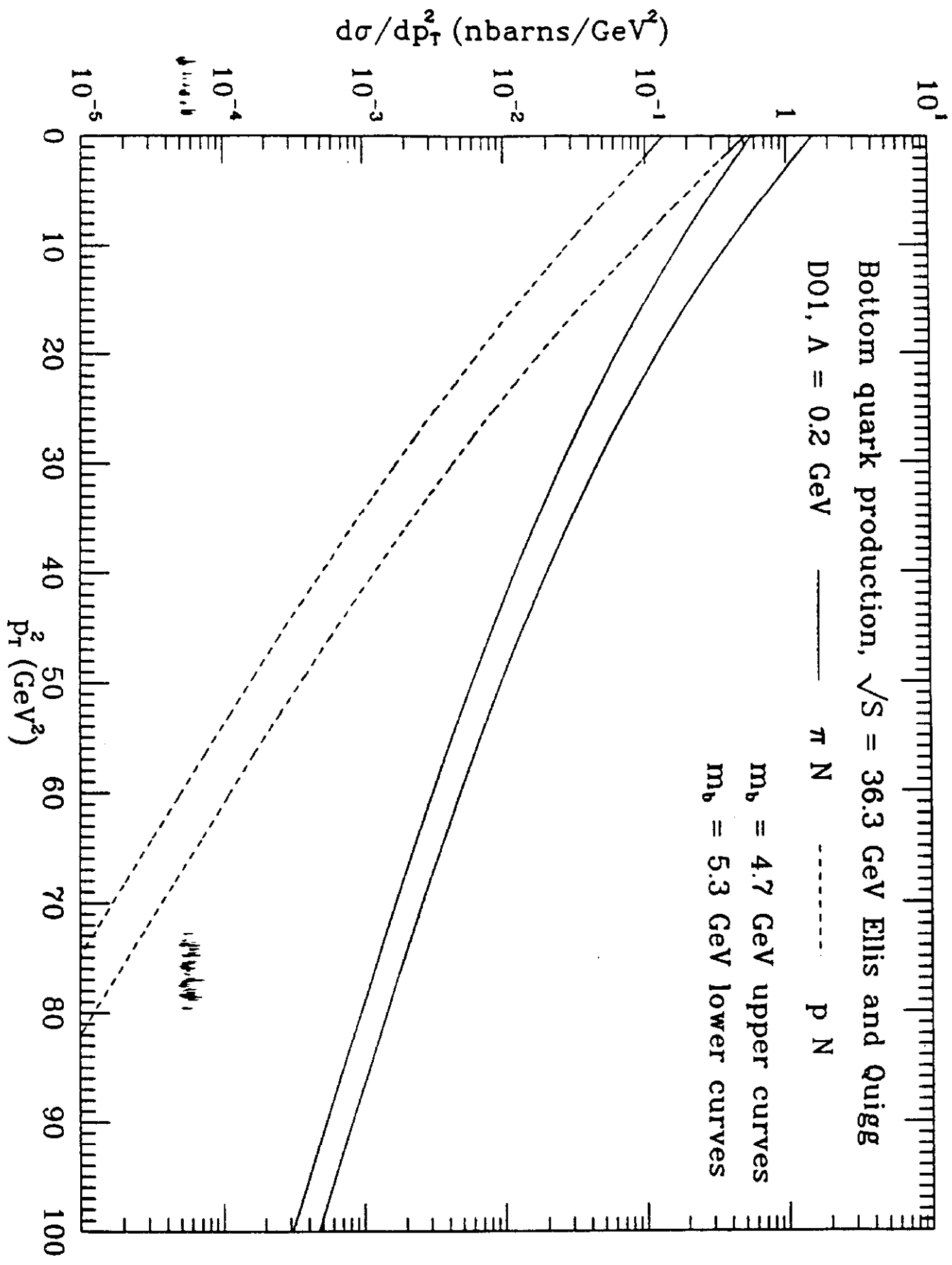


Figure 49: Differential cross section $d\sigma/dp_T^2$ for the production of bottom quarks in πN (solid lines) and pN (dashed lines) collisions at $\sqrt{s} = 36.3$ GeV ($p_{beam} = 700$ GeV/c).

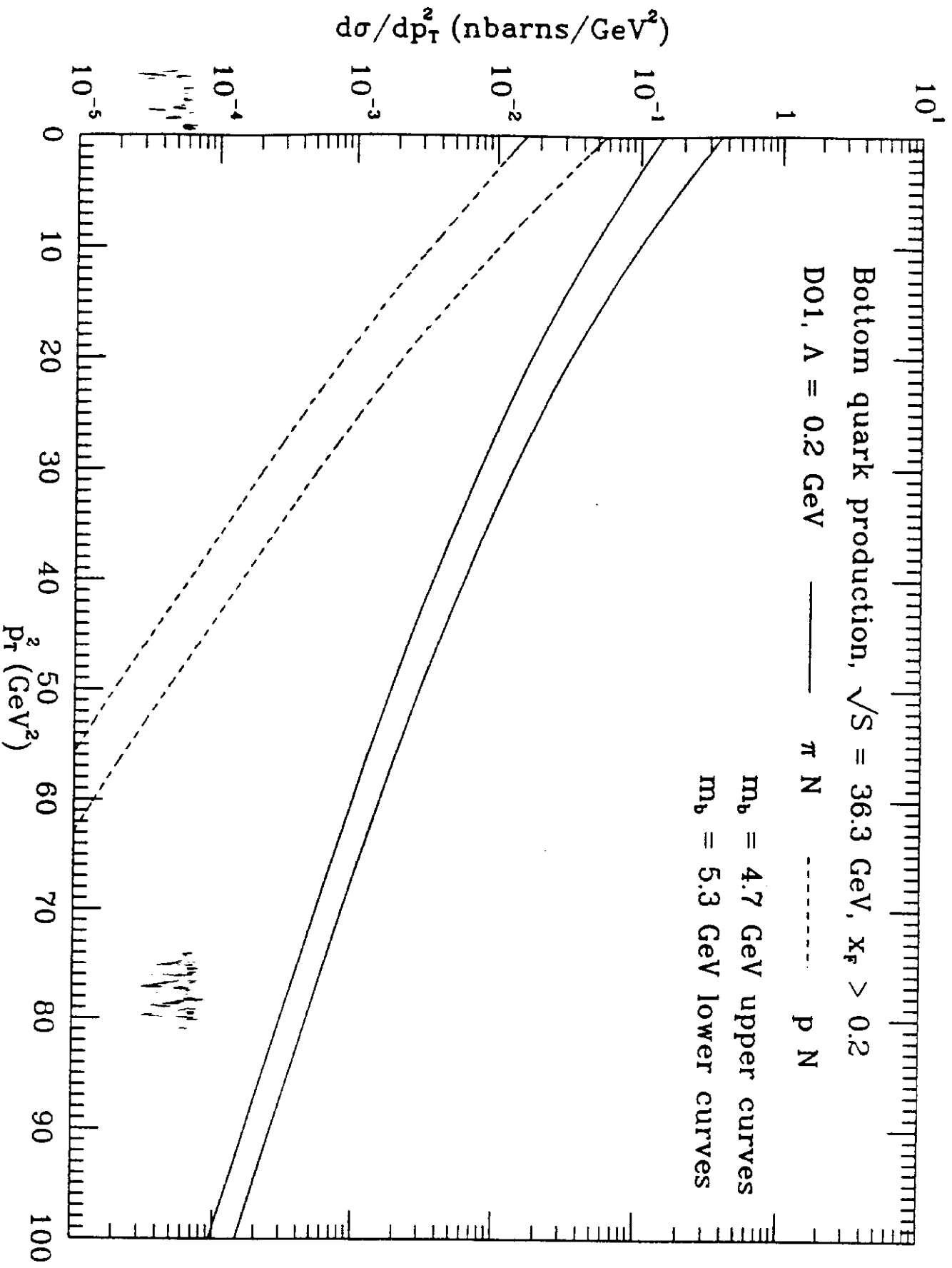


Figure 50: Differential cross section $d\sigma/dp_T^2$ for the forward production ($x_F > 0.2$) of bottom quarks in πN (solid lines) and pN (dashed lines) collisions at $\sqrt{s} = 36.3$ GeV ($p_{beam} = 700$ GeV/c).

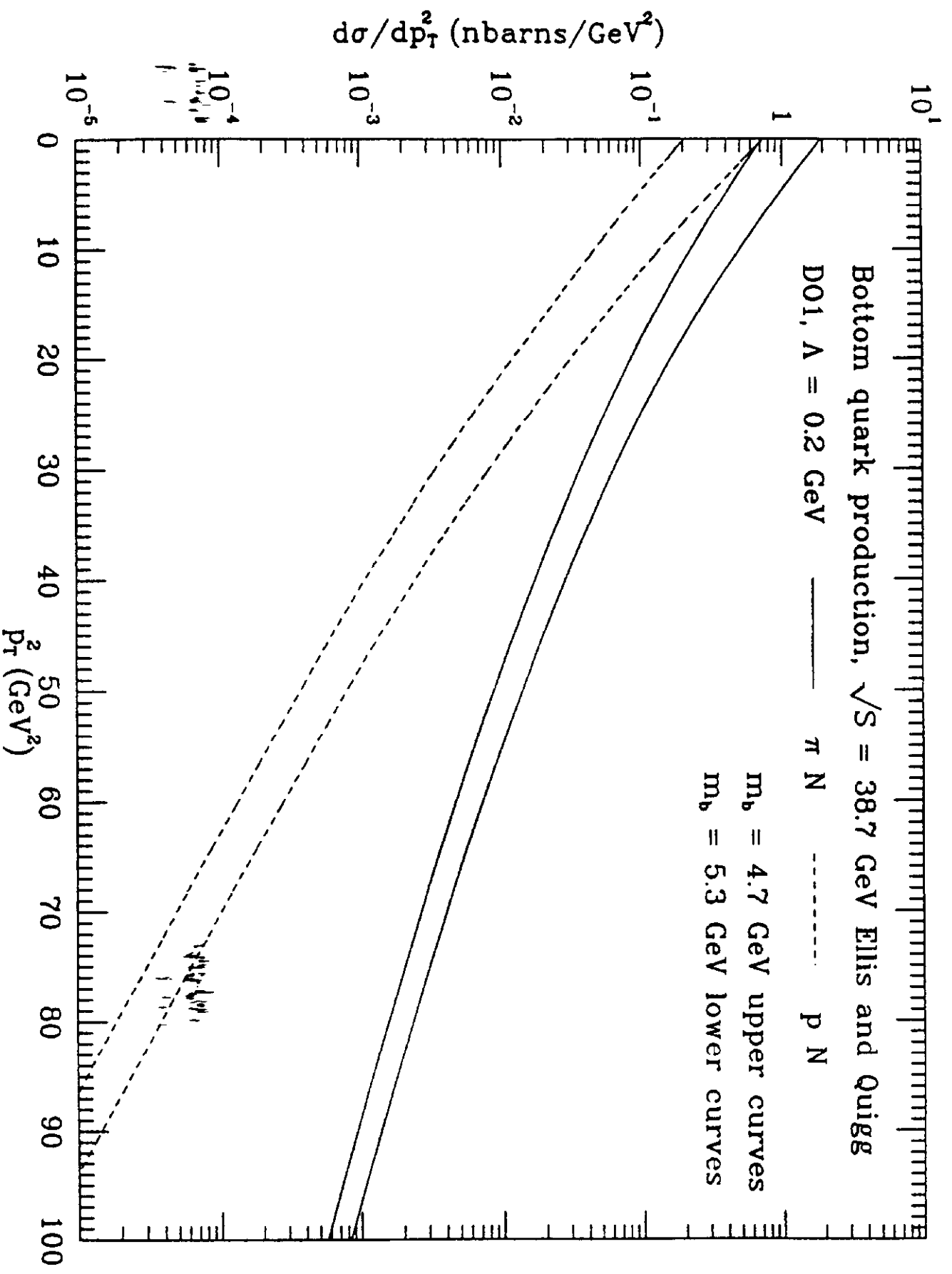


Figure 51: Differential cross section $d\sigma/dp_T^2$ for the production of bottom quarks in πN (solid lines) and pN (dashed lines) collisions at $\sqrt{s} = 38.8$ GeV ($p_{beam} = 800$ GeV/c).

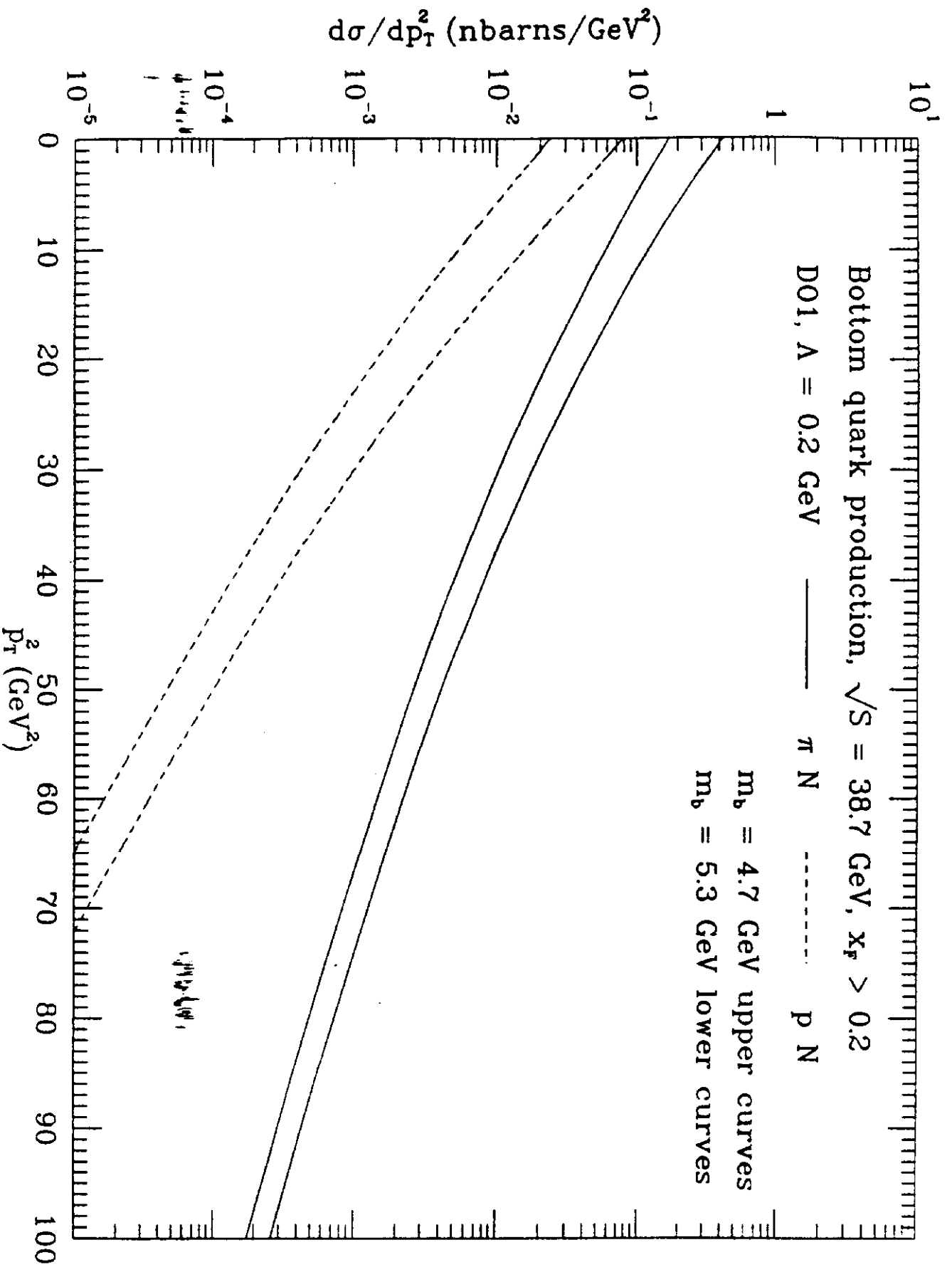


Figure 52: Differential cross section $d\sigma/dp_T^2$ for the forward production ($x_F > 0.2$) of bottom quarks in πN (solid lines) and pN (dashed lines) collisions at $\sqrt{s} = 38.8 \text{ GeV}$ ($p_{beam} = 800 \text{ GeV}/c$).

$pN \rightarrow bb + \text{anything}$

$$P_p = 600 \text{ GeV}/c$$

$$m_b = 5.3 \text{ GeV}/c^2$$

Ellis and Quigg

D01

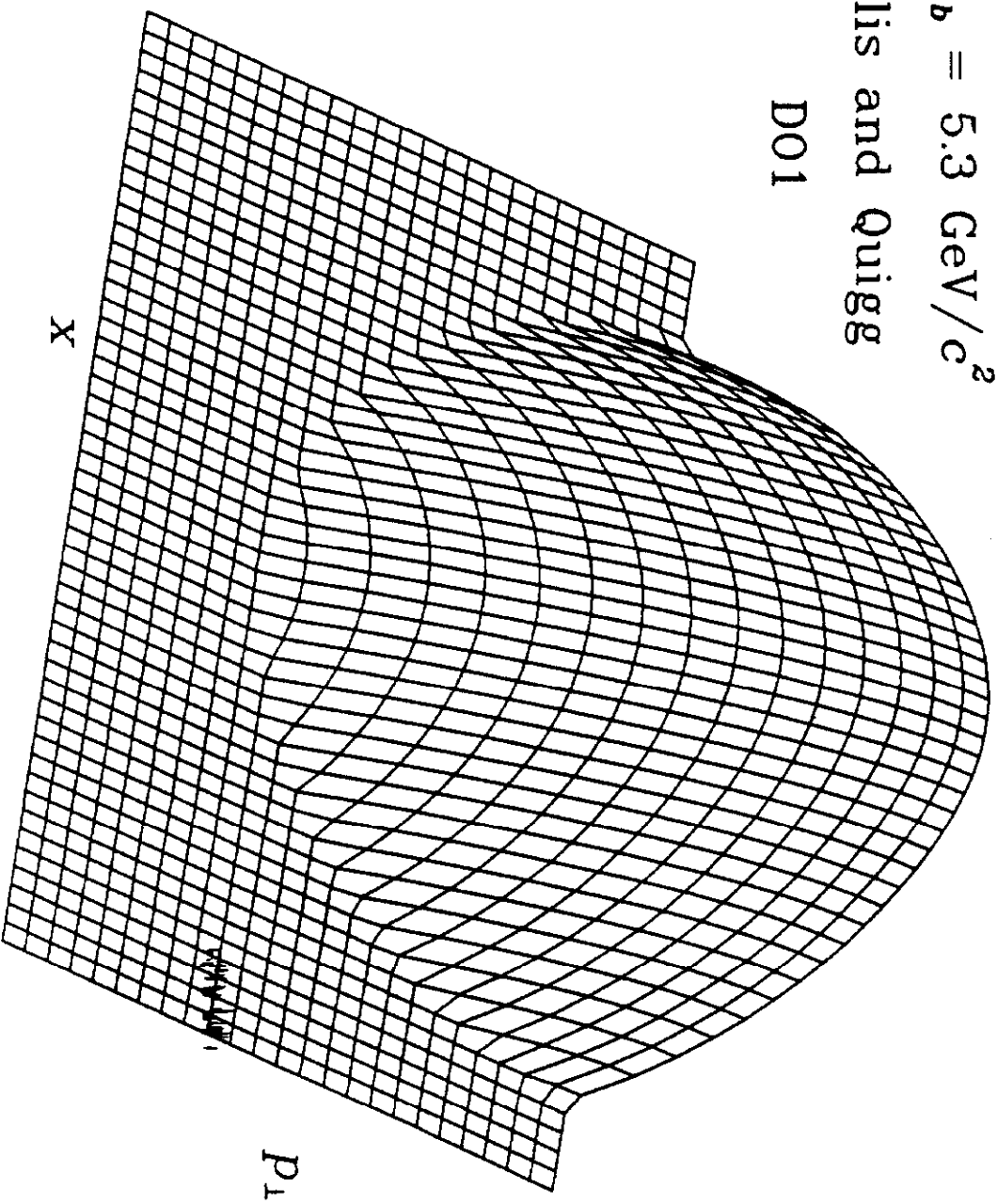


Figure 53: Three-dimensional representation of $\log E d\sigma/d^3p$ for the production of bottom quarks with $m_b = 5.3 \text{ GeV}/c^2$ in $600 \text{ GeV}/c$ pN collisions.

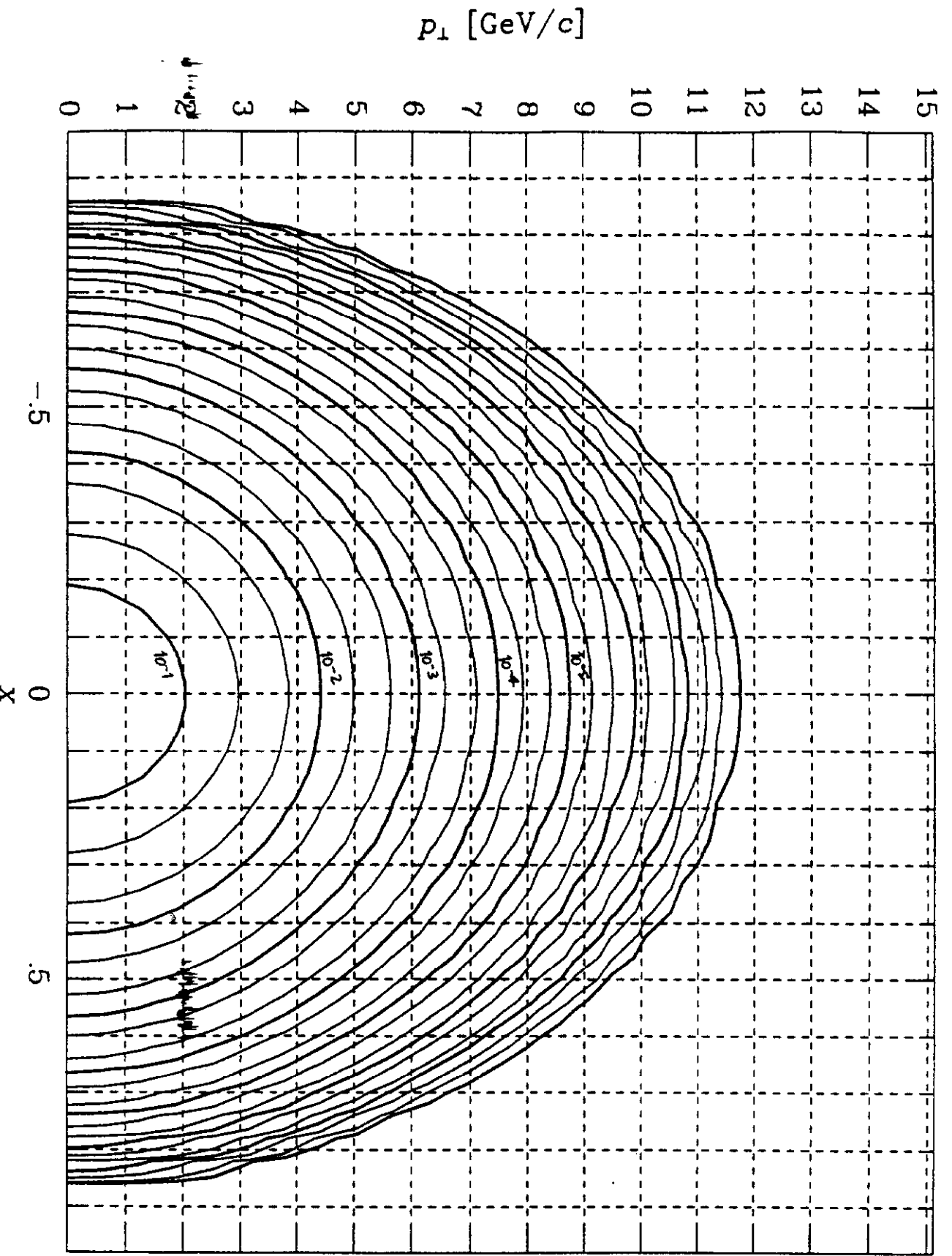


Figure 54: Contour plot of $\log E d\sigma/d^3p$ for the production of bottom quarks with $m_b = 5.3$ GeV/c² in 600 GeV/c pN collisions.

$\pi N \rightarrow bb + \text{anything}$

$$P_\pi = 600 \text{ GeV}/c$$

$$m_b = 5.3 \text{ GeV}/c^2$$

Ellis and Quigg

D01

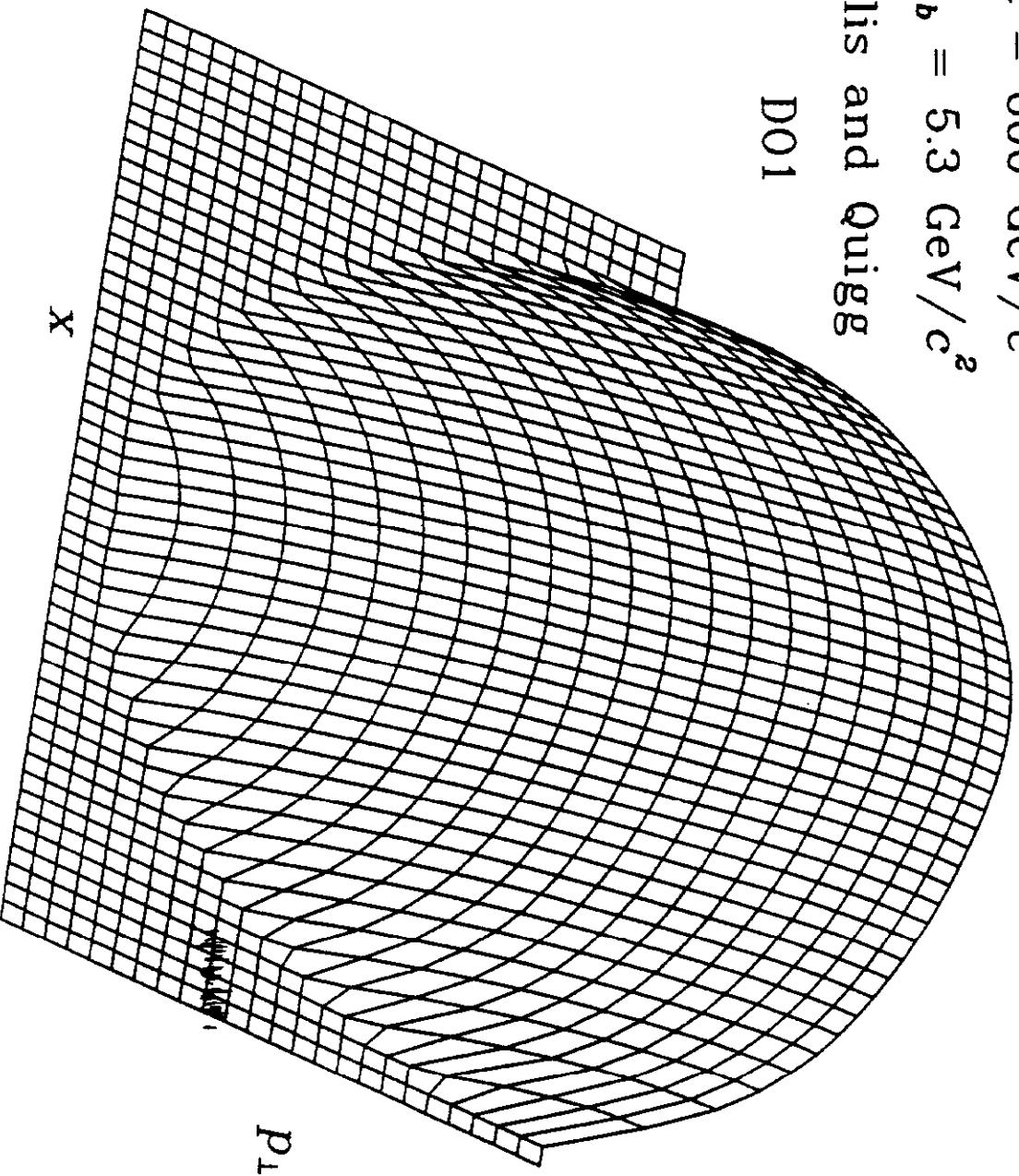


Figure 55: Three-dimensional representation of $\log E d\sigma/d^3p$ for the production of bottom quarks with $m_b = 5.3 \text{ GeV}/c^2$ in $600 \text{ GeV}/c$ πN collisions.

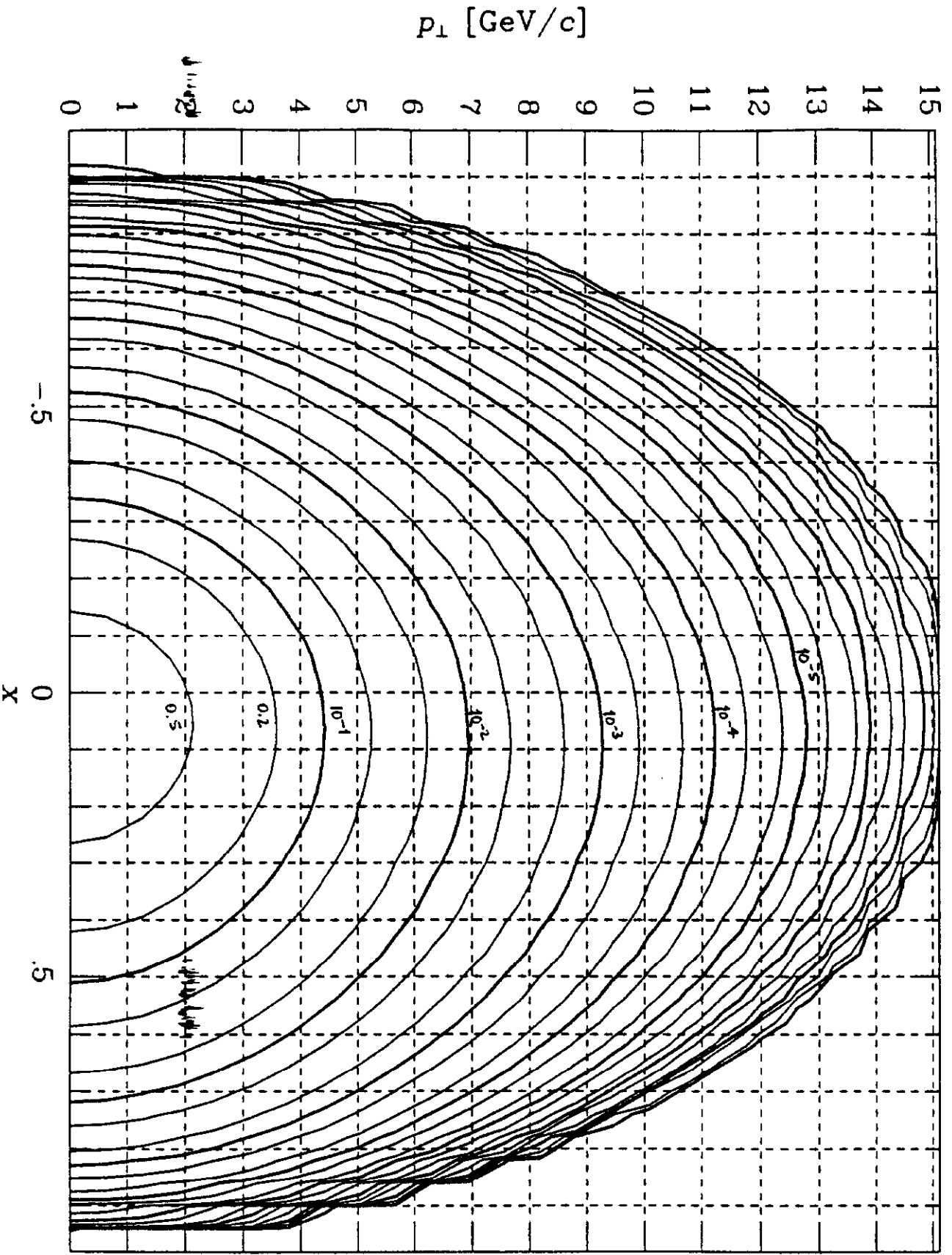


Figure 56: Contour plot of $\log E d\sigma/d^3p$ for the production of bottom quarks with $m_b = 5.3 \text{ GeV}/c^2$ in $600 \text{ GeV}/c \pi N$ collisions.